

Electronic structures and optical properties of Sn(II)  
ternary oxides

Shota Katayama

2015



Electronic structures and optical properties of Sn(II)  
ternary oxides

(二価スズ複合酸化物の電子構造と電気・光学特性)

Shota Katayama

片山 翔太

2015

## Contents

<b>Chapter 1</b>	<b>General introduction</b>	<b>1</b>
<b>Chapter 2</b>	<b>Electronic structures of Sn(II) ternary oxides</b>	<b>7</b>
1.	Introduction	7
2.	Computational procedure	9
3.	Results and discussion	12
4.	Conclusion	32
<b>Chapter 3</b>	<b>Epitaxial growth and characterization of Sn(II) ternary oxides</b>	<b>35</b>
1.	Introduction	35
2.	Experiments	40
3.	Epitaxial growth of Sn(II) ternary oxides with Nb, Ta, and W	42
A.	Sn- <i>M</i> -O ( <i>M</i> =Nb, Ta) with a pyrochlore structure	42
B.	SnNb <sub>2</sub> O <sub>6</sub>	51
C.	SnWO <sub>4</sub>	56
4.	Optical and electrical properties of Sn(II) ternary oxides	61
5.	Conclusion	70
	Appendix: Fabrication and characterization of an Sn-Ti-O thin film	73

<b>Chapter 4</b>	<b>Analysis on native point defects in SnNb<sub>2</sub>O<sub>6</sub></b>	<b>79</b>
1.	Introduction	79
2.	Computational procedure	82
3.	Results and discussion	85
4.	Conclusion	97
<b>Chapter 5</b>	<b>Summary and Conclusion</b>	<b>99</b>
<b>Acknowledgements</b>		<b>101</b>

# Chapter 1

## General introduction

Oxide semiconductors have been widely studied for various applications such as thin film transistors[1], solar cells[2], and ultraviolet light-emitting diodes[3]. To obtain objective functions of semiconductors, it is inevitable to understand and design the electronic structures especially around their band gaps. Through previous researches, general tendency of electronic structures has been established for typical oxides. Most of the typical oxides have valence band maximums (VBM) mainly composed of O-2*p* orbitals which are spatially localized and exhibit large electron affinity, which raises a low hole mobility and difficulty of hole doping. Due to this character, *p*-type oxide semiconductors with superior transporting properties are limited in contrast to the variety of *n*-type oxides including In<sub>2</sub>O<sub>3</sub>[4], ZnO[5,6], and SnO<sub>2</sub>[7]. In this point, oxides which have the VBM with contribution of cation orbitals are attracted attentions. The typical example with such an electronic structure is Cu(I) oxide, Cu<sub>2</sub>O. Cu<sub>2</sub>O is well known as a representative *p*-type oxide semiconductor, where hybridization of O-2*p* and Cu-3*d* orbitals occurs around the VBM[8]. The hybridization provides widely dispersed shallow VBM states. Such an electronic structure is observed in Cu(I) complex oxides. Actually, some multifunctional materials have been developed from Cu(I) complex oxides[9-11], such as CuInO<sub>2</sub> with bipolar conductivity and SrCu<sub>2</sub>O<sub>2</sub> with both of transparency and *p*-type conductivity.

Another example with a unique VBM structure is Sn(II) oxide. SnO, the prototypical Sn(II) oxide, is known as a *p*-type semiconductor[12,13] due to the VBM

constructed from hybridization of O-2*p* and Sn-5*sp*[14,15]. In addition to this electronic structure, SnO exhibits a characteristic layered crystal structure due to the presence of lone-pair electrons. In contrast to Cu(I) systems, the variety and number of reports on Sn(II) complex oxides are poor because Sn tends to exhibit tetravalent in oxides. Reported partner ions for Sn(II) ternary oxides are limited to high valence ions over tetravalent or alkali metal ions; W<sup>6+</sup>[16,17], S<sup>6+</sup>[18], Nb<sup>5+</sup>[19,20], Ta<sup>5+</sup>[21,22], Ti<sup>4+</sup>[23], Na<sup>+</sup>[24], K<sup>+</sup>[25], Rb<sup>+</sup>[26], Cs<sup>+</sup>[26]. Among them, compounds of transition metals with *d*<sup>0</sup> electronic configuration have received attentions for photocatalytic activity or piezoelectricity, e. g., SnWO<sub>4</sub>[27], SnNb<sub>2</sub>O<sub>6</sub>[28], Sn<sub>2</sub>Ta<sub>2</sub>O<sub>7</sub>[28], SnTiO<sub>3</sub>[29].

In previous works, the main concern has been photocatalytic activity for water splitting under visible light irradiation. *d*<sup>0</sup> transition metal ions oxides such as TiO<sub>2</sub>[30], Nb<sub>2</sub>O<sub>5</sub>[31], and Ta<sub>2</sub>O<sub>5</sub>[32] are well known photocatalytic materials but they have low optical absorption coefficients for visible light because of their wide band gaps. In contrast, ternary compounds with Sn(II) are expected to clear this problem due to the shallow VBM states formed by the hybridization of O-2*p* and Sn-5*sp*. Indeed, Y. Hosogi *et al.* have reported that SnNb<sub>2</sub>O<sub>6</sub> has a band gap of 2.3 eV[28] and shows photocatalytic activity for H<sub>2</sub> evolution from an aqueous methanol solution under visible light irradiation. They have also shown its valence band character similar to that of SnO using first-principles calculations[33]. Such valence band structures were predicted for some of the other ternary oxides written above as well[34-36].

While some have reported photocatalytic activities and band gaps of Sn(II) complex oxides, most of their fundamental properties have not been investigated including electrical conductivity and absorption coefficients, despite their unique electronic structures. Additionally, the previous works on first-principles calculations

are sporadic and some of them were carried out with course conditions to describe band structures. In this thesis, I aim to investigate the optical and electrical properties of Sn(II) oxides and reveal their relation with the electronic structures. For this purpose, systematic first-principles calculations on electronic structures and elaborate investigation using epitaxial thin films have been carried out.

In Chapter 2, the electronic structures of Sn(II) ternary oxides were theoretically investigated using first-principles calculations. The first-principles calculations were performed on the density functional theory with the projector augmented wave method[37]. The exchange-correlation functional was treated as the HSE06 hybrid functional[38] which had been shown to describe the electronic structure for a variety of semiconductors more accurately than local and semilocal functional.

In Chapter 3, thin films of Sn-*M*-O pyrochlores (*M*=Nb, Ta), SnNb<sub>2</sub>O<sub>6</sub>, and  $\alpha$ -SnWO<sub>4</sub> were fabricated by a pulsed laser deposition method for characterization of their optical and electrical properties. Their orientations were revealed by X-ray diffraction analyses. Optical absorption spectra were obtained from ultraviolet, visible, and near infrared spectroscopy. They were compared to the spectra obtained from the first-principles calculations. Electrical resistivity measurements and X-ray photoelectron spectroscopy were also performed. The results are discussed with their electronic structures.

In Chapter 4, first-principles calculations on the defect formation of SnNb<sub>2</sub>O<sub>6</sub> were performed. Defect formation energies are important factor to predict the possibility of electrical conduction because they may act as pinning of Fermi level and prevent carrier doping. The formation energies of kinds of native defects were calculated and discussed along with the local structures around defects.

## References

- [1] K. Nomura, H. Ohta, A. Takagi, T. Kamiya, M. Hirano and H. Hosono, *Nature* 432 (2004) 488.
- [2] T. Minami, Y. Nishi and T. Miyata, *Thin Solid Films* 549 (2013) 65.
- [3] A. Tsukazaki, A. Ohtomo, T. Onuma, M. Ohtani, T. Makino, M. Sumiya, K. Ohtani, S.F. Chichibu, S. Fuke, Y. Segawa, H. Ohno, H. Koinuma and M. Kawasaki, *Nat. Mater.* 4 (2005) 42.
- [4] R.B.H. Tahar, T. Ban, Y. Ohya and Y. Takahashi, *J. Appl. Phys.* 83 (1998) 2631.
- [5] R.L. Hoffman, B.J. Norris and J.F. Wager, *Appl. Phys. Lett.* 82 (2003) 733.
- [6] S.E. Harrison, *Phys. Rev.* 93 (1954) 52.
- [7] P.S. Patil, R.K. Kwar, T. Seth, D.P. Amalnerkar and P.S. Chigare, *Ceram. Int.* 29 (2003) 725.
- [8] H. Raebiger, S. Lany and A. Zunger, *Phys. Rev. B* 76 (2007).
- [9] H. Kawazoe, M. Yasukawa, H. Hyodo, M. Kurita, H. Yanagi and H. Hosono, *Nature* 389 (1997) 939.
- [10] H. Ohta, K. Kawamura, M. Orita, M. Hirano, N. Sarukura and H. Hosono, *Appl. Phys. Lett.* 77 (2000) 475.
- [11] H. Yanagi, K. Ueda, H. Ohta, M. Orita, M. Hirano and H. Hosono, *Solid State Commun.* 121 (2002) 15.
- [12] Y. Ogo, H. Hiramatsu, K. Nomura, H. Yanagi, T. Kamiya, M. Kimura, M. Hirano and H. Hosono, *Phys. Status Solidi A* 206 (2009) 2187.
- [13] W. Guo, L. Fu, Y. Zhang, K. Zhang, L.Y. Liang, Z.M. Liu, H.T. Cao and X.Q. Pan, *Appl. Phys. Lett.* 96 (2010).

- [14] I. Lefebvre, M.A. Szymanski, J. Olivier-Fourcade and J.C. Jumas, *Phys. Rev. B* 58 (1998) 1896.
- [15] A. Togo, F. Oba, I. Tanaka and K. Tatsumi, *Phys. Rev. B* 74 (2006).
- [16] W. Jeitschko and A.W. Sleight, *Acta Crystallogr. B* 30 (1974).
- [17] Jeitschk.W and A.W. Sleight, *Acta Crystallogr. B* 28 (1972) 3174.
- [18] Donaldso.Jd and D.C. Puxley, *Acta Crystallogr. B* 28 (1972) 864.
- [19] P. Cerny, A.M. Fransolet, T.S. Ercit and R. Chapman, *Can. Mineral* 26 (1988) 889.
- [20] L.P. Cruz, J.M. Savariault, J. Rocha, J.C. Jumas and J.D.P. de Jesus, *J. Solid State Chem.* 156 (2001) 349.
- [21] D.J. Stewart, O. Knop, R.E. Meads and W.G. Parker, *Can. J. Chem.* 51 (1973) 1041.
- [22] H. Mizoguchi, A.W. Sleight and M.A. Subramanian, *Mater. Res. Bull.* 44 (2009) 1022.
- [23] N. Kumada, Y. Yonesaki, T. Takei, N. Kinomura and S. Wada, *Mater. Res. Bull.* 44 (2009) 1298.
- [24] B. Nowitzki and R. Hoppe, *Z. Anorg. Allg. Chem.* 515 (1984).
- [25] R.M. Braun and R. Hoppe, *Z. Anorg. Allg. Chem.* 478 (1981) 7.
- [26] R.M. Braun and R. Hoppe, *Z. Anorg. Allg. Chem.* 485 (1982) 15.
- [27] I.S. Cho, C.H. Kwak, D.W. Kim, S. Lee and K.S. Hong, *J. Phys. Chem. C* 113 (2009) 10647.
- [28] Y. Hosogi, K. Tanabe, H. Kato, H. Kobayashi and A. Kudo, *Chem. Lett.* 33 (2004) 28.
- [29] Y. Uratani, T. Shishidou and T. Oguchi, *Jpn. J. Appl. Phys.* 47 (2008) 7735.
- [30] R. Asahi, T. Morikawa, T. Ohwaki, K. Aoki and Y. Taga, *Science* 293 (2001) 269.
- [31] H. Kominami, K. Oki, M. Kohno, S. Onoue, Y. Kera and B. Ohtani, *J. Mater. Chem.*

11 (2001) 604.

[32] Y. Noda, B. Lee, K. Domen and J.N. Kondo, *Chem. Mater.* 20 (2008) 5361.

[33] Y. Hosogi, Y. Shimodaira, H. Kato, H. Kobayashi and A. Kudo, *Chem. Mater.* 20 (2008) 1299.

[34] M.W. Stoltzfus, P.M. Woodward, R. Seshadri, J.H. Klepeis and B. Bursten, *Inorg. Chem.* 46 (2007) 3839.

[35] L.A. Burton and A. Walsh, *J. Solid State Chem.* 196 (2012) 157.

[36] G. Hautier, A. Miglio, G. Ceder, G.M. Rignanese and X. Gonze, *Nat Commun* 4 (2013) 2292.

[37] P.E. Blochl, *Phys. Rev. B* 50 (1994) 17953.

[38] J. Heyd, G.E. Scuseria and M. Ernzerhof, *J. Chem. Phys.* 118 (2003) 8207.

## Chapter 2

### Electronic structures of Sn(II) ternary oxides

#### 1. Introduction

Tin monoxide (SnO), a prototypical Sn(II) oxide, is known as a *p*-type oxide semiconductor[1,2]. This property is attributed to its unique valence electronic structure associated with the presence of Sn(II) ions. In typical *n*-type oxide semiconductors such as In<sub>2</sub>O<sub>3</sub>, ZnO, and SnO<sub>2</sub>, the relatively deep valence band maximum (VBM) composed mainly of O-2*p* orbitals lead to difficulty in hole doping. On the other hand, SnO has shallow VBM due to the hybridization of O-2*p* and Sn-5*s,p* orbitals[3,4], which encourages hole doping. On the analogy of SnO, such hybridized valence bands is also expected for complex oxides including Sn(II).

The variety of Sn(II) complex oxides is poor partly because of the thermodynamically instable tendency of Sn(II): Sn ions tend to prefer tetravalent in oxides. The partner ions for Sn(II) ternary oxides are limited to high valence ions over tetravalent or alkali metal ions; W<sup>6+</sup>[5,6], S<sup>6+</sup>[7], Nb<sup>5+</sup>[8,9], Ta<sup>5+</sup>[8,10], Ti<sup>4+</sup>[11], Na<sup>+</sup>[12], K<sup>+</sup>[13,14], Rb<sup>+</sup>[14], Cs<sup>+</sup>[14]. Moreover, the number of reports on properties of Sn(II) complex oxides is quite small. While there are a few reports on photocatalytic activity and the band gaps for some of them, most of their fundamental properties are unclear including electrical conductivity.

Meanwhile, several approaches using first-principles calculations have been performed to understand their electronic structures. For example, Y. Hosogi *et al.* have reported that SnNb<sub>2</sub>O<sub>6</sub> exhibits a valence band character similar to that of SnO, *i. e.*, the

VBM states constructed from the hybridization of Sn-5*sp* and O-2*p*[15]. M. Stolzhus *et al.* have shown the same character for  $\beta$ -SnWO<sub>4</sub>[16]. G. Hautier *et al.* have predicted that K<sub>2</sub>Sn<sub>2</sub>O<sub>3</sub> shows relatively a low hole effective mass at VBM with contribution of Sn-5*sp*[17]. However, previous works of first-principles calculations on Sn(II) oxides are sporadic and there have never been systematic ones. In addition, some of them were performed with course approximations to describe band gaps of semiconductors. Therefore, systematic calculations with adequate conditions are demanded to understand the electronic structure of Sn(II) complex oxides and to predict the electrical and optical properties of them. In this chapter, I calculated and compared the electronic structures of SnO and the representative Sn(II) ternary oxides with *d*<sup>0</sup> transition metals; Sn<sub>2</sub>Nb<sub>2</sub>O<sub>7</sub>, Sn<sub>2</sub>Ta<sub>2</sub>O<sub>7</sub>, SnNb<sub>2</sub>O<sub>6</sub>, SnTa<sub>2</sub>O<sub>6</sub>,  $\alpha$ -SnWO<sub>4</sub>,  $\beta$ -SnWO<sub>4</sub>, and Sn<sub>2</sub>TiO<sub>4</sub>.

## 2. Computational procedure

First-principles calculations were performed on the density functional theory (DFT) with the projector augmented wave (PAW) method[18] as implemented in the VASP code[19,20]. The exchange-correlation functional was treated using the generalized gradient approximation (GGA) proposed by Perdew, Burke, and Ernzerhof[21] or as the HSE06 hybrid functional[22]. The hybrid Hartree-Fock density functional approach has been shown to describe electronic structures for a variety of semiconductors more accurately than local and semilocal functional. PAW data sets with radial cutoffs of 1.6, 1.5, 1.5, 1.5, 1.3, and 0.8 Å were used for Sn, Nb, Ta, W, Ti, O, respectively. Their valence electrons were treated as following; Sn  $5s, 5p$ ; Nb  $3p, 4d, 5s$ ; Ta  $5d, 6s$ ; W  $5d, 6s$ ; Ti  $3d, 4s$ ; O  $2s, 2p$ . A plane-wave cutoff energy of 550 eV was employed. Initial structures were prepared using the lattice parameters and internal coordinates listed in the Inorganic Crystal Structure Database (ICSD). The primitive cells and k-point meshes used for the calculations are described in Fig. 1-5. The lattice parameters and internal coordinates were relaxed within their symmetry until the interatomic forces became less than 5 meV/Å.

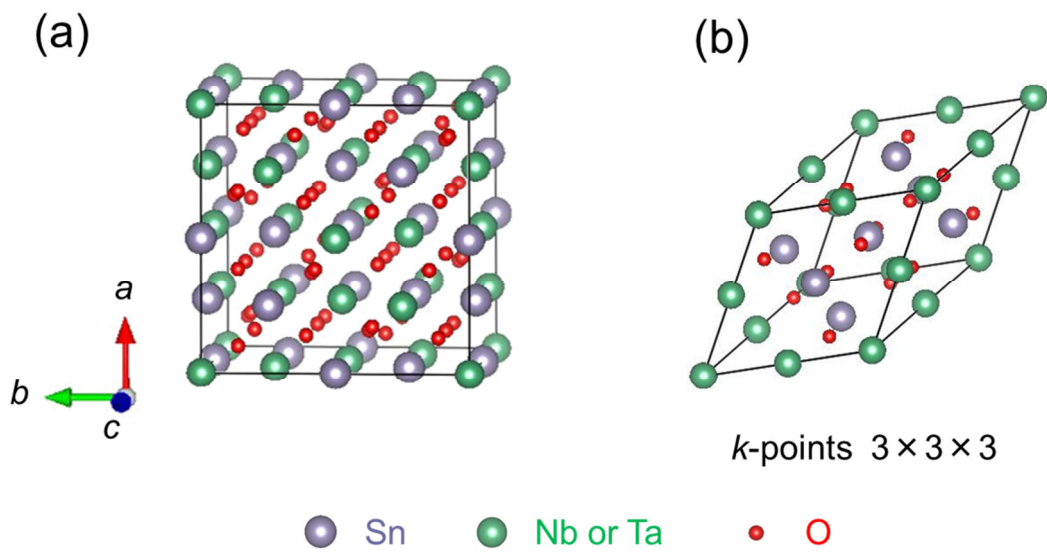


Figure 1 Crystal structure of a Sn- $M$ -O ( $M$ =Nb or Ta) pyrochlore. (a) conventional unit cell and (b) primitive cell used for calculations.

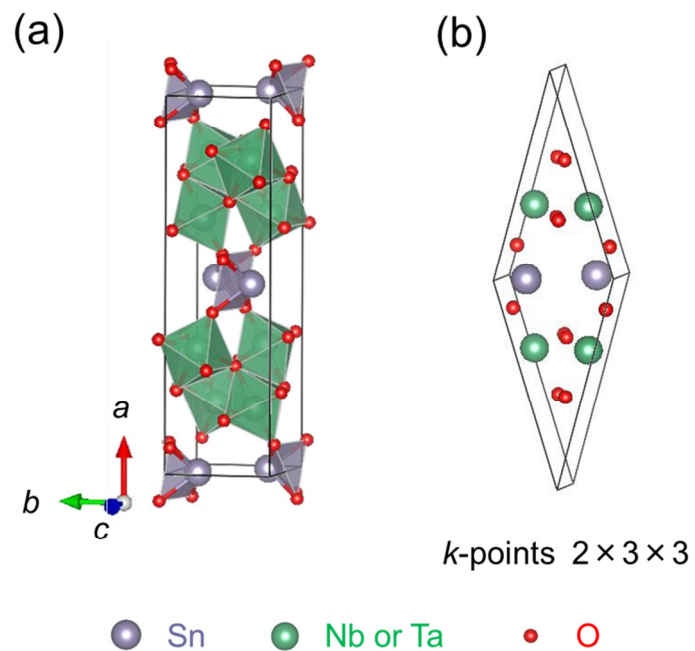


Figure 2 Crystal structure of  $\text{SnM}_2\text{O}_6$  ( $M$ =Nb or Ta) (a) conventional unit cell and (b) primitive cell used for calculations.

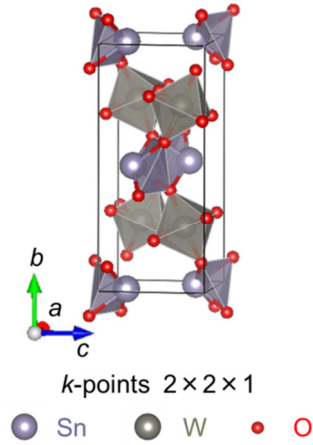


Figure 3 Crystal structure of  $\alpha$ - $\text{SnWO}_4$ , which corresponds to the primitive cell used for calculations.

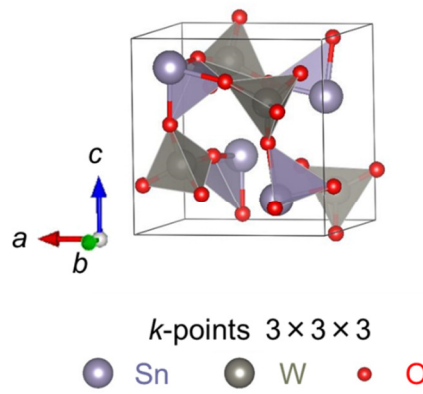


Figure 4 Crystal structure of  $\beta$ - $\text{SnWO}_4$ , which corresponds to the primitive cell used for calculations.

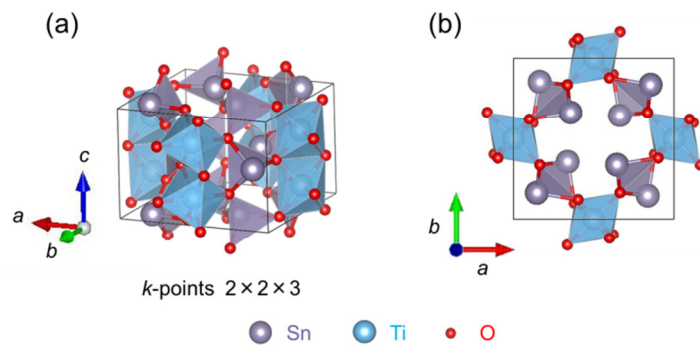


Figure 5 Crystal structure of  $\text{Sn}_2\text{TiO}_4$ . (a) primitive cell used for calculations. (b) projected view along the  $c$  axis.

### 3. Results and discussion

The optimized lattice parameters, band gaps, and formation energies of Sn(II) oxides calculated using GGA-PBE and HSE06 functional are shown in table 1. The references of the formation energies are SnO and Nb<sub>2</sub>O<sub>5</sub>, Ta<sub>2</sub>O<sub>5</sub>, WO<sub>3</sub>, or TiO<sub>2</sub>. The lattice parameters of HSE06 reproduce the experimental values better than those of GGA though both of them overestimate the experimental values. While the predicted band gaps using GGA significantly underestimate the experimental values, the HSE06 calculations reproduce them better, which is typical tendency in PAW calculations using these functional. The calculated band gap for  $\beta$ -SnWO<sub>4</sub> is quite larger than the reported experimental value. Positive formation energies obtained for Sn<sub>2</sub>Nb<sub>2</sub>O<sub>7</sub> and Sn<sub>2</sub>Ta<sub>2</sub>O<sub>7</sub> represents their thermodynamical instability. Additionally, a calculation on the density functional perturbation theory revealed that they showed imaginary phonon modes at  $\Gamma$ -point, which insists they are mechanically unstable as well. This result is consistent with the fact that stoichiometric Sn<sub>2</sub>Nb<sub>2</sub>O<sub>7</sub> and Sn<sub>2</sub>Ta<sub>2</sub>O<sub>7</sub> have never been obtained. Samples fabricated by solid state reaction ordinary include large amount of defects to exhibit significant non-stoichiometry; *e. g.*, Sn<sup>2+</sup><sub>1.62</sub>(Nb<sub>1.86</sub>Sn<sup>4+</sup><sub>0.14</sub>)O<sub>6.55</sub>[23]. The other compounds represent negative formation energies. These results consistently reflect the stability experimentally observed.

Table 1 Lattice parameters, band gaps, and formation energies of the relaxed structures obtained using GGA-PBE and HSE06 functional, respectively. The experimental band gap values are approximated by the absorption thresholds estimated from diffuse reflection measurements on powder samples.

		$a$ (Å)	$b$ (Å)	$c$ (Å)	$E_g$ (eV)		$\Delta E_{\text{form}}$ (eV)
					indirect	direct	
SnNb <sub>2</sub> O <sub>6</sub>	GGA-PBE	17.402	4.9587	5.7066	1.69	1.80	-0.264
	HSE06	17.239	4.9016	5.6320	2.41	2.55	-0.252
	Exp.	17.093	4.877	5.558 [9]	2.3, 2.6 [15,24]		-
Sn <sub>2</sub> Nb <sub>2</sub> O <sub>7</sub>	GGA-PBE	10.741	-	-	0.85	1.06	0.696
	HSE06	10.639	-	-	1.53	1.73	1.16
	Exp.	10.539	-	- [25]	2.3 [15]		-
SnTa <sub>2</sub> O <sub>6</sub>	GGA-PBE	17.446	4.9093	5.6245	2.22	2.24	-0.326
	HSE06	17.249	4.8595	5.5632	2.98	3.01	-0.340
	Exp.	17.113	4.872	5.548 [26]	3.0 [15]		-
Sn <sub>2</sub> Ta <sub>2</sub> O <sub>7</sub>	GGA-PBE	10.706	-	-	1.49	1.64	0.511
	HSE06	10.706	-	-	1.90	2.09	1.04
	Exp.	10.48	-	- [27]	3.0 [15]		-
$\alpha$ -SnWO <sub>4</sub>	GGA-PBE	5.6987	11.829	5.0790	1.34	1.37	-0.135
	HSE06	5.6413	11.696	5.0112	2.12	2.13	-0.126
	Exp.	5.627	11.6486	4.9973 [6]	1.64 - 1.9 [28,29]		-
$\beta$ -SnWO <sub>4</sub>	GGA-PBE	7.5738	-	-	3.73	3.74	-0.140
	HSE06	7.5234	-	-	4.73	4.73	-0.128
	Exp.	7.2989	-	- [5]	2.68 [28]		-
Sn <sub>2</sub> TiO <sub>4</sub>	GGA-PBE	8.6080	8.6080	6.0098	0.95	1.02	-0.050
	HSE06	8.5189	8.5189	5.9210	1.73	1.78	-0.031
	Exp.	8.49	8.49	5.923 [11]	-		-

Before discussing the electronic structures of the ternary oxides, that of SnO is described first. Figure 6 (a) represents the density of states (DOS) of SnO obtained with the HSE06 functional. The origin of energy is set at the VBM. The valence band is roughly divided into three regions. The first region is from the VBM to about -3 eV where Sn-5*sp* and O-2*p* hybridized. In the second one, about -3 to -8 eV, the components of Sn-5*p* and O-2*p* are dominant. The third spreads from -8 eV to -10 eV, where the hybridization of Sn-5*s* and O-2*p* is observed and Sn-5*p* little contribute. The conduction band minimum (CBM) is constructed from mainly Sn-5*p*. This electronic structure can be understood following the previous study on lone-pair compounds[30]. The energy of Sn-5*s* orbital is close to that of O-2*p* orbital, which encourages the interaction between them to form bonding and anti-bonding states. In addition, the anti-bonding states interact with Sn-5*p* resulting in the formation of lone-pair (Fig. 6 (b)). To form this Sn-5*p* hybridization, asymmetric O-coordination around Sn is required because the interaction between Sn-*p* and spherical anti-bonding states is forbidden. As the charge density distribution of VBM states shown in Fig. 7, the lone-pair electrons are found in the space between Sn ions. Figure 8 exhibits the band diagram of SnO. The VBM is located at  $\Gamma$ -point and the CBM is at M-point. The estimated indirect gap of 0.68 eV is consistent with the experimental value of about 0.7 eV[2]. The curvature at the VBM is small in the direction of  $\Gamma$ - to Z-point. This suggests that holes at the valence band move more easily to the interlayer direction than to the intralayer direction.

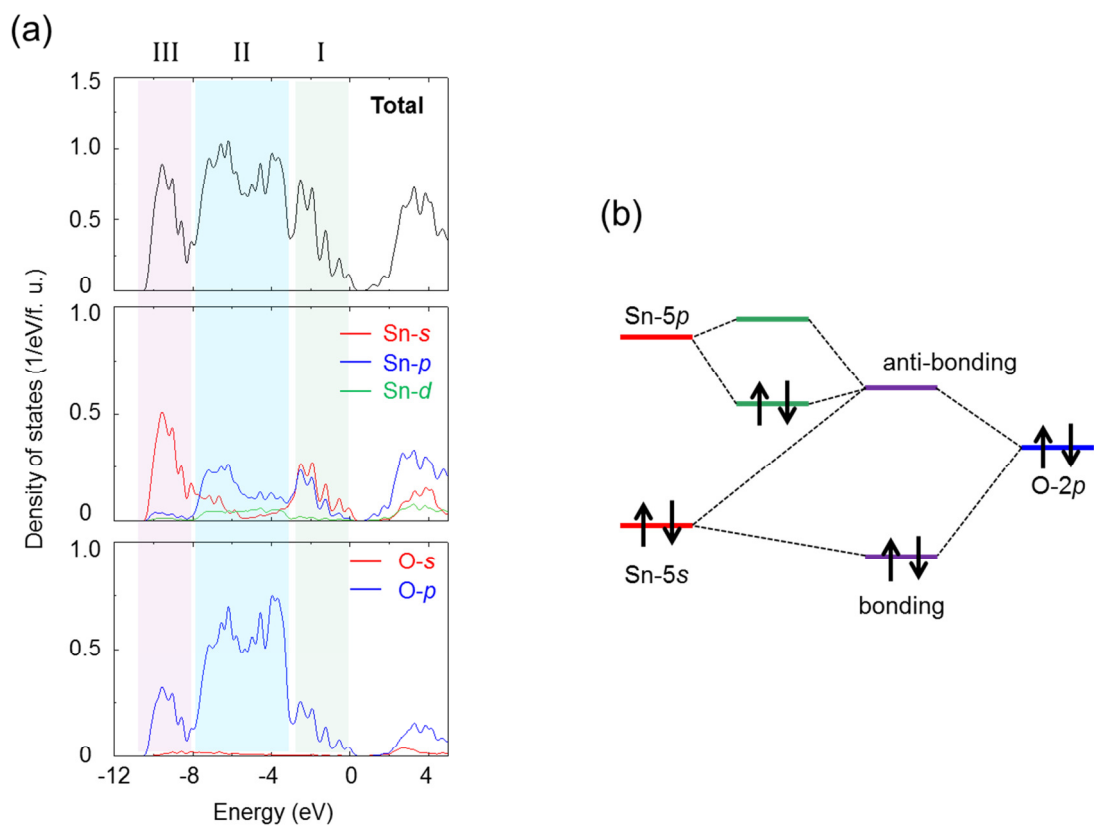


Figure 6 Electronic structure of SnO (a) calculated DOS with HSE06 functional; total DOS (upper), projected DOS for Sn (middle), and projected DOS for O (lower). The origin of the energy is set at VBM. (b) Schematic of the hybridization of Sn-5sp and O-2p.

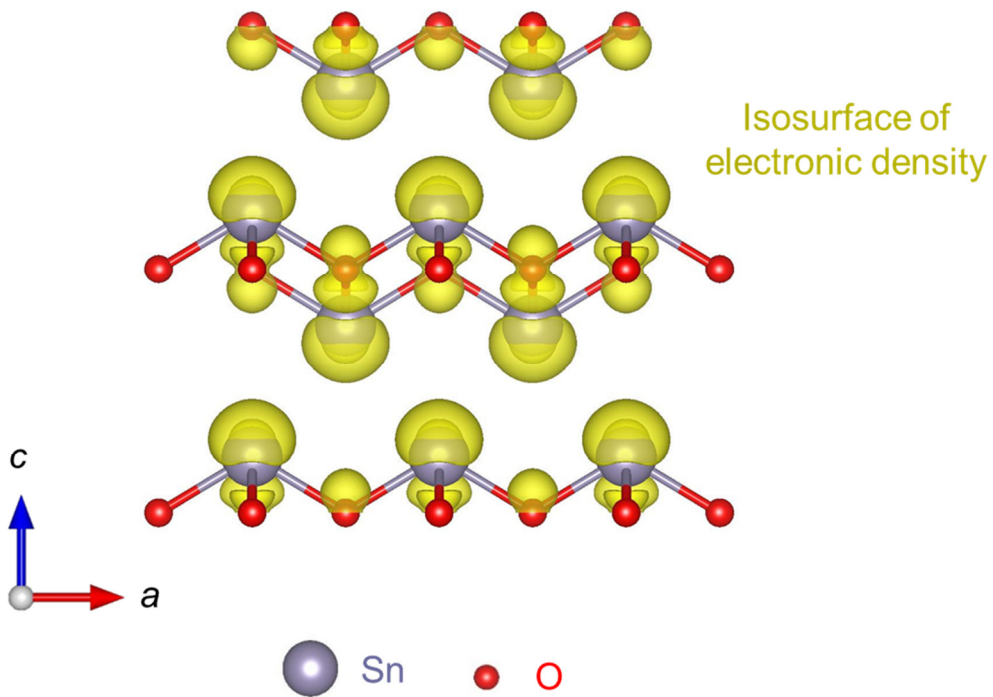
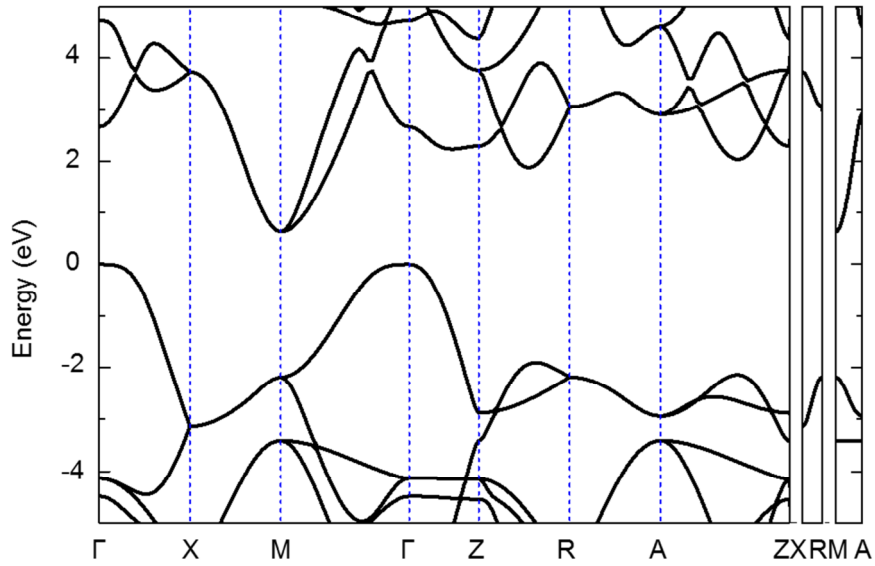


Figure 7 Calculated charge density distributions of electrons occupying the VBM state of SnO. The isosurface of  $0.01 \text{ \AA}^{-3}$  is drawn with yellow color.



	$\times b_1$	$\times b_2$	$\times b_3$	
$\Gamma$	0	0	0	VBM
X	0	1/2	0	
M	1/2	1/2	0	CBM
Z	0	0	1/2	
R	0	1/2	1/2	
A	1/2	1/2	1/2	

Figure 8 Band diagram of SnO calculated using HSE06 functional. The VBM is located at  $\Gamma$ -point and the CBM is at M-point. The origin of the energy is set at the VBM.

Figure 9-12 show DOS of Sn(II) complex oxides obtained using the HSE06. Total DOS and the projected DOS of each element are presented. For all of them, the hybridization of Sn-5*sp* and O-2*p* are found at the VBM, which is similar character to SnO. On the other hand, CBM is constructed mainly from transition metal *d* orbital with small contribution of Sn-*p* and O-*p*. Figure 13-17 show the band diagrams around the band gaps. All of them have indirect-type band structures whose indirect gaps are slightly larger than direct gaps. Some of the VBM or CBM of them are not located at high-symmetry points.

SnNb<sub>2</sub>O<sub>6</sub> and SnTa<sub>2</sub>O<sub>6</sub> have the same crystal structures; stacking structures of Sn-O and Nb-O or Ta-O layers. They show the similar DOS and band structures though their band gaps are different. In the Fig.18, the DOS of SnNb<sub>2</sub>O<sub>6</sub> and SnTa<sub>2</sub>O<sub>6</sub> are compared with those of Nb<sub>2</sub>O<sub>5</sub> and Ta<sub>2</sub>O<sub>5</sub>, respectively. The energies for the DOS of Nb<sub>2</sub>O<sub>5</sub> and Ta<sub>2</sub>O<sub>5</sub> are standardized to align their O-2*s* peak with those of SnNb<sub>2</sub>O<sub>6</sub> and SnTa<sub>2</sub>O<sub>6</sub>, respectively. The electronic structures around the band gaps of SnNb<sub>2</sub>O<sub>6</sub> and SnTa<sub>2</sub>O<sub>6</sub> can be understood as described in Fig. 18: the Sn-5*sp* and O-2*p* hybridized states are inserted just above the valence band of Nb<sub>2</sub>O<sub>5</sub> and Ta<sub>2</sub>O<sub>5</sub>. The bonding states of Sn-5*s* and O-2*p* are also located below the O-2*p* dominant bands. This character is found in the other Sn(II) compounds. The charge density distribution of the VBM states of SnNb<sub>2</sub>O<sub>6</sub> is described in Fig. 19. Within the Sn-O layer, the presence of lone-pair electrons is clearly seen as well as SnO. From the band diagram of SnNb<sub>2</sub>O<sub>6</sub>, it is found that the bands located between -1.7 eV to the VBM are isolated from the lower bands and like mid-gap states. The curvatures at the VBM of SnNb<sub>2</sub>O<sub>6</sub> and SnTa<sub>2</sub>O<sub>6</sub> are small in the direction of Y- to  $\Gamma$ -point which corresponds to interlayer direction. This is against the sense that holes on the VBM which exhibits Sn- and O-orbital characters

seem to be ease to move within the Sn-O layer. It suggests that the small components of Nb- or Ta-*d* at the VBM contribute the transportation over the layers.

$\text{Sn}_2\text{Nb}_2\text{O}_7$  and  $\text{Sn}_2\text{Ta}_2\text{O}_7$  with the same cubic pyrochlore structures represent resemble DOS and band structures. The DOS of them represent a sharp peak at the VBM, which corresponds to the flat bands at the VBM as described in the band diagrams. This can be explained as following. Since Sn-sites in  $\text{Sn}_2\text{Nb}_2\text{O}_7$  and  $\text{Sn}_2\text{Ta}_2\text{O}_7$  are at the center of eight O ions with a high symmetry, the hybridization of the anti-bonding state and Sn-5*p* is forbidden. Indeed, the Sn-*p* components at the VBM is smaller than the other Sn(II) oxides. As the result, the electrons occupying the anti-bonding states at the VBM are concentrated around Sn and O ions. This electrons localization might be associated with the mechanical instability of them. I tried structural optimization after breaking the symmetry by displacing ions. The local structures around Sn(II) after the optimization with and without pyrochlore symmetry are shown in Fig. 20. In the latter structure, the Sn-O bond lengths are scattered and the long bonds are one-sided to create an open space. This asymmetric local structure is considered to be attributed to the formation of lone-pairs.

$\alpha\text{-SnWO}_4$  exhibits a stacking structure with ionic ordering similar to those of  $\text{SnNb}_2\text{O}_6$  and  $\text{SnTa}_2\text{O}_6$  in each layer as shown in Fig. 2 and 3. The DOS feature of the valence bands also resembles to those of  $\text{SnNb}_2\text{O}_6$  and  $\text{SnTa}_2\text{O}_6$ . Its band diagram shows the mid-gap-like states with the Sn-5*sp* contribution near the VBM. On the other hand,  $\beta\text{-SnWO}_4$  looks different: the DOS for both of the valence and conduction bands are composed of narrow scattered peaks. This feature appears in the band diagram as the shape of less dispersed flat bands. This might be attributed to the crystal structure of  $\beta\text{-SnWO}_4$ . It is constructed from corner-sharing tetrahedrons of  $\text{SnO}_3$  and  $\text{WO}_4$  and

these two kinds of tetrahedrons are alternately ordered. As the result, the distance of the same kinds of cations are large, which leads to the less interaction between the same kinds of cations.

The contribution of Sn-5*sp* around the VBM of Sn<sub>2</sub>TiO<sub>4</sub> is seen in a wider range comparing to the other compounds. It spreads from the VBM to about -3 eV. This may reflect the larger Sn concentration of Sn<sub>2</sub>TiO<sub>4</sub> than the others. A previous calculation with HSE06 showed a band gap of 2.04 eV[31], larger than the value of this work, 1.73 eV. Although details of their calculation conditions are not attached, an Sn<sub>2</sub>TiO<sub>4</sub> single crystal is reported to show black color[11], which supports my result. The previous report suggested that the VBM is at  $\Gamma$ - or X-point. In contrast, we found the VBM at low symmetry point between  $\Gamma$ - and X-point with the energy of 0.05 eV lower than those of  $\Gamma$ - and X-point.

The above seven complex oxides are classified into two groups by electronic structures. First is composed of Sn<sub>2</sub>Nb<sub>2</sub>O<sub>7</sub>, Sn<sub>2</sub>Ta<sub>2</sub>O<sub>7</sub>, and  $\beta$ -SnWO<sub>4</sub> which exhibit the flat valence bands. The other is SnNb<sub>2</sub>O<sub>6</sub>, SnTa<sub>2</sub>O<sub>6</sub>,  $\alpha$ -SnWO<sub>4</sub>, and Sn<sub>2</sub>TiO<sub>4</sub> with relatively large dispersed ones. Considering their crystal structures and components of the VBM, the difference is attributed to whether the Sn(II) lone-pairs largely correlate each other or not. The latter compounds are assumed to show a high hole mobility if hole concentration can be increased. In addition, the compounds except for  $\beta$ -SnWO<sub>4</sub> have band gaps in visible region. Although all of them show indirect type band structures, the difference between the indirect- and direct-gaps are small, 0.2 eV for the largest, which indicates the large optical absorption coefficients of them.

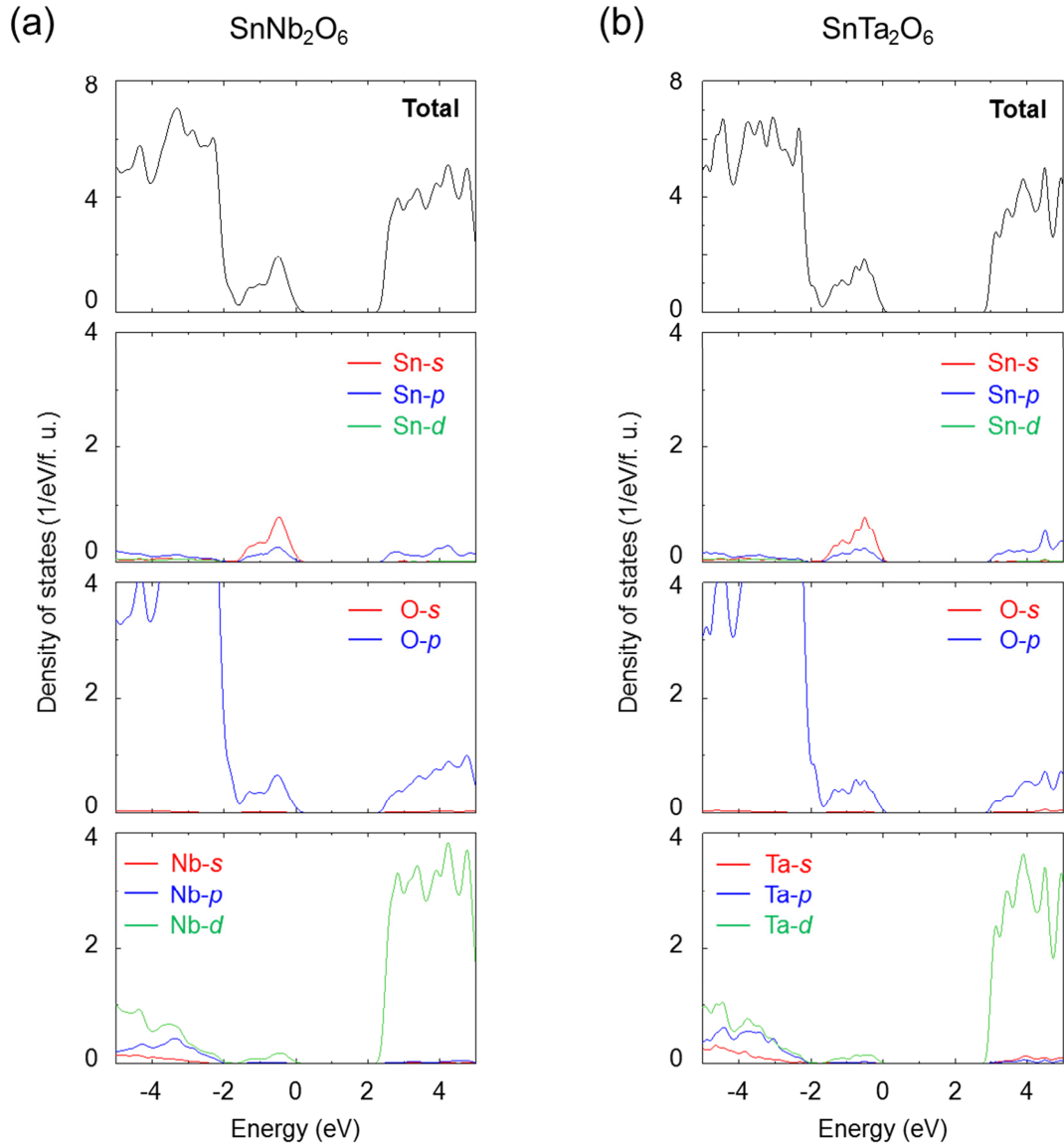


Figure 9 DOS of  $\text{SnM}_2\text{O}_6$  ( $M = \text{Nb}$  or  $\text{Ta}$ ). (a)  $\text{SnNb}_2\text{O}_6$  and (b)  $\text{SnTa}_2\text{O}_6$ . The origin of the energy is set at the VBM.

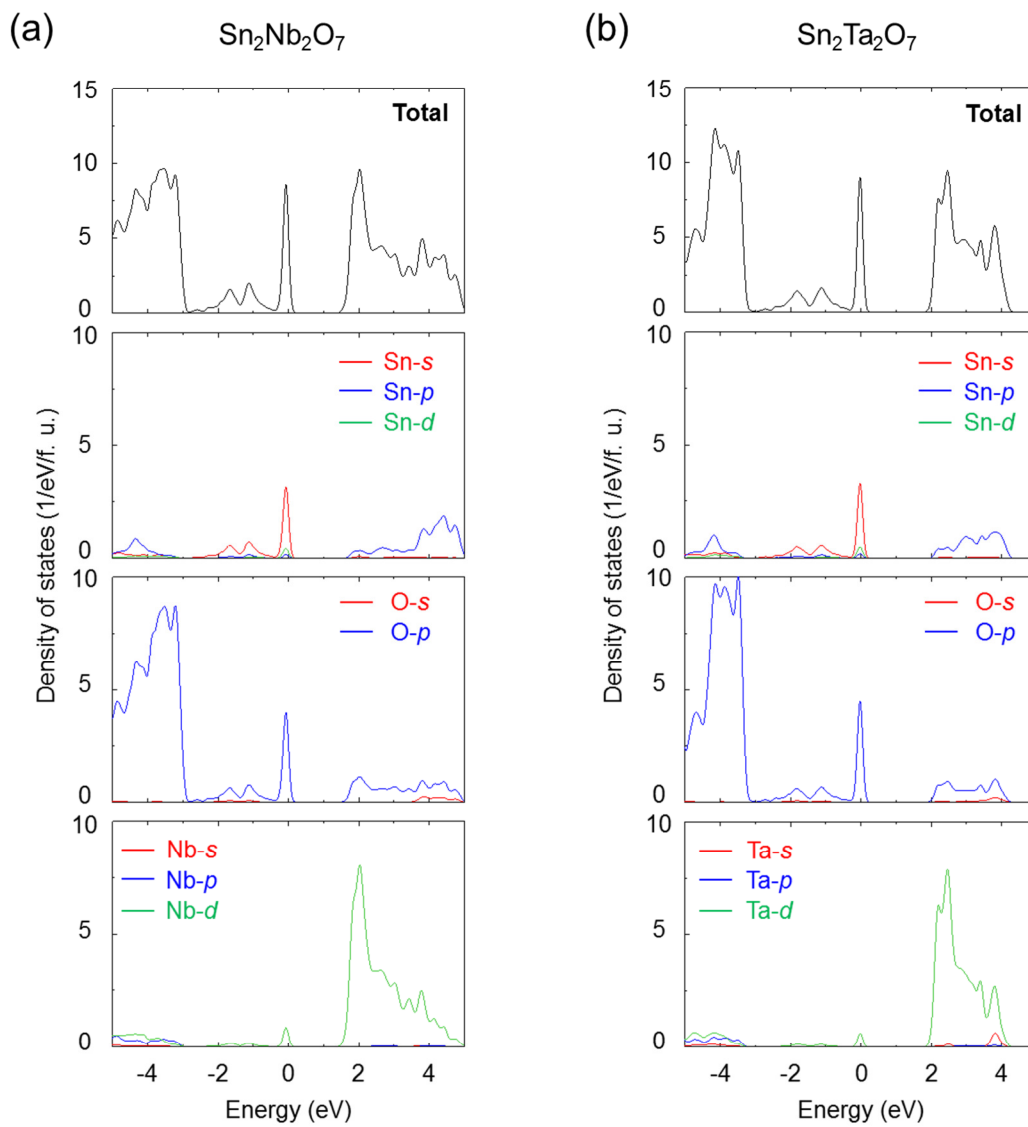


Figure 10 DOS of  $\text{Sn}_2M_2\text{O}_7$  ( $M=\text{Nb}$  or  $\text{Ta}$ ) pyrochlores, (a)  $\text{Sn}_2\text{Nb}_2\text{O}_7$  and (b)  $\text{Sn}_2\text{Ta}_2\text{O}_7$ .

The origin of the energy is set at the VBM.

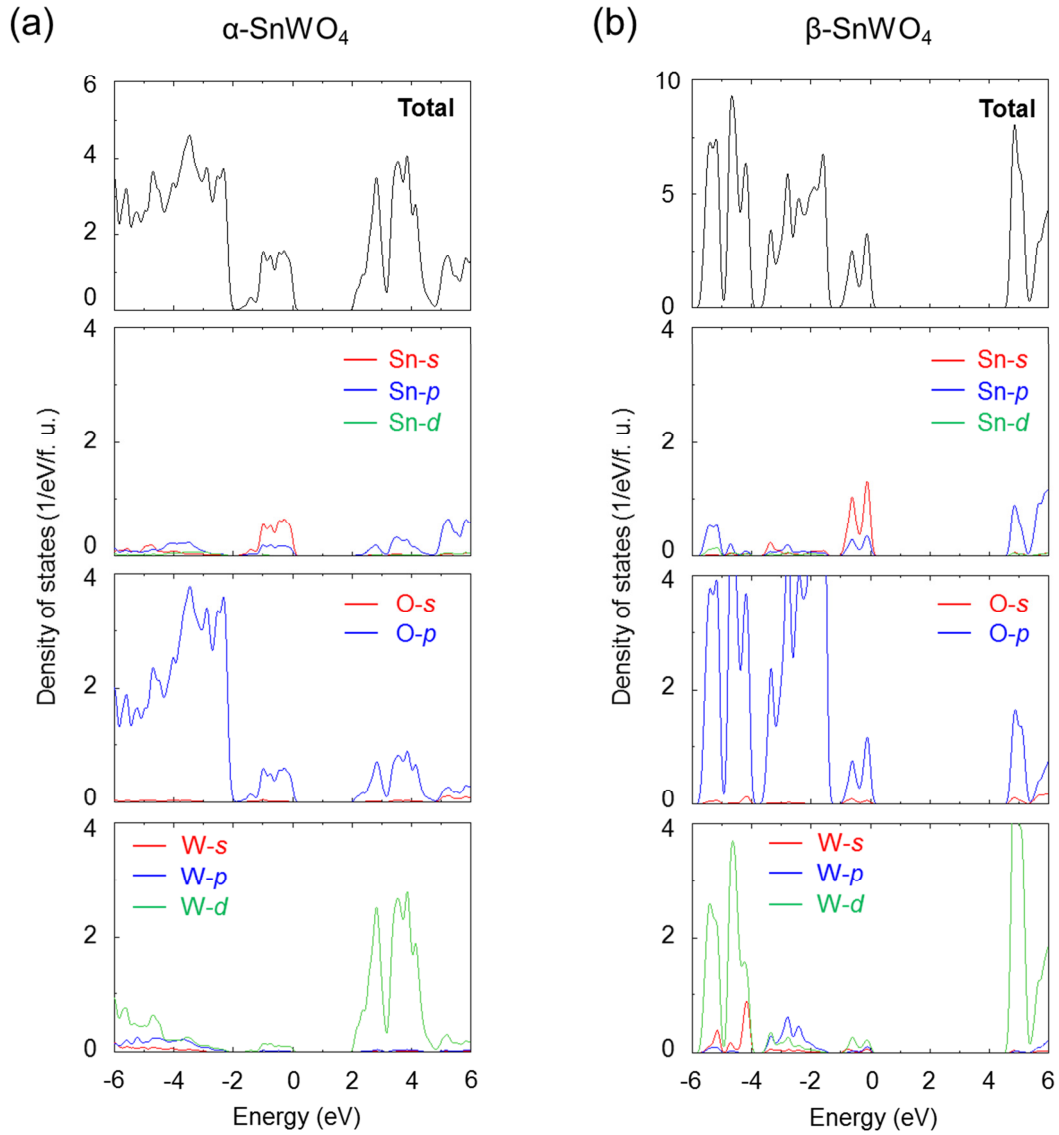


Figure 11 DOS of SnWO<sub>4</sub>. (a)  $\alpha$ -SnWO<sub>4</sub> and (b)  $\beta$ -SnWO<sub>4</sub>. The origin of the energy is set at the VBM.

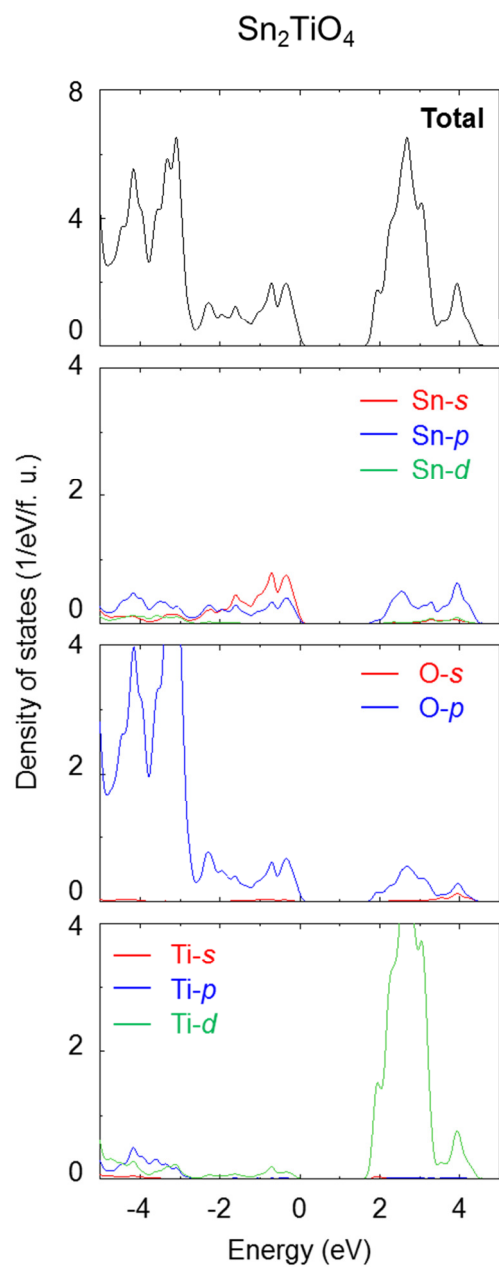
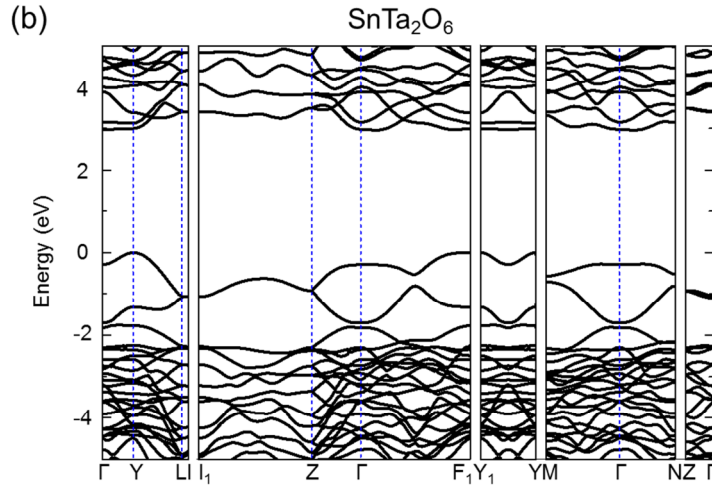
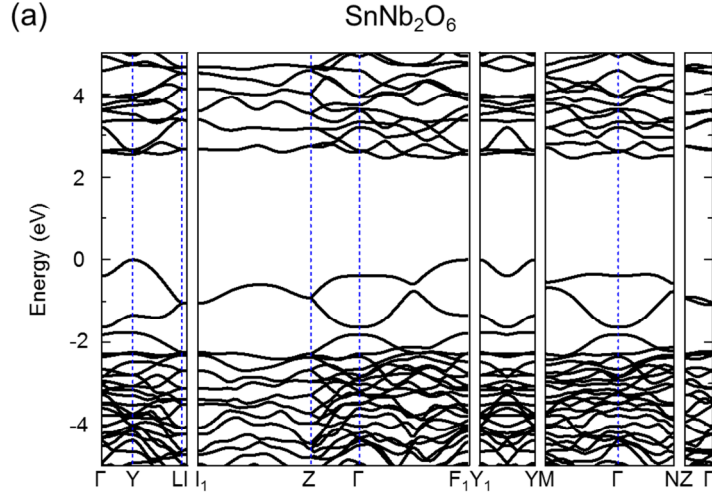


Figure 12 DOS of  $\text{Sn}_2\text{TiO}_4$ . The origin of the energy is set at the VBM.



	$\times b_1$	$\times b_2$	$\times b_3$		$\times b_1$	$\times b_2$	$\times b_3$
$\Gamma$	0	0	0	$F_1$	0.495	0.495	0.509
<b>Y</b>	<b>0.5</b>	<b>0.5</b>	<b>0</b>	<b>VBM</b>	$Y_1$	-0.5	0
L	0.5	0.5	0.5	M	0.5	0	0.5
I	0.495	0.505	0.5	N	0.5	0	0
$I_1$	0.505	-0.505	0.5				
Z	0	0	0.5				

Figure 13 Band diagram of  $\text{SnM}_2\text{O}_6$  ( $M=\text{Nb}$  or  $\text{Ta}$ ). (a)  $\text{SnNb}_2\text{O}_6$  and (b)  $\text{SnTa}_2\text{O}_6$ . The VBM is located at Y-point and the CBM is at a low symmetry point between N- and  $\Gamma$ -points. The origin of the energy is set at the VBM.

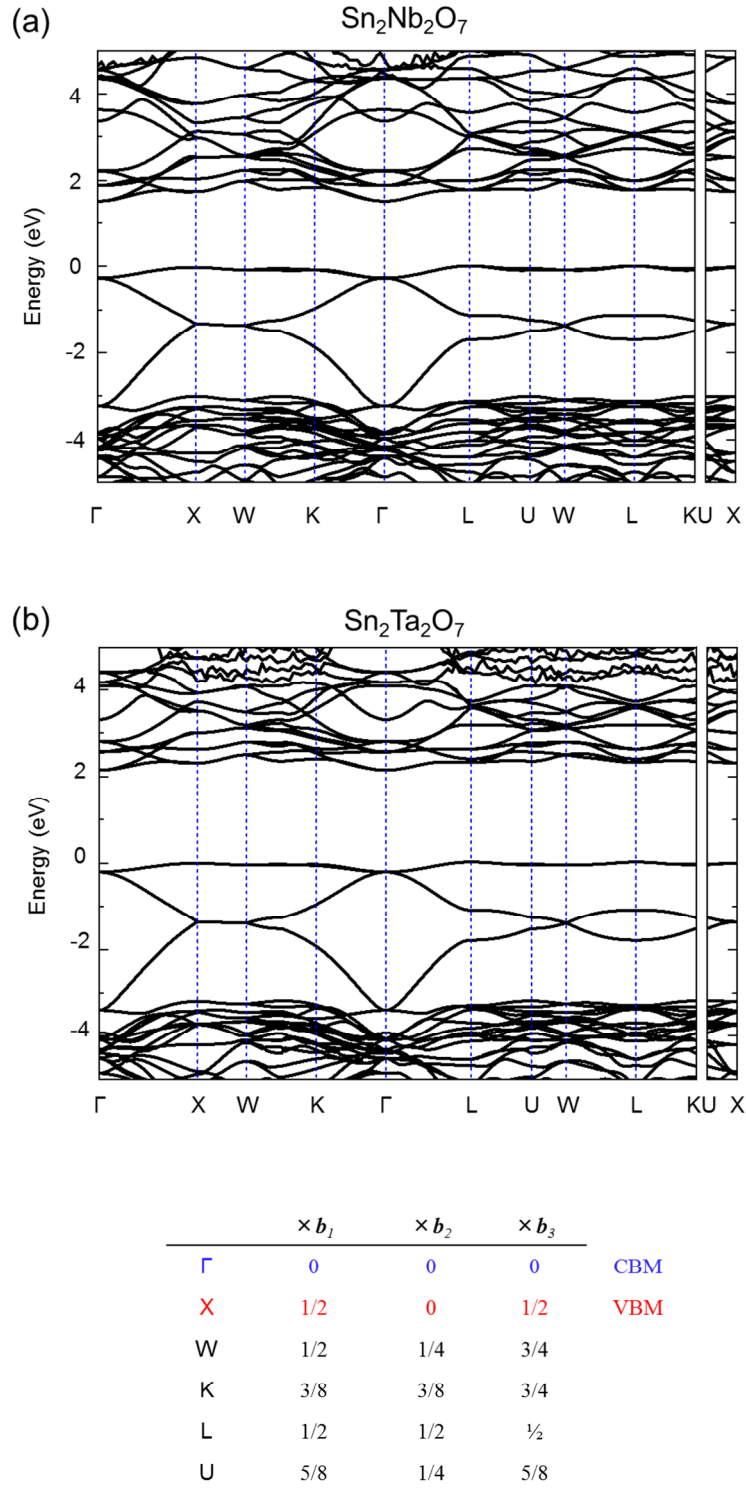
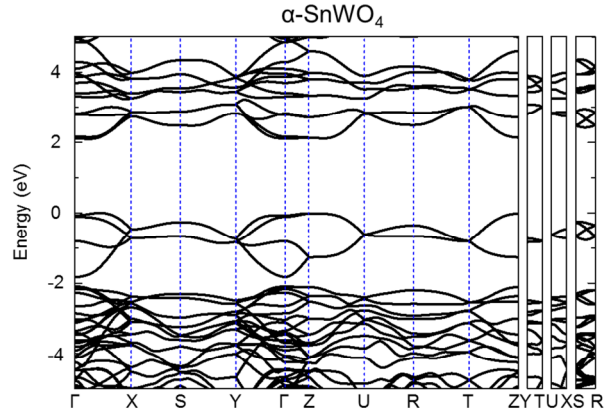
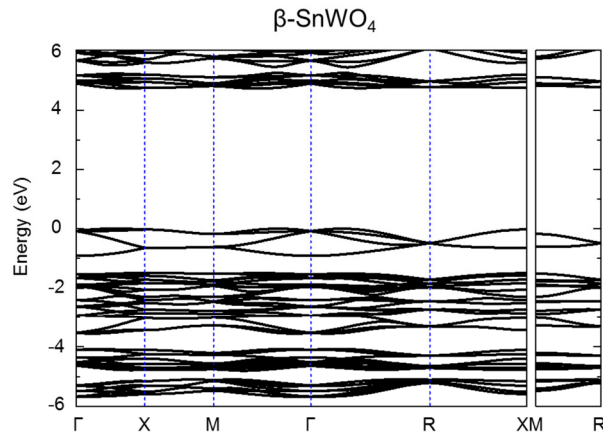


Figure 14 Band diagram of  $\text{Sn}_2M_2\text{O}_7$  ( $M=\text{Nb}$  or  $\text{Ta}$ ), (a)  $\text{Sn}_2\text{Nb}_2\text{O}_7$  and (b)  $\text{Sn}_2\text{Ta}_2\text{O}_7$ . The VBM is located at X-point and the CBM is at  $\Gamma$ -point. The origin of the energy is set at the VBM.



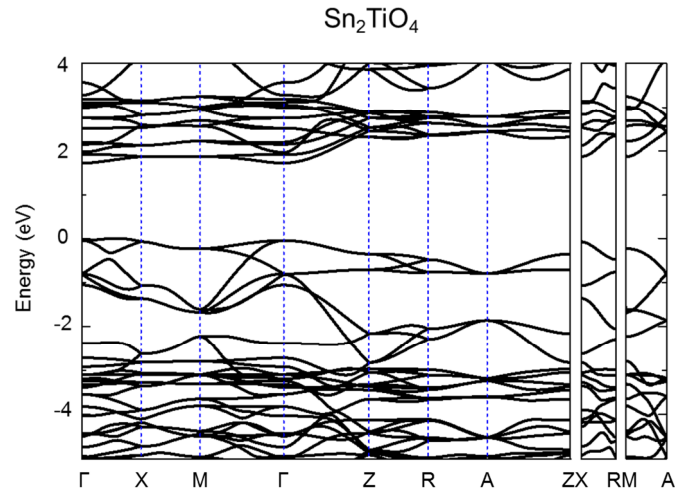
	$\times b_1$	$\times b_2$	$\times b_3$		$\times b_1$	$\times b_2$	$\times b_3$
$\Gamma$	0	0	0	Z	0	0	0.5
X	0.5	0	0	U	0.5	0	0.5
S	0.5	0.5	0	R	0.5	0.5	0.5
Y	0	0.5	0	T	0	0.5	0.5

Figure 15 Band diagram of  $\alpha$ -SnWO<sub>4</sub>. The VBM and CBM are located at a low symmetry points between Y- and  $\Gamma$ -points. The origin of the energy is set at the VBM.



	$\times b_1$	$\times b_2$	$\times b_3$	
$\Gamma$	0	0	0	
X	0	0.5	0	
M	0.5	0.5	0	
R	0.5	0.5	0.5	CBM

Figure 16 Band diagram of  $\beta$ -SnWO<sub>4</sub>. The VBM is located at a low symmetry point between  $\Gamma$ - and X-points and the CBM is at a low symmetry point between  $\Gamma$ - and M-points. The origin of the energy is set at the VBM.



	$\times b_1$	$\times b_2$	$\times b_3$	
$\Gamma$	0	0	0	CBM
X	0	1/2	0	
M	1/2	1/2	0	
Z	0	0	1/2	
R	0	1/2	1/2	
A	1/2	1/2	1/2	

Figure 17 Band diagram of  $\text{Sn}_2\text{TiO}_4$ . The VBM is located at a low symmetry point between  $\Gamma$ - and X- point and the CBM is at  $\Gamma$ -point. The origin of the energy is set at the VBM.

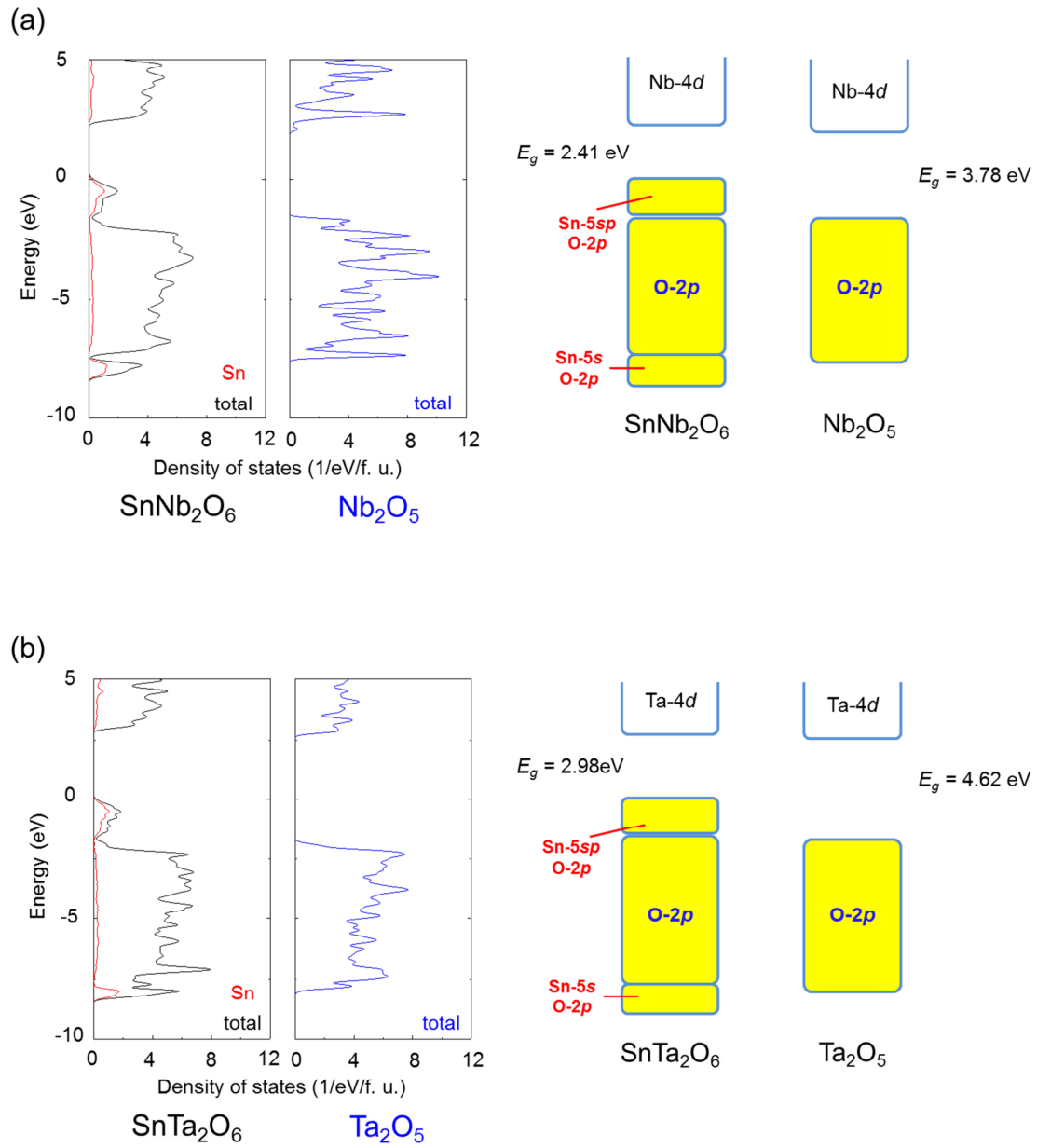


Figure 18 Comparison between the electronic structures of  $\text{SnM}_2\text{O}_6$  and  $\text{M}_2\text{O}_5$  ( $M=\text{Nb}$  or  $\text{Ta}$ ). (a) DOS for  $M=\text{Nb}$  (left) and schematic of band structures (right). (b) those for  $M=\text{Ta}$ .

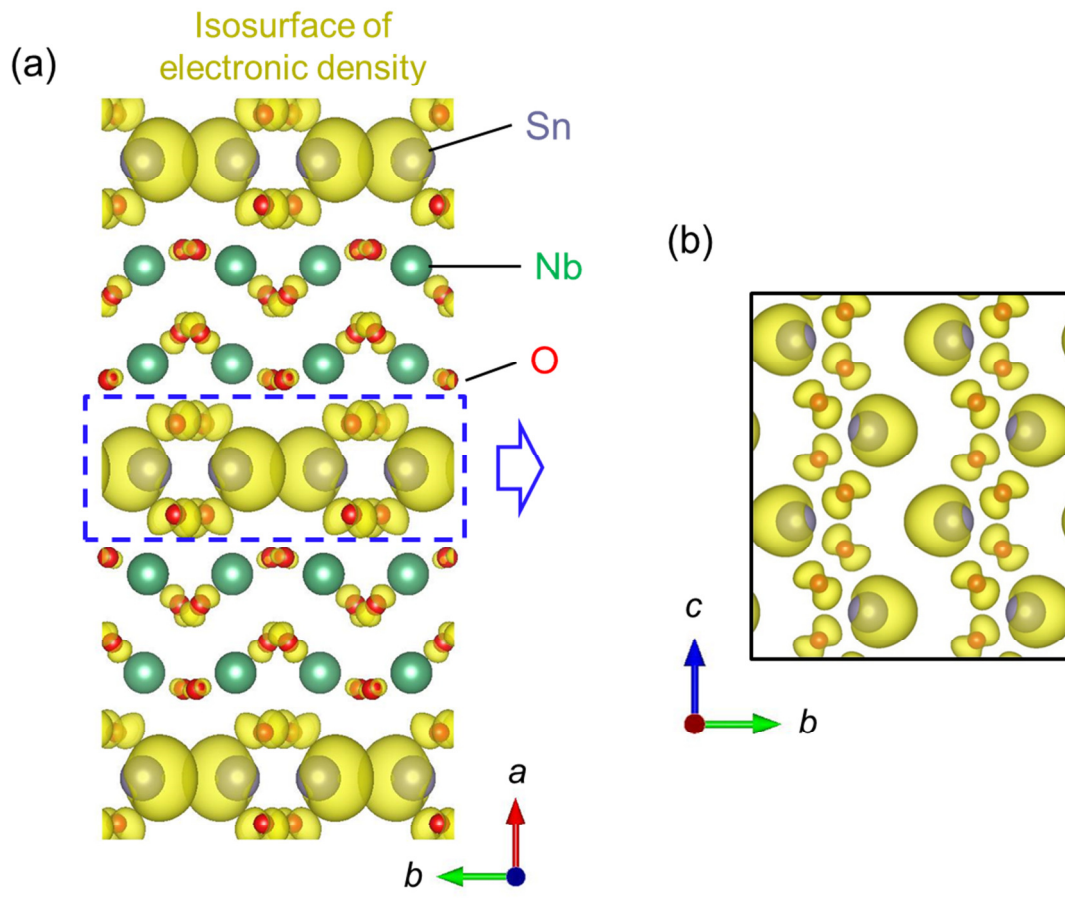


Figure 19 Calculated charge density distributions of electrons at the VBM state for  $\text{SnNb}_2\text{O}_6$ . (a) projected view along  $c$  axis and (b) along  $a$  axis. The isosurface of  $0.003 \text{ \AA}^{-3}$  is drawn with yellow color.

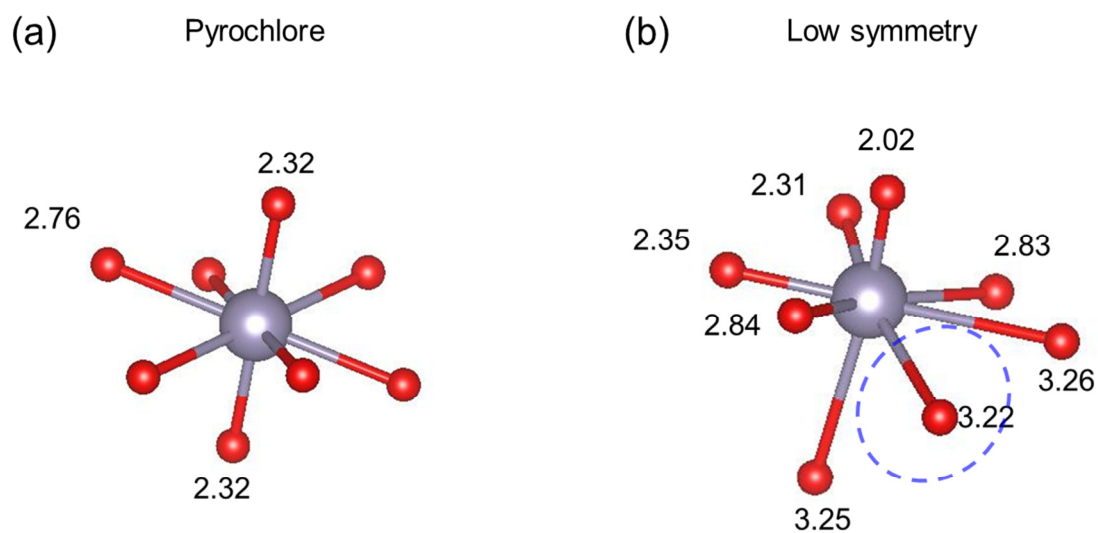


Figure 20 Local structure of Sn-O polyhedron in  $\text{Sn}_2\text{Nb}_2\text{O}_7$  (a) optimized within the symmetry of pyrochlore and (b) optimized after breaking its symmetry. The numbers at the oxygen atoms correspond to the distance from the center Sn atom. For the pyrochlore  $\text{Sn}_2\text{Nb}_2\text{O}_7$ , the lengths of two short bonds are 2.32 Å and the others are 2.76 Å.

#### **4. Conclusion**

The series of calculation confirmed the common trend of Sn(II) complex oxides that their VBM are dominantly composed of the hybridized states of O-2*p* and Sn-5*sp*. The electronic structures reflect their crystal structures; O ions coordination around Sn ions and distance between Sn ions. Relatively large band dispersion at the VBM is observed for the compounds which are considered to exhibit the correlation between Sn lone-pairs; SnNb<sub>2</sub>O<sub>6</sub>, SnTa<sub>2</sub>O<sub>6</sub>, α-SnWO<sub>4</sub>, and Sn<sub>2</sub>TiO<sub>4</sub>. They are assumed to show high hole mobilities if holes could be injected in the valence bands. Most of the Sn(II) ternary oxides have the band gaps corresponding to visible light region. These results indicates the possibility of Sn(II) complex oxides for optoelectronic applications.

## References

- [1] W. Guo, L. Fu, Y. Zhang, K. Zhang, L.Y. Liang, Z.M. Liu, H.T. Cao and X.Q. Pan, *Appl. Phys. Lett.* 96 (2010).
- [2] Y. Ogo, H. Hiramatsu, K. Nomura, H. Yanagi, T. Kamiya, M. Kimura, M. Hirano and H. Hosono, *Phys. Status Solidi A* 206 (2009) 2187.
- [3] I. Lefebvre, M.A. Szymanski, J. Olivier-Fourcade and J.C. Jumas, *Phys. Rev. B* 58 (1998) 1896.
- [4] A. Togo, F. Oba, I. Tanaka and K. Tatsumi, *Phys. Rev. B* 74 (2006).
- [5] Jeitschk.W and A.W. Sleight, *Acta Crystallogr. B* 28 (1972) 3174.
- [6] W. Jeitschko and A.W. Sleight, *Acta Crystallogr. B* 30 (1974).
- [7] Donaldso.Jd and D.C. Puxley, *Acta Crystallogr. B* 28 (1972) 864.
- [8] D.J. Stewart, O. Knop, R.E. Meads and W.G. Parker, *Can. J. Chem.* 51 (1973) 1041.
- [9] P. Cerny, A.M. Fransolet, T.S. Ercit and R. Chapman, *Can. Mineral* 26 (1988) 889.
- [10] H. Mizoguchi, A.W. Sleight and M.A. Subramanian, *Mater. Res. Bull.* 44 (2009) 1022.
- [11] N. Kumada, Y. Yonesaki, T. Takei, N. Kinomura and S. Wada, *Mater. Res. Bull.* 44 (2009) 1298.
- [12] B. Nowitzki and R. Hoppe, *Z. Anorg. Allg. Chem.* 515 (1984).
- [13] R.M. Braun and R. Hoppe, *Z. Anorg. Allg. Chem.* 478 (1981) 7.
- [14] R.M. Braun and R. Hoppe, *Z. Anorg. Allg. Chem.* 485 (1982) 15.
- [15] Y. Hosogi, Y. Shimodaira, H. Kato, H. Kobayashi and A. Kudo, *Chem. Mater.* 20 (2008) 1299.
- [16] M.W. Stoltzfus, P.M. Woodward, R. Seshadri, J.H. Klepeis and B. Bursten, *Inorg.*

Chem. 46 (2007) 3839.

[17] G. Hautier, A. Miglio, G. Ceder, G.M. Rignanese and X. Gonze, Nat Commun 4 (2013) 2292.

[18] P.E. Blochl, Phys. Rev. B 50 (1994) 17953.

[19] G. Kresse and J. Furthmuller, Phys. Rev. B 54 (1996) 11169.

[20] G. Kresse and D. Joubert, Phys. Rev. B 59 (1999) 1758.

[21] J.P. Perdew, K. Burke and M. Ernzerhof, Physical Review Letters 77 (1996) 3865.

[22] J. Heyd, G.E. Scuseria and M. Ernzerhof, J. Chem. Phys. 118 (2003) 8207.

[23] T. Omata, M. Kita, S. Otsuka-Yao-Matsuo and M. Katada, J. Phys. Chem. Solids 66 (2005) 53.

[24] S.J. Liang, S.Y. Zhu, Y. Chen, W.M. Wu, X.C. Wang and L. Wu, J. Mater. Chem. 22 (2012) 2670.

[25] L.P. Cruz, J.M. Savariault, J. Rocha, J.C. Jumas and J.D.P. de Jesus, J. Solid State Chem. 156 (2001) 349.

[26] M.N. V., I.V. V. and B.N. V., Doklady Akademii Nauk SSSR 223 (1975).

[27] M. Gasperin, Cr. Hebd. Acad. Sci. 240 (1955) 2340.

[28] I.S. Cho, C.H. Kwak, D.W. Kim, S. Lee and K.S. Hong, J. Phys. Chem. C 113 (2009) 10647.

[29] Y.G. Su, L.C. Hou, C.F. Du, L.M. Peng, K. Guan and X.J. Wang, Rsc Adv. 2 (2012) 6266.

[30] A. Walsh, D.J. Payne, R.G. Egdell and G.W. Watson, Chem. Soc. Rev. 40 (2011) 4455.

[31] L.A. Burton and A. Walsh, J. Solid State Chem. 196 (2012) 157.

## Chapter 3

# Epitaxial growth and characterization of Sn(II) ternary oxides

### 1. Introduction

Oxides including Sn(II) ions are expected to have unique electronic structures associated with the presence of Sn-5s electrons[1-4]. The valence electronic states of them are constructed from hybridization of Sn-5sp and O-2p orbitals. The hybridization is considered to form wider and shallower valence bands than the O-2p dominant ones which are common for typical metal oxides.

One of the applications expected from such valence bands is a photocatalyst active under visible light irradiation. Some  $d^0$  ions oxides such as TiO<sub>2</sub>, Nb<sub>2</sub>O<sub>5</sub>, and Ta<sub>2</sub>O<sub>5</sub> are well known to exhibit photocatalytic activity[5-7] and studied for water decomposition. Although they have low optical absorption coefficients for visible light because of their wide band gaps, compounds with Sn(II), e. g., Sn<sub>2</sub>TiO<sub>4</sub>, SnNb<sub>2</sub>O<sub>6</sub>, and Sn<sub>2</sub>Ta<sub>2</sub>O<sub>7</sub>, are expected to clear this problem due to the shallow valence band maximum (VBM) states. Indeed, Y. Hosogi *et al.* have shown that SnNb<sub>2</sub>O<sub>6</sub> exhibits a band gap of 2.3 eV and photocatalytic activity for H<sub>2</sub> evolution from an aqueous methanol solution under visible light irradiation[8]. I. S. Cho *et al.* have reported that two polymorphs of SnWO<sub>4</sub>, orthogonal  $\alpha$  phase and cubic  $\beta$  phase, have band gaps of 1.64 eV and 2.68 eV, respectively, and both of them exhibit higher photocatalytic activity for the degradation of a dye solution than that of WO<sub>3</sub>[9]. However, while the photocatalytic activities and band gaps of some Sn(II) compounds have been reported, fundamental optical

properties such as absorption coefficients are not investigated.

Another property associated with the shallow VBM is *p*-type electrical transportation. In typical *n*-type oxide semiconductors such as  $\text{In}_2\text{O}_3$ ,  $\text{ZnO}$ , and  $\text{SnO}_2$ , the relatively deep VBM composed of mainly O-2*p* orbitals leads to difficulty in hole doping. In contrast, Sn(II) oxides have advantage in this point. Indeed, tin monoxide ( $\text{SnO}$ ), the prototypical Sn(II) oxide, is known as a typical *p*-type conductive oxide due to the shallow VBM which encourages a hole doping[10,11]. This is analogous to cuprite ( $\text{Cu}_2\text{O}$ ) as a representative *p*-type oxide semiconductor, where the hybridization of the O-2*p* and Cu-3*d* orbitals occurs around the VBM[12]. While thin film growth of *p*-type semiconductors containing Cu(I), such as  $\text{CuInO}_2$  and  $\text{SrCu}_2\text{O}_2$ , have been studied for device developments[13,14], previous reports on the fabrication of Sn(II) complex oxides are mainly in the bulk or powder form[15-17]. Additionally, the reported electrical transportation properties of Sn(II) complex oxides are limited in a few reports on  $\text{SnWO}_4$ [18]. Therefore, I aim to investigate the potential of optoelectronic applications based on ternary oxides with Sn(II) and provide a thin film growth process of them.

Sn(II) oxides tend to exhibit unique crystal structures, in addition to the electronic structures, due to the formation of lone-pairs in similar manners found in some Pb(II), Sb(III), and Bi(III) compounds[19-21]. Among Sn(II) oxides,  $\text{SnNb}_2\text{O}_6$  and  $\alpha\text{-SnWO}_4$  have characteristic crystal structures worth noting. The crystal structures of them are drawn in Fig. 1 and Fig. 2. They have similar stacking structure of Sn-O layer and Nb-O or W-O layer; the Sn-O layers with the ionic ordering similar to  $\text{SnO}$  (110) and the Nb-O layers or W-O layers with the rutile (101)-like ordering.

Optical and electrical properties emerging due to such two dimensional Sn-O and/or TM-O structures are of special interest among Sn(II) oxides.

In this chapter, I report the characterization of optical and electrical properties of Sn(II) complex oxides using single-phase epitaxial thin films grown by pulsed laser deposition (PLD) method. I tried to fabricate the films of Sn-Nb-O and Sn-Ta-O cubic pyrochlore phases,  $\text{SnNb}_2\text{O}_6$ ,  $\text{SnTa}_2\text{O}_6$ , two forms of  $\text{SnWO}_4$ , and  $\text{Sn}_2\text{TiO}_4$ . Among them,  $\text{SnTa}_2\text{O}_6$ ,  $\beta\text{-SnWO}_4$ , and  $\text{Sn}_2\text{TiO}_4$  thin films could not be obtained. Here, I show the results on the other four phases; Sn-Nb-O and Sn-Ta-O pyrochlore,  $\text{SnNb}_2\text{O}_6$ , and  $\alpha\text{-SnWO}_4$ .

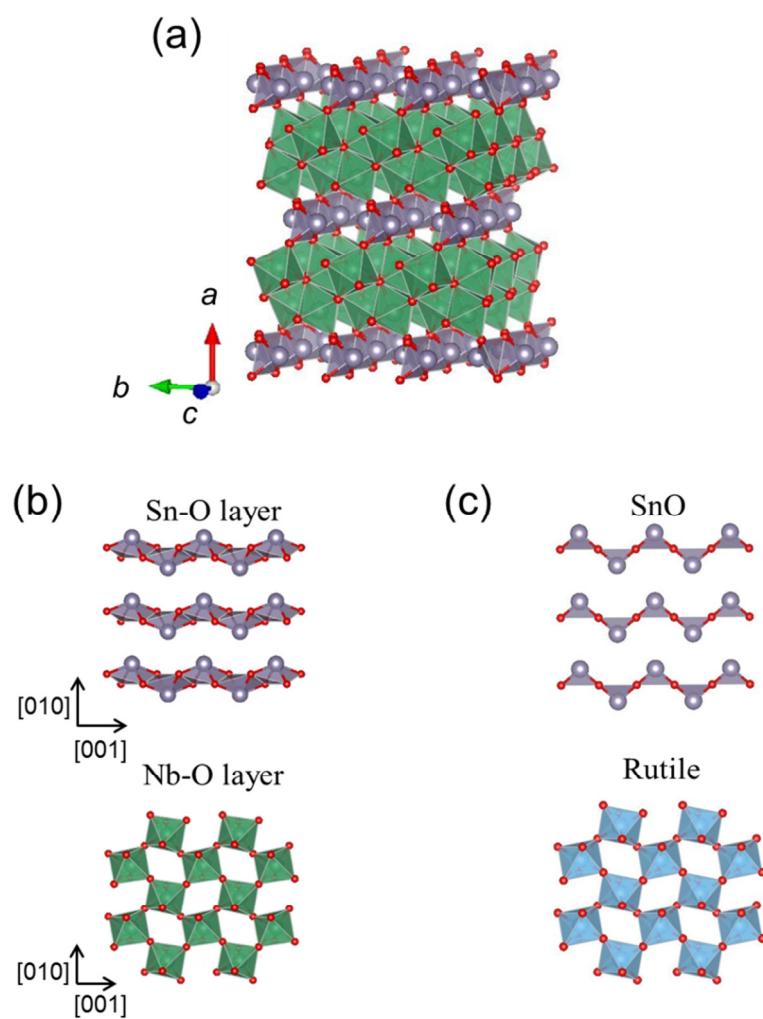


Figure 1 Crystal structure of  $\text{SnNb}_2\text{O}_6$ . (a) perspective view, (b) projected view of Sn-O layer (upper) and Nb-O layer (lower) along  $a$  axis, and (c) projected view of SnO (110) (upper) and rutile-structure (101) (lower).

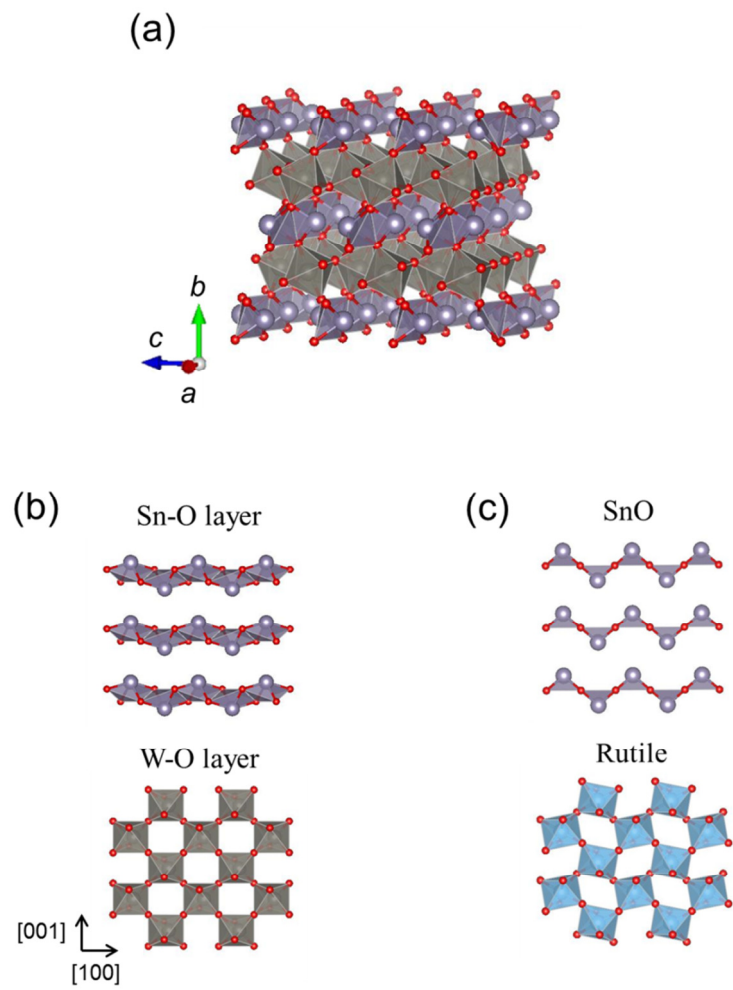


Figure 2 Crystal structure of  $\alpha$ - $\text{SnWO}_4$ . (a) perspective view (b) projected view of Sn-O layer (upper) and W-O layer (lower) along  $a$  axis, and (c) projected view of SnO (110) (upper) and rutile-structure (101) (lower).

## 2. Experiments

Sn-*M*-O pyrochlores (*M*=Nb, Ta), SnNb<sub>2</sub>O<sub>6</sub>, and α-SnWO<sub>4</sub> thin films were fabricated by PLD using a KrF excimer laser ( $\lambda = 248$  nm,  $\tau = 25$  ns, Lambda Physik COMPex205). Sintered compacts of Sn<sub>2</sub>Nb<sub>2</sub>O<sub>7</sub>, Sn<sub>2</sub>Ta<sub>2</sub>O<sub>7</sub>, and α-SnWO<sub>4</sub> prepared by hot isostatic pressing were used as targets. The laser energy density of 1.5 J/cm<sup>2</sup>, the spot size of 2.0 mm<sup>2</sup>, and the pulse frequency of 5 Hz were used. The target-substrate distance was 65 mm. Pressure in the chamber was kept at  $1.0 \times 10^{-4}$  Torr for the pyrochlores and SnNb<sub>2</sub>O<sub>6</sub>, and at  $7.0 \times 10^{-3}$  Torr for α-SnWO<sub>4</sub> by flowing oxygen gas during the deposition. The back pressure was less than  $1 \times 10^{-6}$  Torr. The substrate temperature was kept at 773 K for all of them. After the deposition, gas flow was stopped and the samples were cooled to room temperature in the chamber. Substrates for epitaxial growth were chosen as below.

For growth of Sn-*M*-O pyrochlores, yttria-stabilized-zirconia (YSZ) (100) single crystals (Crystal Base, Co., Ltd.) were used because both of them exhibit fluorite-related crystal structure. The lattice parameter of YSZ is 5.21 Å which is close to the half of those of Sn-Nb-O and Sn-Ta-O pyrochlores ( $a=10.539$  Å[17] and 10.48 Å[22], respectively). The lattice mismatches are about 1 % assuming the twice of  $a_{\text{YSZ}}$  as its lattice periodicity. For growth of SnNb<sub>2</sub>O<sub>6</sub> and α-SnWO<sub>4</sub>, a suitable substrate was explored with a focus on their stacking structures. As mentioned above, they are constructed from stacks of SnO (110)-like layers and rutile (101)-like layers. Although (110) oriented SnO thin film has never been reported, epitaxial growth of rutile-TiO<sub>2</sub> (101) / Al<sub>2</sub>O<sub>3</sub> (01 $\bar{1}$ 2) and SnO<sub>2</sub> (101) / Al<sub>2</sub>O<sub>3</sub> (01 $\bar{1}$ 2) were reported[23,24]. Therefore, Al<sub>2</sub>O<sub>3</sub> (01 $\bar{1}$ 2) single crystals (Shinkosha, Co., Ltd.) were chosen as substrates expecting the SnNb<sub>2</sub>O<sub>6</sub> (100) and α-SnWO<sub>4</sub> (010) oriented epitaxial growth.

The crystal structures and orientations of the thin films were investigated by five-axis X-ray diffraction (XRD) on a Rigaku SmartLab (Cu- $K\alpha_1$ , 40 kV, 30 mA) with an asymmetric Ge (111) two-crystal incidence monochromator. The compositions of the thin films were measured using a wavelength-dispersive X-ray spectrum (WDS) analyzer (Oxford instruments INCA Wave-500) on a scanning electron microscope (Hitachi S-3500H). The film thickness, surface roughness, and density were estimated by an X-ray reflectivity analysis. The surface morphologies of the thin films were observed using an atomic force microscope (AFM) (Shimadzu SPM-9700). The optical transmittance and reflectance spectra were obtained with the use of a Shimadzu Solid Spec-3700DUV. The absorption coefficients ( $\alpha$ ) of the thin films were evaluated from them in consideration of light interference and multiple reflections at the surfaces and the interface. X-ray photoelectron spectroscopy was performed on the films using Al- $K\alpha$  radiation ( $h\nu=1486$  eV) on a JEOL JPS-9010TRX. The energy calibration for insulating samples was performed using C-1s peak of surface contamination because they exhibit energy shift caused by charge-up during measurements. The resistivities of the films were measured by van der Pauw method using a Toyo Corporation Resitest8300.

### 3. Epitaxial growth of Sn(II) ternary oxides with Nb, Ta, and W

#### A. Sn-*M*-O (*M*=Nb, Ta) with a pyrochlore structure

The atomic ratios of Sn to *M* (Sn/*M*) (*M*=Nb, Ta) of the thin films fabricated at different substrate temperatures are shown in Fig. 3. All of the films represent lower Sn/*M* ratios than those of the targets whose designed ratios are 1.0. This is attributed to the differences in the evaporation ratio from the growth front and/or in spatial plume distribution between Sn and Nb or Ta. A higher substrate temperature leads to a lower Sn/*M* and the Sn contents are close to zero at 973 K. The films fabricated at 773 and 873 K are single pyrochlore phases as shown later, despite the lower Sn content than the stoichiometric composition of Sn/*M* = 1. These results are in line with a previous report by L. Cruz *et al.*, showing that the pyrochlore structure can be maintained even when the Sn-Nb-O compound involved a large amount of tin(II)-site vacancies, *e. g.*, about 30% for  $\text{Sn}^{2+}_{1.4}(\text{Nb}_{1.8}\text{Sn}^{4+}_{0.2})\text{O}_{6.3}$ [17].

$2\theta$ -XRD profiles of the Sn-*M*-O thin films are shown in Fig. 4. The peaks of the 773 K- and 873 K-grown samples are ascribed to the *h*00 diffractions of the films with pyrochlore-type structure and the YSZ substrates. On the other hand, the profiles of the 973 K samples show other peaks, 36.52 and 38.26 degrees for the Sn-Nb-O film and 28.25 and 36.56 degrees for Sn-Ta-O film. These peaks and the results of composition analyses suggest the presence of Nb<sub>2</sub>O<sub>5</sub> and/or NbO<sub>2</sub> in the Sn-Nb-O film and Ta<sub>2</sub>O<sub>5</sub> in the Sn-Ta-O film. It should be noted that Sn/*M* in some of the films are only ~0.5 which are close to that in Sn*M*<sub>2</sub>O<sub>6</sub>.  $\beta$ -pyrochlore type AB<sub>2</sub>O<sub>6</sub> is known as a cubic phase with A/B = 0.5, as exemplified by K(Nb,W)O<sub>6</sub> and RbOs<sub>2</sub>O<sub>6</sub> [25,26]. In contrast, the crystal structures of the films are indicated to be a normal pyrochlore type from the extinction rule. Previously, it is reported that a non-stoichiometric compound of

$\text{Sn}^{2+}_{1.4}(\text{Nb}_{1.8}\text{Sn}^{4+}_{0.2})\text{O}_{6.3}$  has a normal pyrochlore type structure but involves Sn atoms occupying Wyckoff positions different from those of the ideal  $\text{Sn}_2\text{Nb}_2\text{O}_7$  pyrochlore [17]. Although it is difficult to determine the internal coordinates and occupancies of ions in our thin films from XRD analyses, such a change in the atomic positions could have occurred due to a large amount of non-stoichiometry.

The out-of-plane lattice constants are estimated to be 10.60 and 10.54 Å for the 773 K samples of Sn-Nb-O and Sn-Ta-O, respectively, which are close to the values reported for bulk samples [16,17,22]. There are clear fringe structures around the 400 peaks of the both 773 K films. The 400 peaks of both films shows 0.10 degrees of a full width at half maximum (FWHM) in the rocking curves. These results indicate small distribution of the out-of-plane lattice constants and high orientations of the films. From the oscillation cycles of the fringe structures, the thicknesses were estimated to be 20 nm for both of them. Figure 5 shows reciprocal space maps around the 622 diffractions of the Sn-M-O pyrochlores and the 311 diffraction of the substrate for the 773 K samples. The cube-on-cube in-plane orientation relationship is indicated. The in-plane coordinates of the diffraction spots of the thin films are not coincident with those of the substrates. Additionally, the spots of the films are shifted from the dashed line on which a 622 diffraction of the undistorted cubic crystal must be. These results suggest that the films are partially relaxed from the strain induced in the epitaxial growth and still slightly distorted to be tetragonal. The in-plane lattice constants for both of the films are estimated to be 10.5 Å. The cube-on-cube in-plane orientation relationships between the thin films and the substrates are also confirmed by XRD  $\phi$ -scan measurements on the 222 diffraction of the films as described in Fig. 6.

Figure 7 shows the AFM images of (a) the YSZ substrate and (b-d) the

Sn-Nb-O thin films obtained in an area of  $3\ \mu\text{m} \times 3\ \mu\text{m}$ . Those of the Sn-Ta-O thin films are presented in Fig. 8 (b-d). In contrast to the flat surface of the 773 K films, granular morphologies are observed for the films fabricated at higher substrate temperature. Root-mean-square (RMS) surface roughnesses are estimated to be 0.1 nm for the YSZ substrate, 0.2, 2.4, and 4.4 nm for the Sn-Nb-O films of 773 K, 873 K, and 973 K, and 0.3, 0.5, and 1.7 nm for the Sn-Ta-O films of 773 K, 873 K, and 973 K, respectively. Qualitatively consistent results are obtained from the X-ray reflectivity measurements.

Figure 9 represents an X-ray reflectivity profiles of the 773 K films with simulated profiles by the Parratt's method [27]. The parameters used in the simulation are a thickness of 20 nm, a density of  $5.5\ \text{g}/\text{cm}^3$ , and a RMS surface roughness of 0.4 nm for the Sn-Nb-O film. A thickness of 21 nm, a density of  $7.8\ \text{g}/\text{cm}^3$ , and a surface roughness of 0.6 nm are used for the Sn-Ta-O film. These parameters yield the best fit to the experimental profiles. The obtained values of the film thickness are consistent with those estimated by the XRD measurements.

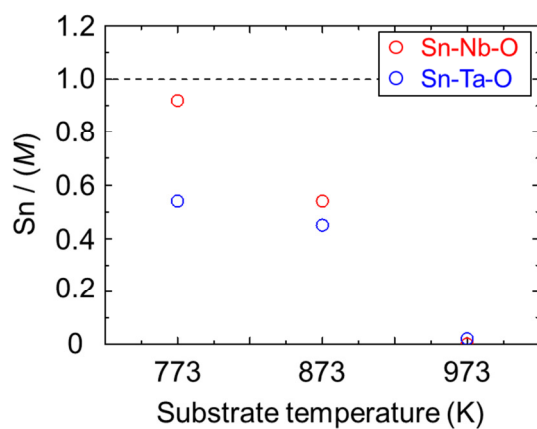


Figure 3 Sn/M ratios ( $M=Nb$  or  $Ta$ ) of the Sn- $M$ -O thin films fabricated on the YSZ substrate at different substrate temperature estimated by SEM-WDX.

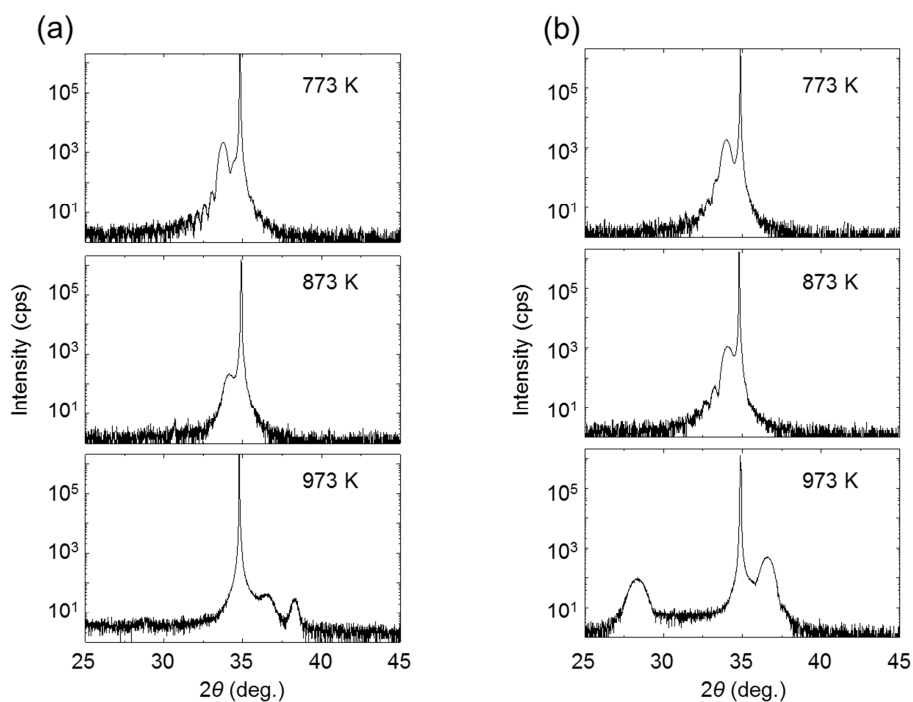


Figure 4 XRD  $2\theta$ - $\theta$  profiles of the Sn- $M$ -O ( $M=Nb$  or  $Ta$ ) thin films fabricated at different substrate temperature. (a)  $M=Nb$  and (b)  $M=Ta$ .

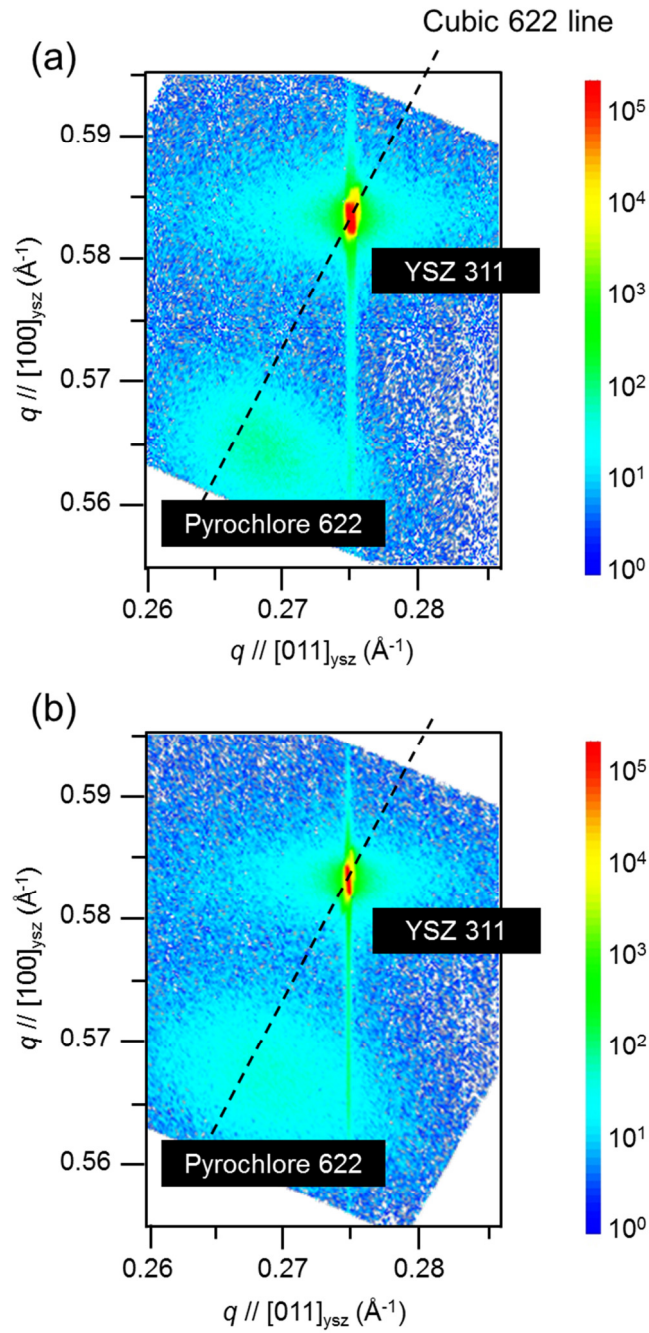


Figure 5 Reciprocal space mapping around the 622 diffractions of the Sn- $M$ -O ( $M=\text{Nb}$  or Ta) thin films fabricated at 773 K. (a)  $M=\text{Nb}$  and (b)  $M=\text{Ta}$ . The dashed lines denote the positions of the 622 diffractions for an ideal, undistorted cubic crystal.

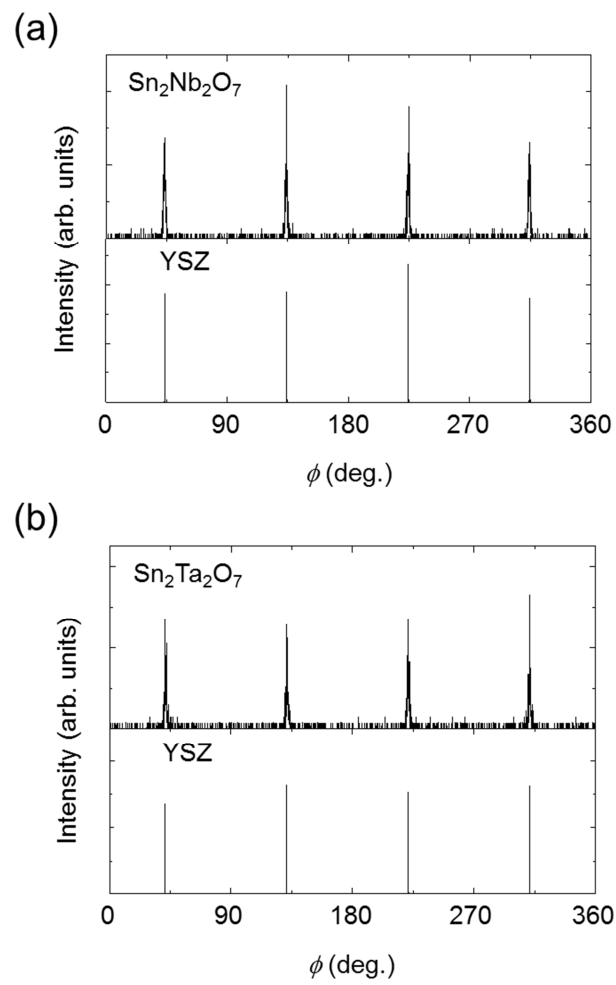


Figure 6 XRD  $\phi$  profiles of the 222 diffractions of the Sn- $M$ -O ( $M$ =Nb or Ta) thin films fabricated at 773 K and 111 diffractions of the YSZ substrate. (a)  $M$ =Nb and (b)  $M$ =Ta.

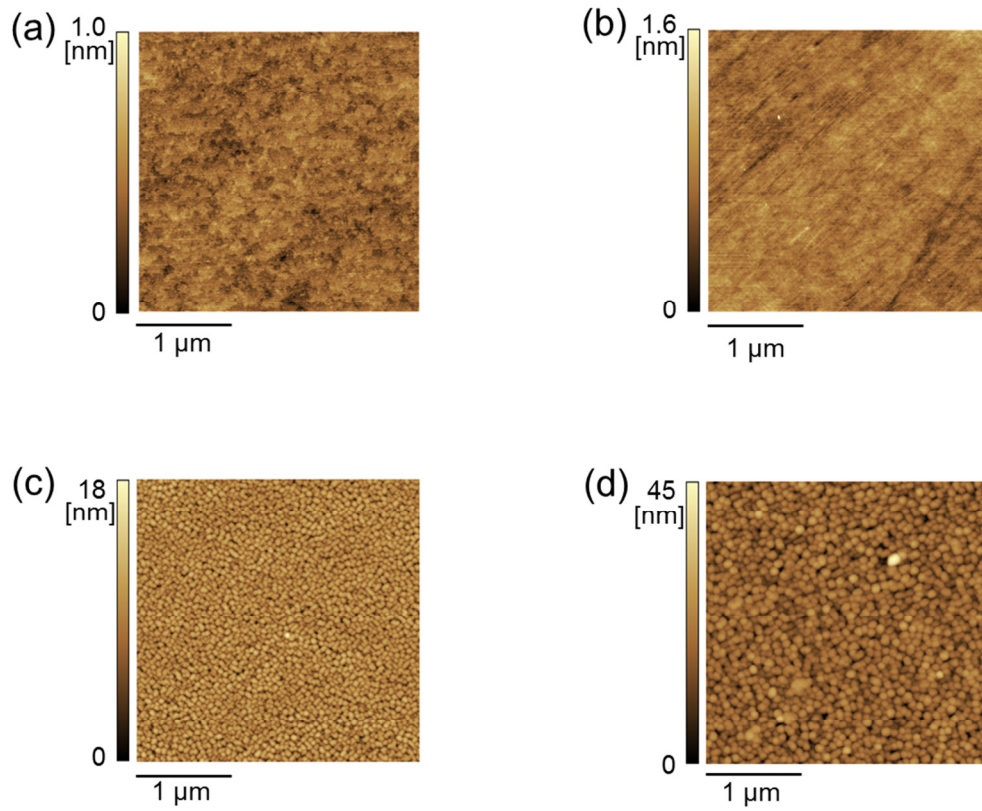


Figure 7 AFM images of the surface for the (a) YSZ substrate and (b) Sn-Nb-O thin film fabricated at 773 K, (c) at 873 K, and (d) at 973 K.

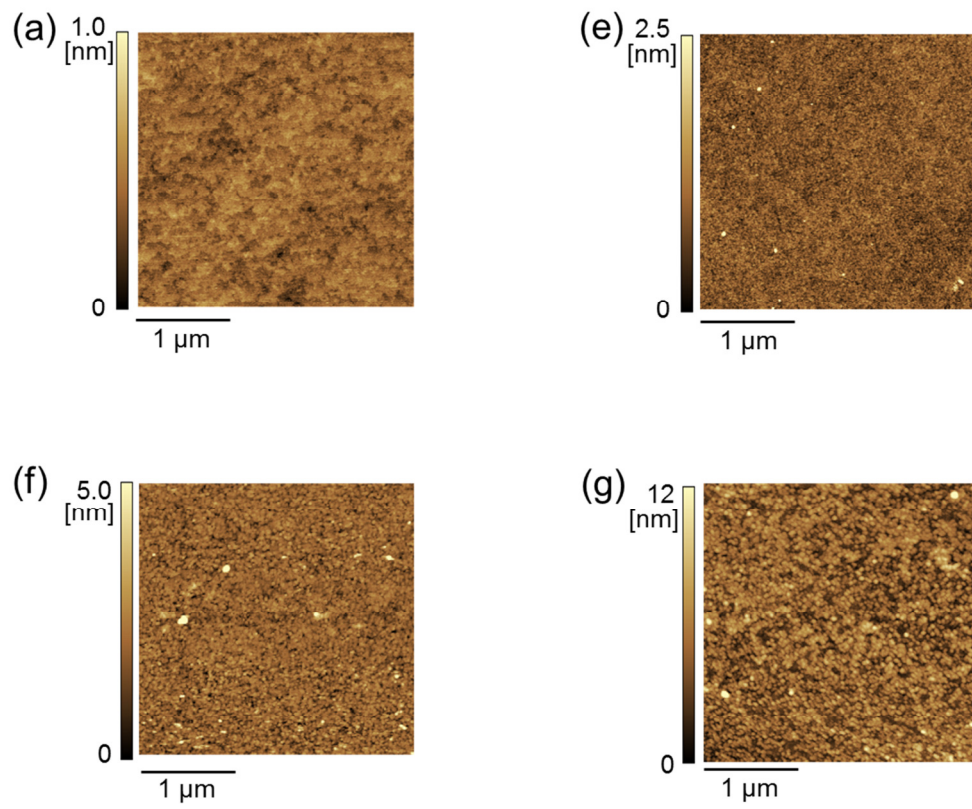


Figure 8 AFM images of the surface for the (a) YSZ substrate and (b) Sn-Ta-O thin film fabricated at 773 K, (c) at 873 K, and (d) at 973 K.

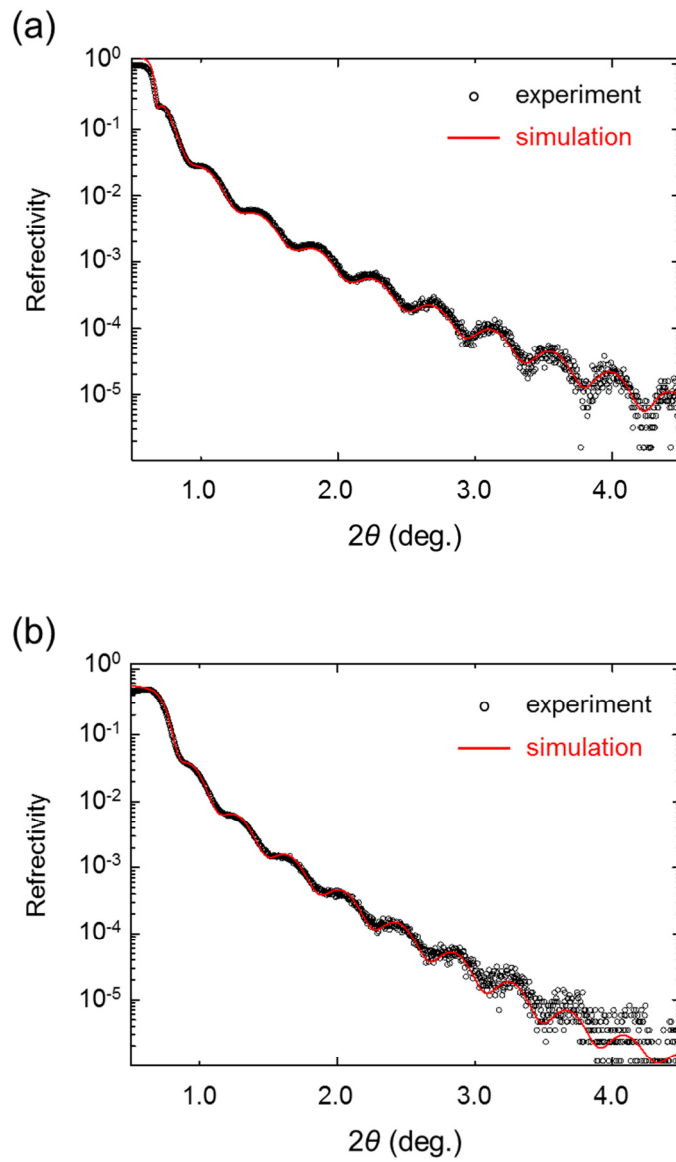


Figure 9 X-ray reflectivity of the Sn- $M$ -O ( $M$ =Nb or Ta) thin films fabricated at 773 K.

(a)  $M$ =Nb and (b)  $M$ =Ta.

## B. SnNb<sub>2</sub>O<sub>6</sub>

The optimized condition used for the growth of Sn-*M*-O pyrochlore is also suitable for SnNb<sub>2</sub>O<sub>6</sub>, i. e., the substrate temperature of 773 K and the oxygen pressure of  $1.0 \times 10^{-4}$  Torr. Figure 10 shows the XRD  $2\theta$ - $\theta$  profile of SnNb<sub>2</sub>O<sub>6</sub> thin film grown at this condition. All of the peaks are assigned to the diffractions from SnNb<sub>2</sub>O<sub>6</sub> (*h*00) and the Al<sub>2</sub>O<sub>3</sub> substrate. Figure 10 (b) is the magnification around the 600 peak of SnNb<sub>2</sub>O<sub>6</sub>. A clear fringe structure is found around the peak, which reflects the high orientation of the film and low dispersion of its out-of-plane lattice constant. The film thickness is estimated to be 20 nm from the oscillation cycles. The out-of-plane lattice constant is evaluated as 17.12 Å which is close to the reported bulk value of 17.093 Å[28]. Figure 11 (a) shows the  $\phi$ -scan on the 620 diffraction of the film and the 006 of the Al<sub>2</sub>O<sub>3</sub> substrate. The thin film is found to have been epitaxially grown on the substrate with the in-plane orientation relationships of SnNb<sub>2</sub>O<sub>6</sub> [010] // Al<sub>2</sub>O<sub>3</sub> [10 $\bar{1}$ 0] with existence of 180 degrees rotated domains. The rotated domains are attributed to the monoclinic crystal structure of SnNb<sub>2</sub>O<sub>6</sub>. A schematic top view is described in Fig. 11(b). This orientation relation is consistent with that predicted from the report on an epitaxial thin film of rutile-TiO<sub>2</sub>(101) / Al<sub>2</sub>O<sub>3</sub>(01 $\bar{1}$ 2). The in-plane lattice constants are evaluated from systematic XRD measurements as  $b=4.9$  Å and  $c=5.6$  Å which are close to the bulk values of  $b=4.877$  Å and  $c=5.558$  Å[28]. The strain of epitaxial growth is almost fully relaxed probably because of the relatively large lattice mismatches of 2.7% along *b* axis and 8.2% along *c* axis.

The cation atomic ratio of Sn/Nb obtained by SEM-WDX is 0.56, with the error of about  $\pm 10\%$ . They are close to those of SnNb<sub>2</sub>O<sub>6</sub> even with the use of a Sn<sub>2</sub>Nb<sub>2</sub>O<sub>7</sub> target. Considering the Sn/Nb of 0.9 for the Sn-Nb-O pyrochlore fabricated at

the same condition, the surplus ions for growth of  $\text{SnNb}_2\text{O}_6$  are considered to have evaporated from the growth front.

Figure 12 shows the X-ray reflectivity of the  $\text{SnNb}_2\text{O}_6$  and a simulated profile. The best fitting was obtained with the use of a film thickness of 20.5 nm, a density of  $5.8 \text{ g/cm}^3$ , and a RMS surface roughness of 1.0 nm. The thickness is consistent with the value estimated from XRD and the density is coincident with the theoretical one of  $5.74 \text{ g/cm}^3$ . These results indicate the homogeneousness and high crystallinity of the  $\text{SnNb}_2\text{O}_6$  film. An AFM image of the film surface is represented in Fig. 13. The granular surface morphology may be attributed to the island mode crystal growth and the intercepted grain growth caused by coexistence of two domains. The RMS surface roughness is evaluated to be 0.9 nm from the AFM.

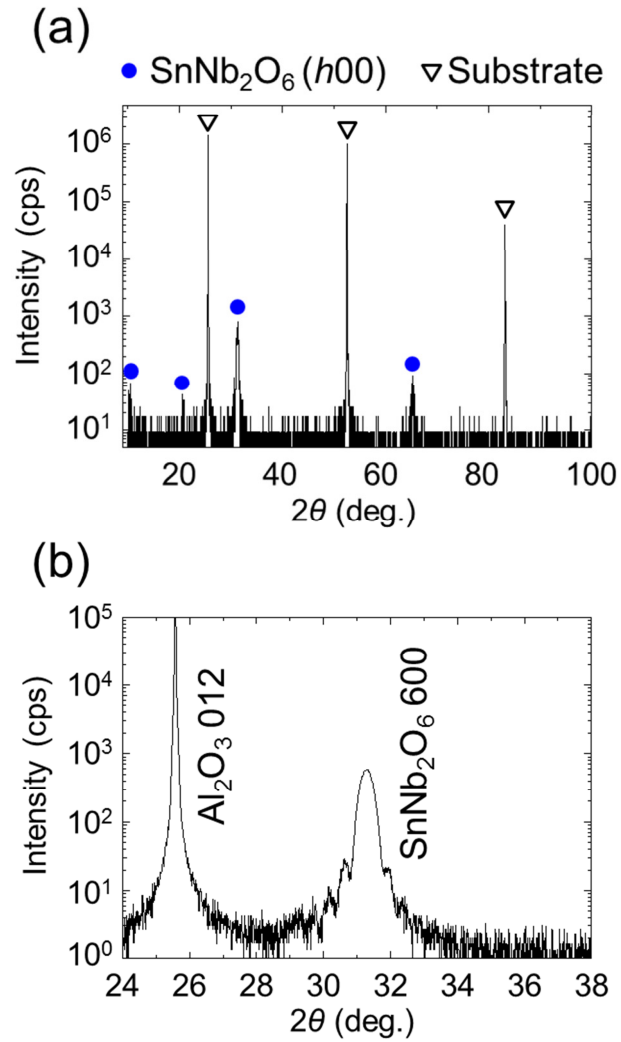


Figure 10 XRD  $2\theta$ - $\theta$  profiles of the  $\text{SnNb}_2\text{O}_6$  thin film fabricated on the  $\text{Al}_2\text{O}_3(01\bar{1}2)$  substrate. (a) profile in the range of 10 to 100 degrees and (b) magnification around the 600 diffraction of  $\text{SnNb}_2\text{O}_6$ .

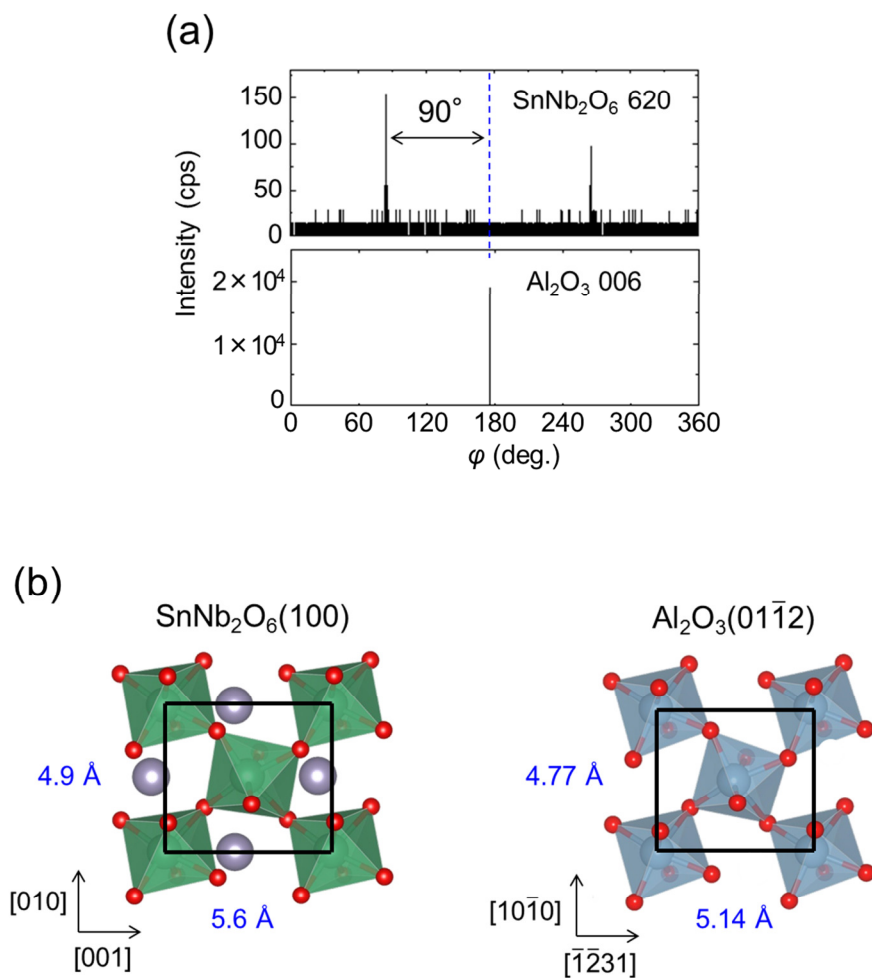


Figure 11 In-plane orientation relationships of the  $\text{SnNb}_2\text{O}_6$  thin film and the  $\text{Al}_2\text{O}_3$  substrate. (a) XRD  $\phi$  profiles of 620 diffractions of the  $\text{SnNb}_2\text{O}_6$  thin film and 006 diffraction of  $\text{Al}_2\text{O}_3$  substrate. (b) projected view of  $\text{SnNb}_2\text{O}_6$  (100) and  $\text{Al}_2\text{O}_3$  ( $01\bar{1}2$ ).

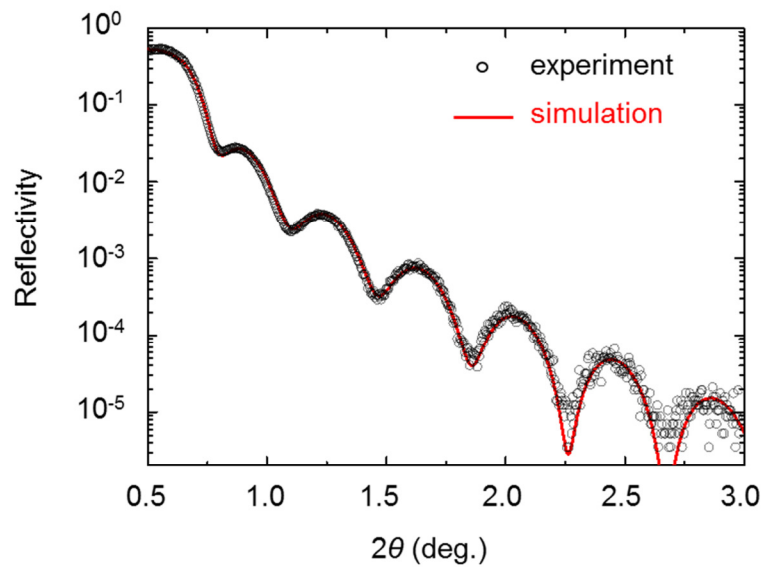


Figure 12 X-ray reflectivity of the  $\text{SnNb}_2\text{O}_6$  thin film. The red line shows a simulated profile with the parameter of film thickness of 20.5 nm, a density of  $5.8 \text{ g/cm}^3$ , and a RMS surface roughness of 1.0 nm.

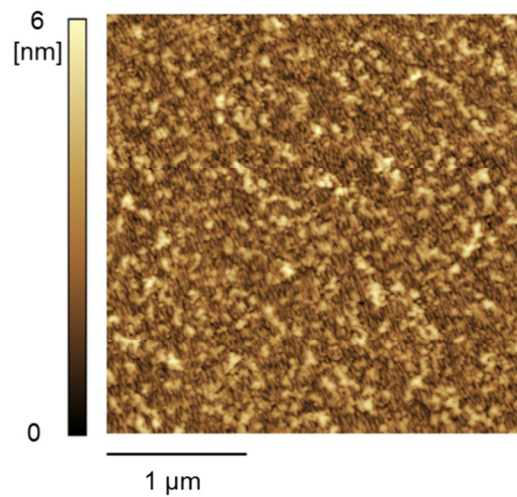


Figure 13 AFM image of the surface for the  $\text{SnNb}_2\text{O}_6$  thin film. Its RMS surface roughness is estimated to be 0.9 nm.

### C. SnWO<sub>4</sub>

The XRD  $2\theta$ - $\theta$  profiles of Sn-W-O thin films fabricated with oxygen partial pressure of 5, 7, 10 mTorr are presented in Fig. 14. For this system, higher oxygen partial pressure was required than that suitable for the three compounds described above. The film fabricated at 7 mTorr is found to be a single phase of (010)-oriented  $\alpha$ -SnWO<sub>4</sub>. Growth condition with low pressure involves the precipitation of WO<sub>2</sub>, a reduced phase with W<sup>4+</sup>. On the other hand, the film fabricated at higher oxidizing condition shows the peaks of not SnWO<sub>4</sub> but other phase(s). They could not be identified but might have emerged due to the oxidation of Sn(II) to Sn(IV). The peaks of  $\alpha$ -SnWO<sub>4</sub> do not have a fringe structure in contrast to the other films presented above. The rocking curve of the 040 peak of the 7 mTorr film is shown in Fig. 15. The FWHM of 1.5 degrees shows its low orientation. The estimated out-of-plane lattice constant of 11.79 Å is slightly larger than a reported bulk value of 11.65 Å[15]. Figure 16 (a) represents the  $\phi$ -scan on the 042 diffraction of the film and the 006 of Al<sub>2</sub>O<sub>3</sub> substrate. The  $\alpha$ -SnWO<sub>4</sub> film is found to have epitaxially grown on the substrate with the in-plane orientation relationship of  $\alpha$ -SnWO<sub>4</sub> [001] // Al<sub>2</sub>O<sub>3</sub> [10 $\bar{1}$ 0]. A schematic top view is drawn in Fig. 16 (b). The in-plane lattice constants are estimated to be  $a=5.6$  Å and  $c=5.0$  Å. These values are close to the bulk values of  $a=5.627$  Å and  $c=4.997$  Å[15]. Therefore, the strain of epitaxial growth is considered to be almost fully relaxed as well as the SnNb<sub>2</sub>O<sub>6</sub> film. The in-plane mismatches with the substrate are 8.9% along  $a$  axis and 5.0% along  $c$  axis, respectively. The Sn/W ratio of  $1.03 \pm 0.05$  was obtained for the 7 mTorr film from the SEM-WDX measurement.

The surface morphologies of the  $\alpha$ -SnWO<sub>4</sub> films with the average thickness of about 10 nm and 25 nm are represented in Fig. 17. The 25 nm film is fabricated using

higher laser energy of  $3.0 \text{ J/cm}^2$  with respect to  $1.5 \text{ J/cm}^2$  and the same condition for the other parameters. The films exhibit characteristic anisotropic surface morphology which suggests that the films have grown selectively along [001]. This is assumed to be concerned with the difference in the mismatches of two in-plane directions. The 10 nm sample shows exposure of the substrate surface due to the selective growth. This exposure almost disappears in the thicker film. However, the 25 nm film is found to contain a precipitation of  $\text{WO}_2$  by an XRD analysis. Therefore, I use the thinner film for property characterization even though it has the inhomogeneous morphology.

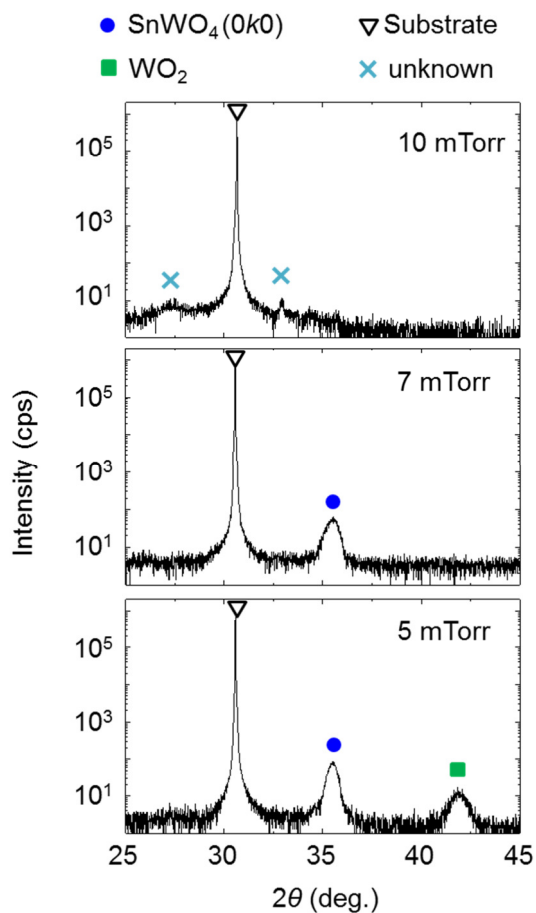


Figure 14 XRD  $2\theta$ - $\theta$  profiles of the  $\alpha$ - $\text{SnWO}_4$  thin film fabricated on the  $\text{Al}_2\text{O}_3$  (01 $\bar{1}$ 2) substrate at different oxygen partial pressure.

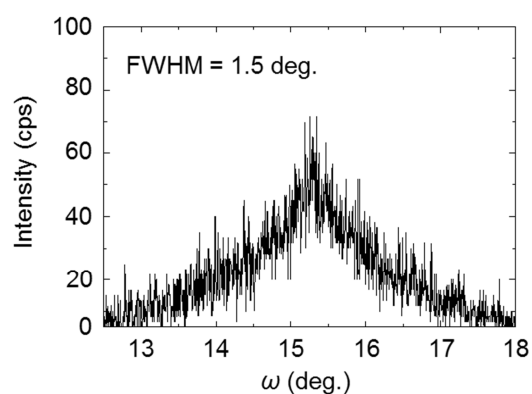


Figure 15 Rocking curve on the  $\alpha$ - $\text{SnWO}_4$  (040) for the thin film fabricated at 7 mTorr of oxygen partial pressure. The FWHM is 1.5 degrees.

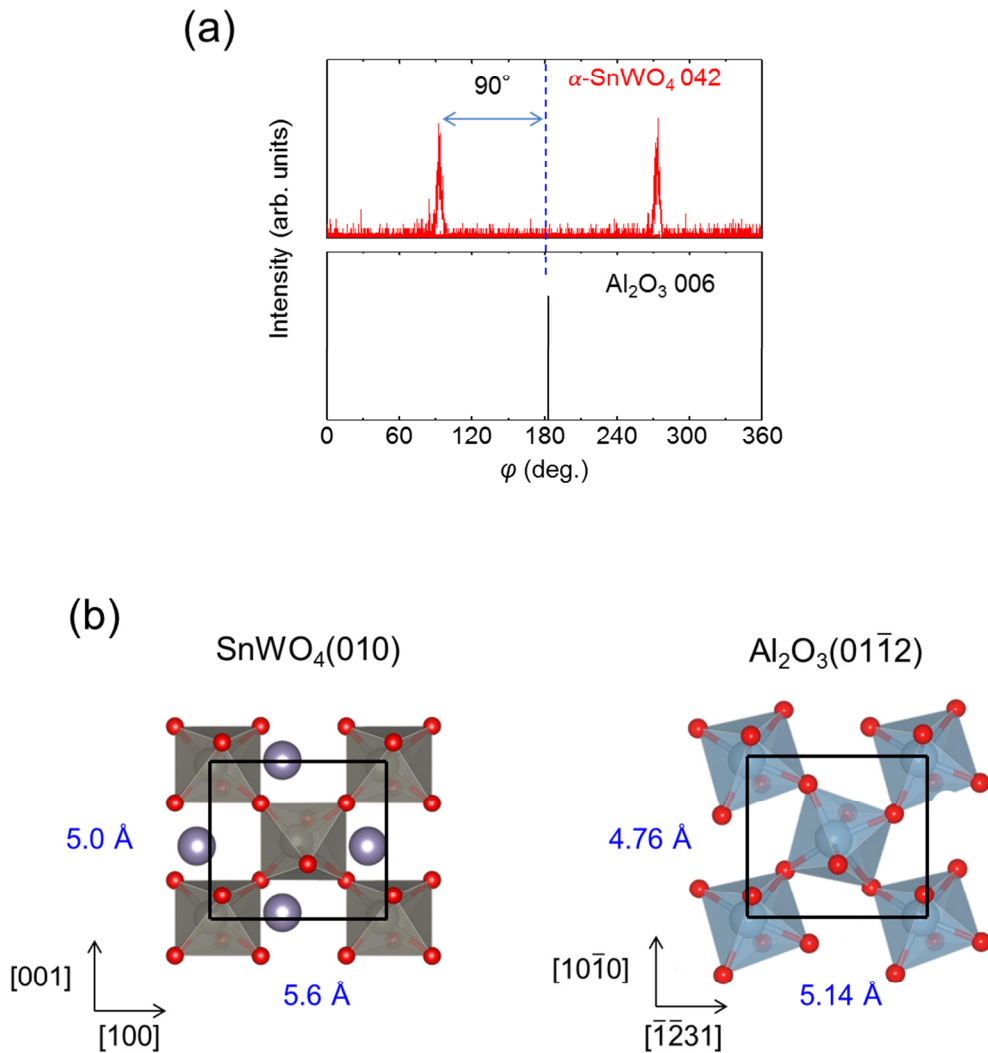


Figure 16 In-plane orientation relationships of the  $\alpha\text{-SnWO}_4$  thin film and the  $\text{Al}_2\text{O}_3$  substrate. (a) XRD  $\phi$  profiles of 042 diffractions of the  $\alpha\text{-SnWO}_4$  and 006 diffraction of  $\text{Al}_2\text{O}_3$ . (b) projected view of  $\alpha\text{-SnWO}_4$  (100) and  $\text{Al}_2\text{O}_3$  ( $01\bar{1}2$ ).

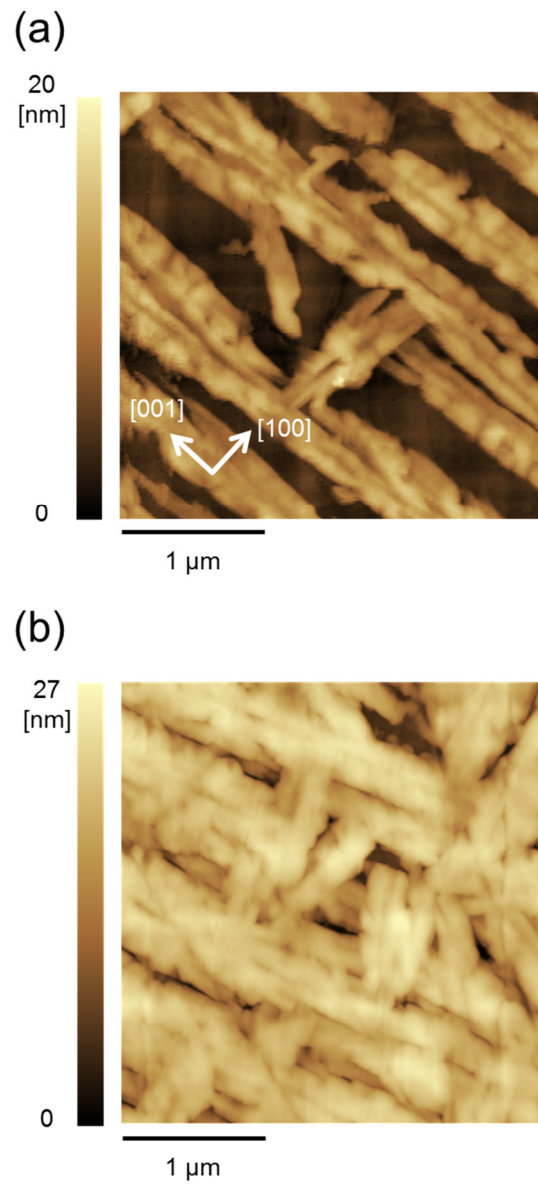


Figure 17 AFM images of the surface for the  $\alpha\text{-SnWO}_4$  thin films with the average thickness of (a) 10 nm and (b) 25 nm. The vectors represent the orientation of  $\alpha\text{-SnWO}_4$ .

#### 4. Optical and electrical properties of Sn(II) ternary oxides

In this section, the optical and electrical properties of the thin films are characterized. Figure 18 represents the XPS spectra near the Fermi levels for the thin films; Sn-*M*-O pyrochlores fabricated at 773 K, SnNb<sub>2</sub>O<sub>6</sub>, and  $\alpha$ -SnWO<sub>4</sub> at 7 mTorr with the reference of an SnO thin film. The intensity scales are aligned at the maximum intensities in the shown range. The spectra of the complex oxides have similar features: There are small peaks spreading in the range from their VBM to 2.5 eV and larger peaks located next to them. Meanwhile, their valence band structures are discussed in chapter 2. Here, Figure 19 shows again the XPS spectrum of SnNb<sub>2</sub>O<sub>6</sub> and the density of states (DOS) near its VBM obtained by the DFT calculation using the HSE06 functional: The conditions for the calculation are described in chapter 2. The intensity scale and origin of the energy for the calculated DOS are standardized at the small peak at the VBM. It is found that the relative peak positions of the XPS spectrum are consistent with the calculated DOS. The small peak of the XPS spectrum is thought to reflect the hybridized states of Sn-5*sp* and O-2*p* comparing to the calculated projected DOS. The VBM energies of the films are decided as the thresholds of the small peaks. For the SnO film with *p*-type conductivity, the Fermi level is coincident with the VBM, which is consistent with the previous report that has shown the shallow acceptor level of SnO located about 90 meV above the VBM[3]. The Fermi levels relative to the VBM are estimated to be 1.3 eV for SnNb<sub>2</sub>O<sub>6</sub> and 1.1 eV for the other three films, respectively. Investigation on the valence of Sn using Sn-3*d* spectra was difficult because the binding energies for those of Sn(II) and Sn(IV) were too close to each other to divide the peaks appropriately.

Figure 20 (a) shows the transmittance spectra of the Sn-Nb-O pyrochlore thin

films fabricated at 773, 873, and 973 K. A characteristic decrease in the transmittance is observed at about 500 nm for the film deposited at 773 K and at shorter wavelength for the higher-temperature-grown samples. The shift of the absorption thresholds is probably due to the difference in the concentration and/or valence states of Sn. Figure 20 (b) shows the spectra of Sn-Ta-O thin films. The spectra of 773 K and 873 K have similar threshold. They exhibit small difference in Sn/Ta ratios as mentioned above.

The transmittance and reflectance spectra of  $\text{SnNb}_2\text{O}_6$  are presented in Fig. 21 (a). A decrease in the transmittance spectrum is located at about 500 nm. The reflectance spectra were measured for two arrangements; light incident from the thin film side and the substrate side. The difference in the two reflectance spectra found at shorter wavelength is ascribed to the absorption of the film. An absorption spectrum of  $\text{SnNb}_2\text{O}_6$  is calculated using the transmittance and reflectance spectra, those of the  $\text{Al}_2\text{O}_3$  substrate described in Fig. 21 (b), and the film thickness obtained from the X-ray reflectivity analysis. The resultant is shown in Fig. 21 (c) with a spectrum obtained from DFT calculation using the HSE06 functional. The absorption threshold of the film is coincident with that of the calculated spectrum at about 2.55 eV. The experimental absorption coefficient reaches  $10^5 \text{ cm}^{-1}$  at 3.3 eV. The difference in the slope above 4 eV may reflect the DOS of the valence band (Fig. 19). The absorption spectra for the Sn-M-O film fabricated at 773 K and the  $\alpha\text{-SnWO}_4$  film at 7 mTorr are obtained in the same way as that for  $\text{SnNb}_2\text{O}_6$ . The results are summarized in Fig. 22. The absorption thresholds are presented with the reported values in table 1. The reported values were obtained from diffuse reflectance spectroscopy and the Kubelka-Munk theory. The absorption thresholds of the films are similar to those reported.

Among the fabricated thin films, only the  $\alpha$ -SnWO<sub>4</sub> exhibits electrical conductivity. The resistivity is measured as  $9.2 \times 10^4 \Omega\text{cm}$ , which is in the same order to that of a sintered pellet fabricated by a solid state reaction,  $4.0 \times 10^4 \Omega\text{cm}$ . Hall measurements on the thin film could not yield satisfying data with low noise enough to distinguish the carrier type, probably because of its inhomogeneous morphology. In this point, it is possible that the resistivity obtained by the van der Pauw method also contains some inaccuracy. The other compounds never exhibit conductivity even when dopants are added to them; 1 cation% of Cu, Zr, and Ge for SnNb<sub>2</sub>O<sub>6</sub> and Sn-*M*-O pyrochlores.

The high resistivities of the films are consistent with the results of XPS. The energy difference between their Fermi levels and both VBM and CBM are summarized in table 2 and Fig. 23. The depths from the CBM are evaluated under the assumption that their optical absorption thresholds correspond to the band gaps. These compounds are found to have indirect-type band structure as shown in chapter 2. Although it is not clear whether the weak absorption of the indirect-transition could be observed for the thin films, the differences between indirect- and direct-gaps are less than 0.2 eV according to the calculation results. It is found that the Fermi levels of the films are located at deep positions from both of the band edges, which indicates the low carrier concentrations of them. This result and high resistivities of doped samples indicate the possibility that both of the acceptor- and donor-like defects are ease to form and act as Fermi level pinning for these compounds.

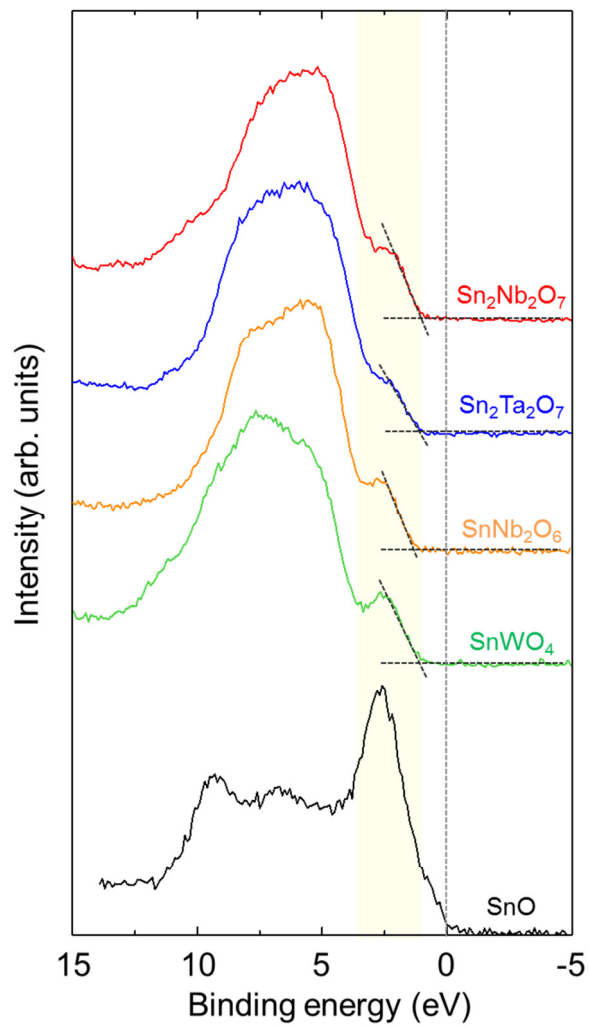


Figure 18 XPS spectra of the Sn(II) oxide thin films. The origin of the energy is set at Fermi level.

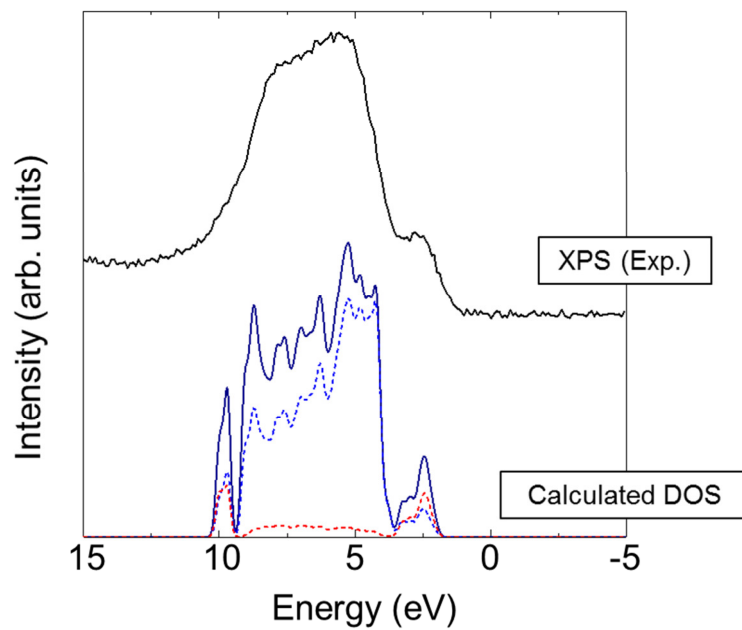


Figure 19 Comparison between the XPS spectrum and calculated valence band DOS for  $\text{SnNb}_2\text{O}_6$ .

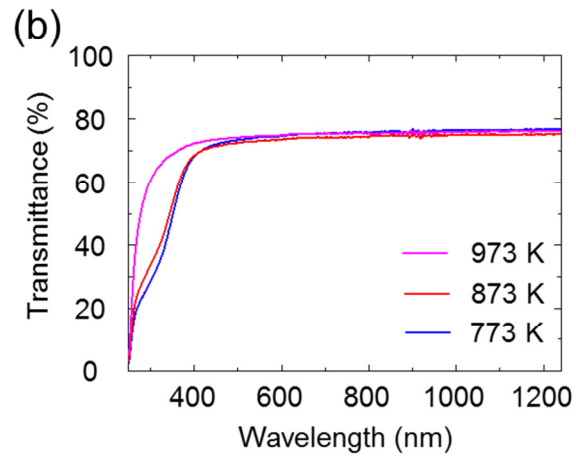
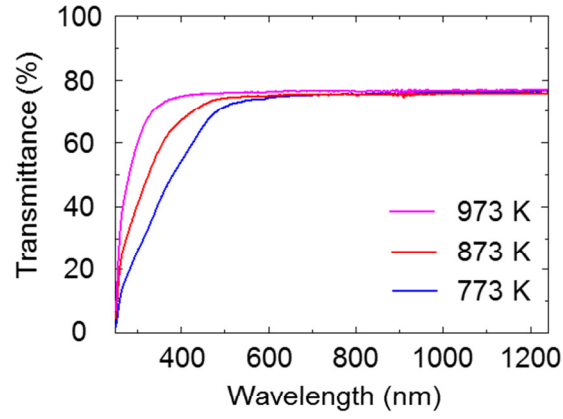


Figure 20 Transmittance spectra of Sn- $M$ -O ( $M$ =Nb or Ta) thin films fabricated at substrate temperature of 773, 873, and 973 K. (a)  $M$ =Nb and (b)  $M$ =Ta.

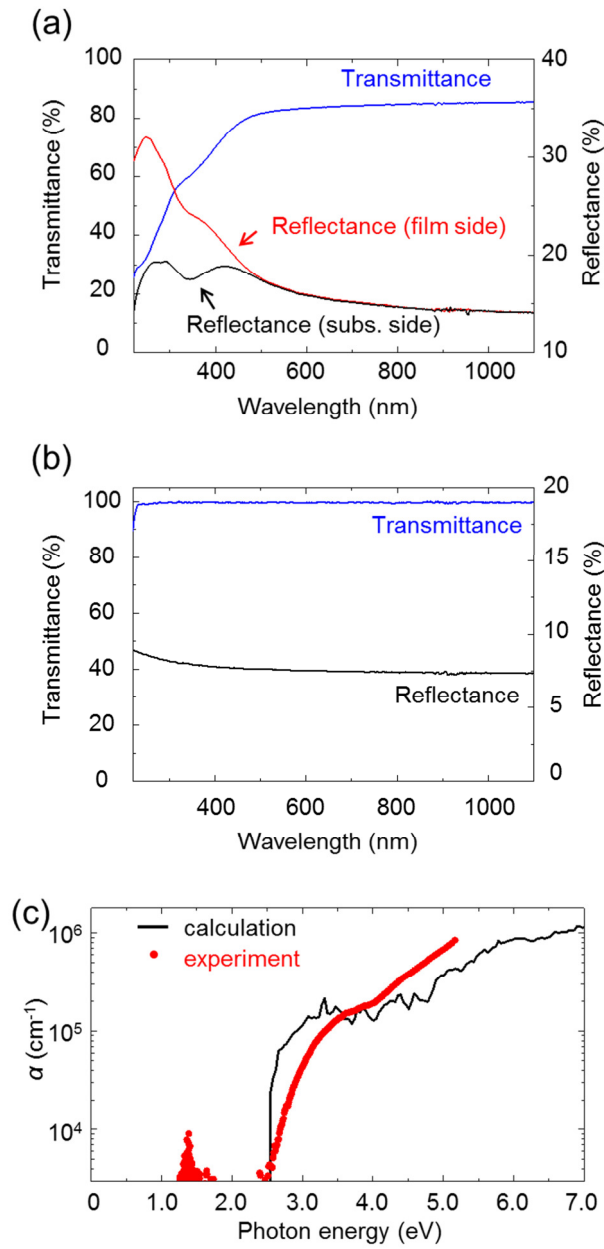


Figure 21 Optical properties of the SnNb<sub>2</sub>O<sub>6</sub> thin film and Al<sub>2</sub>O<sub>3</sub> substrate. (a) transmittance and reflectance spectra for the SnNb<sub>2</sub>O<sub>6</sub> thin film with the Al<sub>2</sub>O<sub>3</sub> substrate. Reflectance is measured with light incident from thin film side and the substrate side. (b) Transmittance and reflectance spectrum for the Al<sub>2</sub>O<sub>3</sub> substrate. (c) Absorption spectrum of the SnNb<sub>2</sub>O<sub>6</sub> thin film excluding the absorption or reflection of substrate. The spectrum obtained from first-principles calculation is also presented.

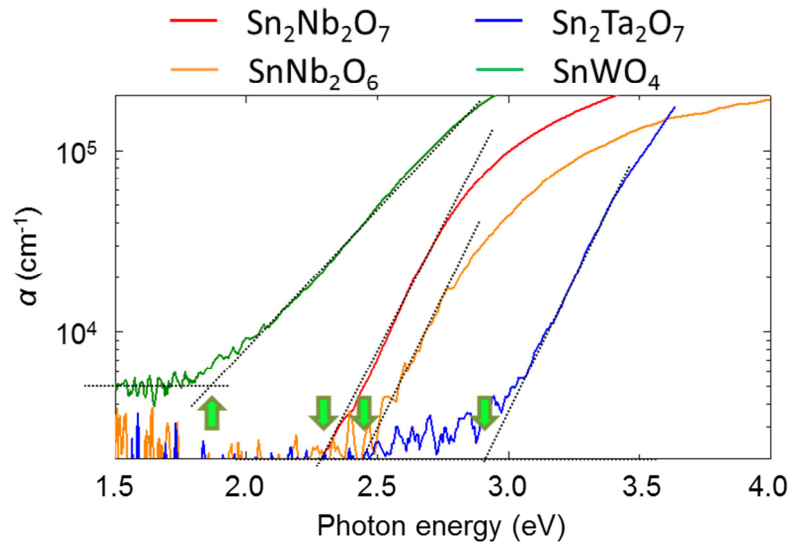


Figure 22 Absorption spectra of Sn(II) oxide thin films. The vectors represent their absorption thresholds.

Table 1 Comparison among the absorption thresholds and reported values obtained by diffuse reflection for powder samples.

	absorption Threshold (eV)	Reported (eV)
$\text{Sn}_2\text{Nb}_2\text{O}_7$	2.3	2.3 [8]
$\text{Sn}_2\text{Ta}_2\text{O}_7$	2.9	3.0 [8]
$\text{SnNb}_2\text{O}_6$	2.5	2.3, 2.6 [8, 29]
$\alpha\text{-SnWO}_4$	1.8	1.64, 1.9 [9, 30]

Table 2 Summary of the Fermi level position. The energies between the VBM to Fermi levels are measured by XPS and Fermi levels to the CBM are estimated assuming the absorption thresholds as their band gaps.

	Fermi level to VBM (eV)	Fermi level to CBM (eV)	absorption threshold (eV)
$\text{Sn}_2\text{Nb}_2\text{O}_7$	1.1	1.2	2.3
$\text{Sn}_2\text{Ta}_2\text{O}_7$	1.1	1.8	2.9
$\text{SnNb}_2\text{O}_6$	1.3	1.2	2.5
$\alpha\text{-SnWO}_4$	1.1	0.7	1.8

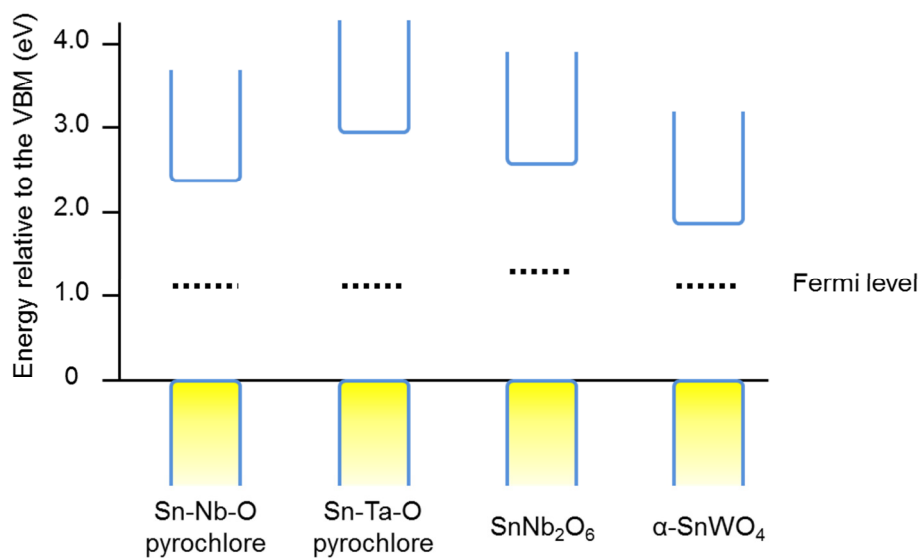


Figure 23 Schematic of the Fermi level positions in band gaps for Sn(II) oxide thin films. The VBM positions are aligned as a matter of convenience.

## 5. Conclusion

The optical and electrical properties of Sn(II) complex oxides were investigated using epitaxial thin films. The epitaxial thin films of Sn-*M*-O (*M*=Nb, Ta) pyrochlore, SnNb<sub>2</sub>O<sub>6</sub>, and α-SnWO<sub>4</sub> were fabricated on single crystal substrates by the PLD method. The optical absorption coefficients and absorption thresholds of them were evaluated from spectroscopy. Electrical conductivity is observed for only the α-SnWO<sub>4</sub> film whose resistivity is  $9.2 \times 10^4 \Omega\text{cm}$ . The other films are insulator even if dopants are added to them. The XPS analyses showed that the Fermi levels of the films are located at deep positions from both of the band edges. This result is in line with the high resistivity of the films and indicates the presence of Fermi level pinning caused by defects.

## Reference

- [1] M.W. Stoltzfus, P.M. Woodward, R. Seshadri, J.H. Klepeis and B. Bursten, *Inorg. Chem.* 46 (2007) 3839.
- [2] Y. Hosogi, Y. Shimodaira, H. Kato, H. Kobayashi and A. Kudo, *Chem. Mater.* 20 (2008) 1299.
- [3] Y. Ogo, H. Hiramatsu, K. Nomura, H. Yanagi, T. Kamiya, M. Kimura, M. Hirano and H. Hosono, *Phys. Status Solidi A* 206 (2009) 2187.
- [4] G. Hautier, A. Miglio, G. Ceder, G.M. Rignanese and X. Gonze, *Nat Commun* 4 (2013) 2292.
- [5] R. Asahi, T. Morikawa, T. Ohwaki, K. Aoki and Y. Taga, *Science* 293 (2001) 269.
- [6] H. Kominami, K. Oki, M. Kohno, S. Onoue, Y. Kera and B. Ohtani, *J. Mater. Chem.* 11 (2001) 604.
- [7] Y. Noda, B. Lee, K. Domen and J.N. Kondo, *Chem. Mater.* 20 (2008) 5361.
- [8] Y. Hosogi, K. Tanabe, H. Kato, H. Kobayashi and A. Kudo, *Chem. Lett.* 33 (2004) 28.
- [9] I.S. Cho, C.H. Kwak, D.W. Kim, S. Lee and K.S. Hong, *J. Phys. Chem. C* 113 (2009) 10647.
- [10] Y. Ogo, H. Hiramatsu, K. Nomura, H. Yanagi, T. Kamiya, M. Hirano and H. Hosono, *Appl. Phys. Lett.* 93 (2008).
- [11] W. Guo, L. Fu, Y. Zhang, K. Zhang, L.Y. Liang, Z.M. Liu, H.T. Cao and X.Q. Pan, *Appl. Phys. Lett.* 96 (2010).
- [12] H. Raebiger, S. Lany and A. Zunger, *Phys. Rev. B* 76 (2007).
- [13] H. Ohta, K. Kawamura, M. Orita, M. Hirano, N. Sarukura and H. Hosono, *Appl. Phys. Lett.* 77 (2000) 475.
- [14] H. Yanagi, K. Ueda, H. Ohta, M. Orita, M. Hirano and H. Hosono, *Solid State Commun.* 121 (2002) 15.

- [15] Jeitschk.W and A.W. Sleight, *Acta Crystallogr. B* 30 (1974) 2088.
- [16] T. Birchall and A.W. Sleight, *J. Solid State Chem.* 13 (1975) 118.
- [17] L.P. Cruz, J.M. Savariault, J. Rocha, J.C. Jumas and J.D.P. de Jesus, *J. Solid State Chem.* 156 (2001) 349.
- [18] J.L. Solis and V. Lantto, *Phys. Scripta* T69 (1997) 281.
- [19] A. Walsh, D.J. Payne, R.G. Egdeell and G.W. Watson, *Chem. Soc. Rev.* 40 (2011) 4455.
- [20] A. Walsh, G.W. Watson, D.J. Payne, R.G. Edgell, J.H. Guo, P.A. Glans, T. Learmonth and K.E. Smith, *Phys. Rev. B* 73 (2006).
- [21] A. Kyono, M. Kimata, M. Matsuhisa, Y. Miyashita and K. Okamoto, *Phys. Chem. Miner.* 29 (2002) 254.
- [22] M. Gasperin, *Cr. Hebd. Acad. Sci.* 240 (1955) 2340.
- [23] M. Murakami, Y. Matsumoto, T. Hasegawa, P. Ahmet, K. Nakajima, T. Chikyow, H. Ofuchi, I. Nakai and H. Koinuma, *J. Appl. Phys.* 95 (2004) 5330.
- [24] J.E. Dominguez, X.Q. Pan, L. Fu, P.A. Van Rompay, Z. Zhang, J.A. Nees and P.P. Pronko, *J. Appl. Phys.* 91 (2002) 1060.
- [25] B. Darriet, M. Rat, J. Galy and Hagenmul.P, *Mater. Res. Bull.* 6 (1971) 1305.
- [26] R. Galati, R.W. Hughes, C.S. Knee, P.F. Henry and M.T. Weller, *J. Mater. Chem.* 17 (2007) 160.
- [27] L.G. Parratt, *Phys. Rev.* 95 (1954) 359.
- [28] T.S. Ercit and P. Cerny, *Can. Mineral* 26 (1988) 899.
- [29] S.J. Liang, S.Y. Zhu, Y. Chen, W.M. Wu, X.C. Wang and L. Wu, *J. Mater. Chem.* 22 (2012) 2670.
- [30] Y.G. Su, L.C. Hou, C.F. Du, L.M. Peng, K. Guan and X.J. Wang, *Rsc Adv.* 2 (2012) 6266.

## **Appendix: Fabrication and characterization of an Sn-Ti-O thin film**

### 1. Outline

We tried to fabricate an  $\text{Sn}_2\text{TiO}_4$  thin film by the PLD method. Although the objective compound had never been grown, another phase of an Sn-Ti-O was obtained. Its structure, composition, surface morphology, and transmittance spectrum are shown below.

### 2. Experiments

Sn-Ti-O thin films were fabricated on the  $\text{MgAl}_2\text{O}_4$  (100) substrates using the dual targets of Sn and  $\text{TiO}_2$ . The ablation ratio of Sn :  $\text{TiO}_2$  was 3 : 1. The substrate temperature of 773 K and the oxygen partial pressure of 1 mTorr were used. The laser energy density of  $4.0 \text{ J/cm}^2$ , the spot size of  $2.0 \text{ mm}^2$ , and the pulse frequency of 5 Hz were used. After the deposition, gas flow was stopped and the samples were cooled to room temperature in the chamber.

The crystal structures and orientations of the thin films were investigated by a transmission electron microscope (TEM) in addition to XRD. The composition of the film was obtained by an energy-dispersive X-ray spectrum (EDX) analyzer on the TEM. Other investigation was performed in the same way as mentioned above.

### 3. Results

The X-ray reflectivity of the thin film is exhibited in Fig. 1. The parameters used in the simulation are a thickness of 48 nm, a density of  $5.12 \text{ g/cm}^3$ , and a RMS surface roughness of 0.6 nm. This good fitting with a single layer model suggests the homogeneousness of the thin film.

Figure 2 (a) shows the XRD  $2\theta$ - $\theta$  profile of the Sn-Ti-O thin film on the  $\text{MgAl}_2\text{O}_4$  substrate. A peak of the thin film is observed at 43.92 degrees though it is not assigned to any diffractions of  $\text{Sn}_2\text{TiO}_4$ . Although the ablation ratio of Sn and  $\text{TiO}_2$  targets was varied in the range from Sn :  $\text{TiO}_2 = 6 : 1$  to  $2 : 3$ , other phases including Sn,  $\text{TiO}_2$ , and  $\text{Sn}_2\text{TiO}_4$  was not grown and the ratio of  $3 : 1$  yielded the sharpest peak among them. A FWHM of the rocking curve at the peak is estimated to be 0.10 degrees, which reflects the high orientation of the thin film. Figure 2 (b) shows the reciprocal space mapping around the 622 diffraction of the  $\text{MgAl}_2\text{O}_4$ . A peak of the thin film is observed at the in-plane coordinate coincident with that of the 622 diffraction of the substrate. This indicates that the film has been epitaxially grown on the substrate.

In Fig. 3 (a), a cross-sectional TEM bright-field image is presented. The viewing direction is  $[100]$  of the  $\text{MgAl}_2\text{O}_4$  substrate. Near the interface, oriented region which looks dark contrast is observed. Considering the result of the X-ray reflectivity measurement, the other amorphous or polycrystalline region is assumed to be caused by damage in the sample preparation for TEM observation. Fig. 3 (b) shows the micro diffraction pattern obtained from the orientated region and the substrate. Although the crystal structure of the thin film could not be distinguished, one of the most plausible candidates is a rocksalt structure considering the diffraction pattern and the periodicity. Assuming the rocksalt structure, the lattice parameters are estimated to be  $4.02 \text{ \AA}$  for the

in-plane direction and 4.12 Å for the out-of-plane direction from XRD while titanium monoxide (TiO) is reported to have a rocksalt structure with the lattice parameter of 4.18 Å[1]. The composition of the oriented region is measured by STEM-EDX. The Sn/Ti ratio is obtained as 0.47, close to 0.5.

Figure 4 shows the transmittance spectrum of the Sn-Ti-O thin film. The slope changes at about 580 nm and 350 nm which correspond to 2.1 eV and 3.4 eV, respectively. TiO is known to exhibit metallic character. The band gaps of Sn<sub>2</sub>TiO<sub>4</sub>, rutile-TiO<sub>2</sub>, SnO<sub>2</sub>, and SnO are 1.73 eV (calculated in Chapter 2), 3.0, 4.0, and 0.7 eV, respectively[2-4].

It is considered of value to investigate the detailed crystal structure and valence of Sn in the cubic phase.

## References

- [1] E.S. Bumps, H.D. Kessler and M. Hansen, T. Am. Soc. Metals 45 (1953) 1008.
- [2] O. Diwald, T.L. Thompson, T. Zubkov, E.G. Goralski, S.D. Walck and J.T. Yates, J Phys Chem B 108 (2004) 6004.
- [3] H. Kim, R.C.Y. Auyeung and A. Pique, Thin Solid Films 516 (2008) 5052.
- [4] Y. Ogo, H. Hiramatsu, K. Nomura, H. Yanagi, T. Kamiya, M. Kimura, M. Hirano and H. Hosono, Phys. Status Solidi A 206 (2009) 2187.

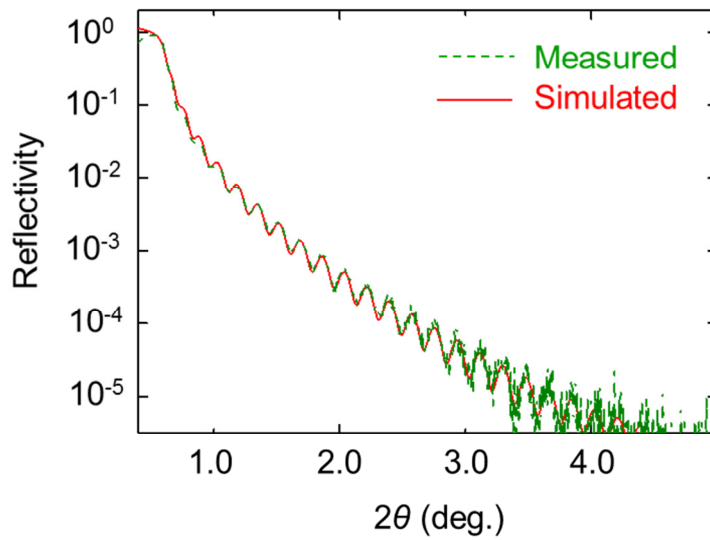


Figure 1 X-ray reflectivity of the thin film and simulated one. The parameters used in the simulation are a thickness of 48 nm, a density of  $5.12 \text{ g/cm}^3$ , and a RMS surface roughness of 0.6 nm.

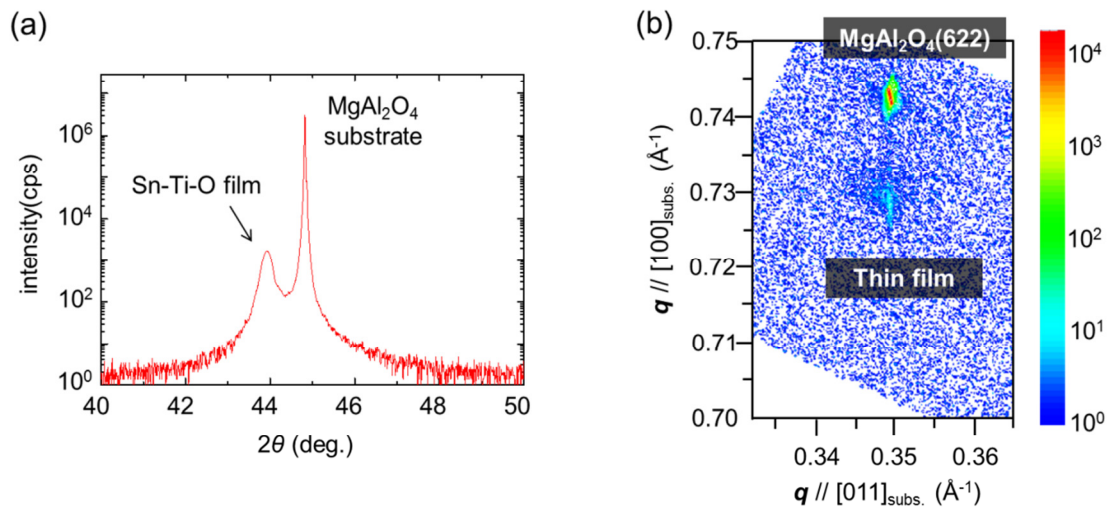


Figure 2 XRD profiles of the Sn-Ti-O thin film. (a)  $2\theta$ - $\theta$  profile and (b) reciprocal space mapping around the 622 diffraction of the  $\text{MgAl}_2\text{O}_4$ .

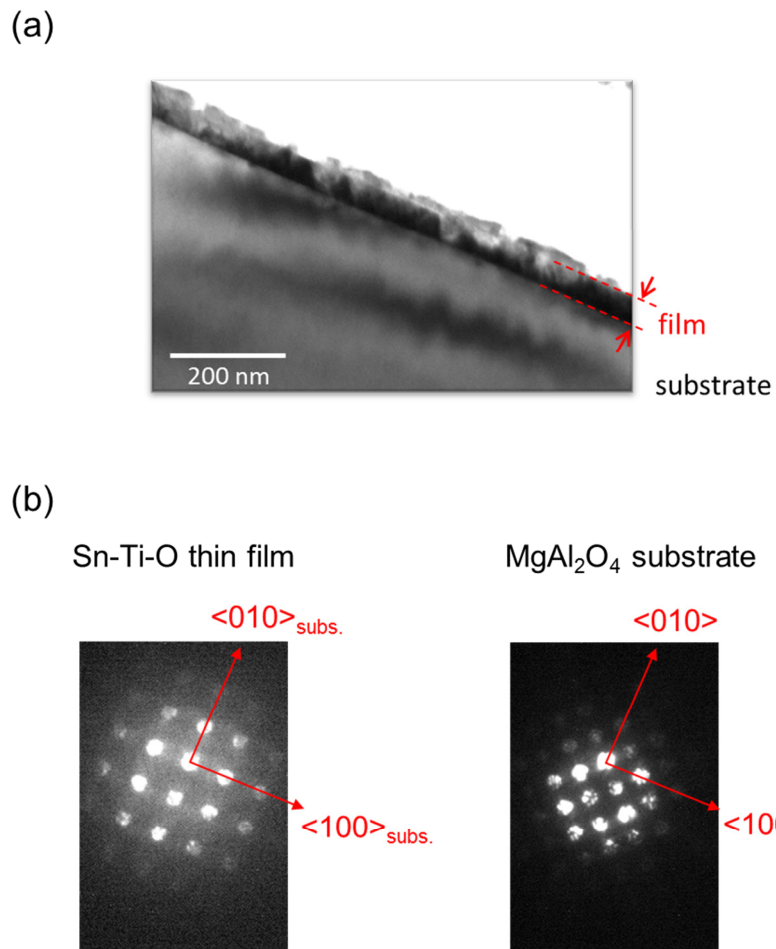


Figure 3 TEM images of the Sn-Ti-O thin film. (a) a cross-sectional bright-field image and (b) micro diffraction patterns of the orientated region (left) and the substrate (right).

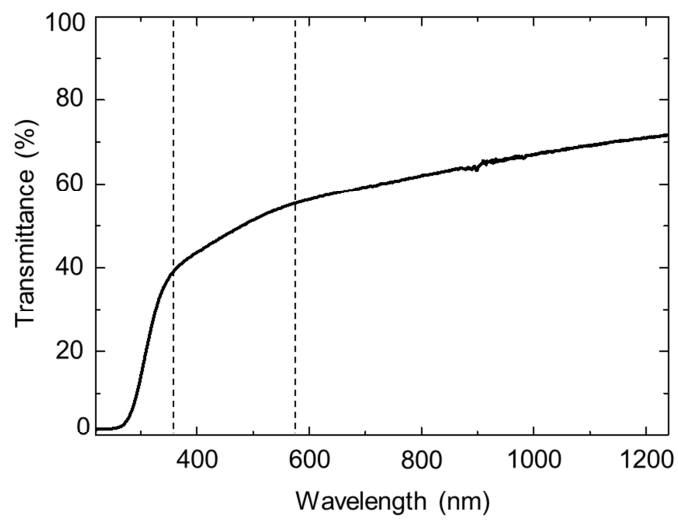


Figure 4 transmittance spectrum of the Sn-Ti-O thin film on the MgAl<sub>2</sub>O<sub>4</sub> substrate.

## Chapter 4

### Analysis on native point defects in $\text{SnNb}_2\text{O}_6$

#### 1. Introduction

Oxides including Sn(II) ions are expected to have unique electronic structures associated with the presence of Sn-5s electrons[1-3]. Tin monoxide (SnO), the prototypical Sn(II) oxide, is known to exhibit *p*-type conductivity[1,4] due to a shallow valence band maximum (VBM) constructed from hybridization of O-2*p* and Sn-5*sp* which encourages a hole doping. Similar electronic structures are predicted for complex oxides with Sn(II), *e.g.*,  $\text{SnWO}_4$ ,  $\text{SnNb}_2\text{O}_6$ ,  $\text{Sn}_2\text{Ta}_2\text{O}_7$ , by first-principles calculations[2,3,5]. However, reports on their electrical properties are limited to those on  $\text{SnWO}_4$  of *n*-type[6,7].

In my pervious study, the epitaxial thin films of Sn-*M*-O (*M*=Nb, Ta) pyrochlore and  $\text{SnNb}_2\text{O}_6$  did not exhibit electrical conductivity even if dopants were added to them (Chapter 3). Particularly for  $\text{SnNb}_2\text{O}_6$ , its relatively large band dispersion at VBM states was predicted from the first-principles calculation, which indicates a high hole mobility (Chapter 2). Meanwhile, the analysis of X-ray photoelectron spectroscopy (XPS) showed its Fermi level located around the center of the band gap. This indicates the low carrier density of the  $\text{SnNb}_2\text{O}_6$  thin film. I speculated that the low carrier density of  $\text{SnNb}_2\text{O}_6$  had a root in the carrier compensation caused by the defect formation.

In semiconductors, native point defects can act as a source or a compensation of carriers. For SnO, it has been suggested that the acceptor-like Sn vacancy is a source

of its relatively high hole density without doping. In addition, there is a theoretical analysis on defect formation in an Sn(II) complex oxide; that on  $\text{K}_2\text{Sn}_2\text{O}_3$  reported by G. Hautier *et al.*[5]. They reported that K vacancy acts as a shallow acceptor with small formation energy. Moreover, the formation energy of O vacancy which can compensate holes is relatively high at oxidizing condition (shown in Fig. 1). This indicates intrinsic *p*-type conductivity of  $\text{K}_2\text{Sn}_2\text{O}_3$  as well as SnO, though it is not confirmed experimentally maybe because it is immediately hydrolyzed in air. Meanwhile, it is unclear whether such a defect formation trend is common for Sn(II) oxides or not, since it has never been investigated for other Sn(II) compounds including  $\text{SnNb}_2\text{O}_6$ .

In this study, the formation energies of point defects and their local structures in  $\text{SnNb}_2\text{O}_6$  are investigated using first-principles calculations in order to explain its deep Fermi level and to examine the possibility of carrier doping on it.

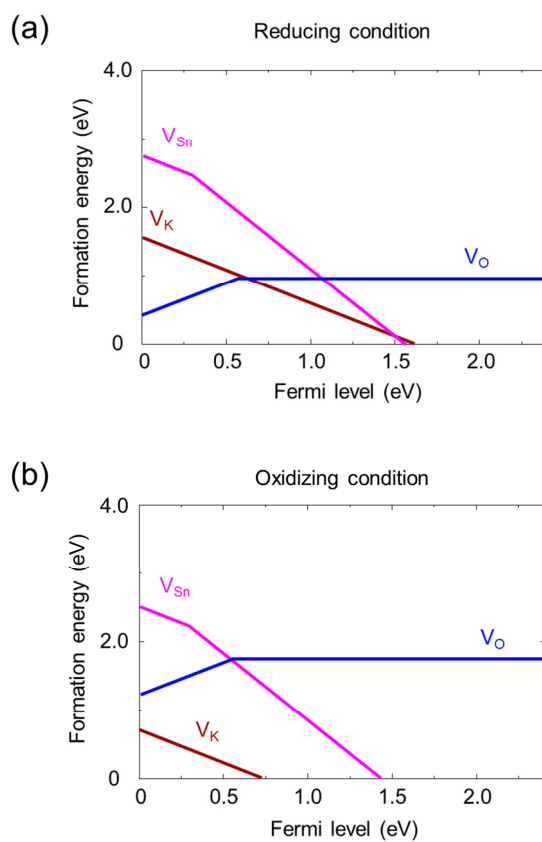


Figure 1 Calculated defect formation energies of vacancies in  $K_2Sn_2O_3$  Reported by G. Hautier *et al.*[5]. The formation energies of Sn-site vacancy ( $V_{Sn}$ ), K-site vacancy ( $V_K$ ), and O-site vacancy ( $V_O$ ) are presented under (a) reducing condition and (b) oxidizing condition.

## 2. Computational procedure

The first-principles calculations were performed by the projector augmented-wave (PAW) method[8] as implemented in the VASP code[9,10]. PAW data sets with radial cutoffs of 1.6, 1.5, and 0.8 Å were used for Sn, Nb, and O. Their valence electrons were treated as following; Sn  $5s, 5p$ ; Nb  $3p, 4d$ , O  $2s, 2p$ . The HSE06 hybrid functional[11] was used for the exchange correlation functional. The lattice constants and internal atomic positions of a primitive cell were fully relaxed within its symmetry in advance (Table 1). Then, a 72 atoms supercell was constructed by expanding the primitive cell of  $\text{SnNb}_2\text{O}_6$  as shown in Fig 2. The internal atomic positions of the defect supercells which contain a defect were relaxed with the lattice parameters fixed.  $\Gamma$ -centered  $2 \times 2 \times 2$  k-point sampling was employed for the supercell calculations.

The formation energy of each defect is calculated as[12]

$$E^f(D^q) = E(D^q) - E(\text{perfect}) - \sum_i n_i \mu_i + q(\varepsilon_{\text{VBM}} + \Delta\varepsilon_f), \quad (1)$$

where  $E(D^q)$  is the total energy of the supercell with a defect  $D$  in charge state of  $q$ .  $E(\text{perfect})$  is the total energy of the supercell of the perfect crystal.  $n_i$  is the number of  $i$  atoms removed ( $n_i < 0$ ) or added ( $n_i > 0$ ) and  $\mu_i$  is the chemical potential of it. The chemical potential can change in the range where the target compound is stable.  $\varepsilon_{\text{VBM}}$  is the energy level of the VBM.  $\varepsilon_{\text{VBM}} + \Delta\varepsilon_f$  is the Fermi level and  $\Delta\varepsilon_f$  is considered as a variable which changes from zero to the band gap value.

The defect concentrations were calculated using the defect formation energies as

$$C(D^q) = N[D] \exp\left(-\frac{E_f[D^q]}{k_B T}\right), \quad (2)$$

where  $N[D]$  is the number of the site for a defect  $D$ ,  $k_B$  is the Boltzmann' constant, and  $T$  is absolute temperature. The electron concentration in the conduction band and

the hole concentration in the valence band are obtained from the Fermi-Dirac distribution as following, respectively.

$$n = \int_{\varepsilon_{CBM}}^{\infty} D(\varepsilon) \frac{1}{e^{(\varepsilon - \varepsilon_f)/k_B T} + 1} d\varepsilon, \quad (3)$$

$$p = \int_{-\infty}^{\varepsilon_{VBM}} D(\varepsilon) \frac{1}{e^{(\varepsilon_f - \varepsilon)/k_B T} + 1} d\varepsilon, \quad (4)$$

where  $D(\varepsilon)$  is the density of states for bulk and  $\varepsilon_{CBM}$  is the energy level of the conduction band minimum (CBM). The concentrations of defects and carriers are under the condition of the charge neutrality described as

$$p - n + \sum qC[D^q] = 0. \quad (5)$$

Solving this equation self-consistently, the concentrations and the Fermi level are determined.

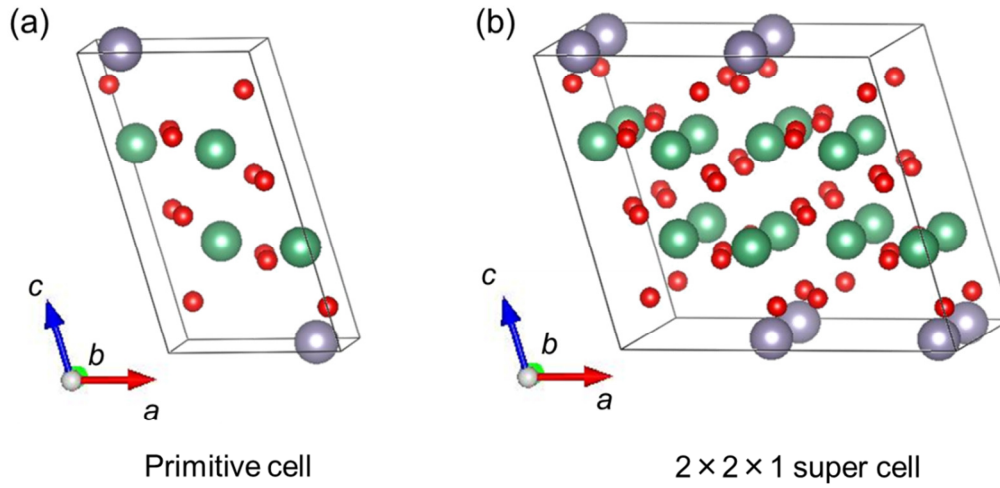


Figure 2 Unit cell of  $\text{SnNb}_2\text{O}_6$  for defect calculations. (a) Primitive cell for optimization of the lattice constants. (b) Supercell constructed by  $2 \times 2 \times 1$  of primitive cell for the defect calculations.

Table 1 Optimized lattice constants using primitive cell of Fig. 2 (a).

	$a$ (Å)	$b$ (Å)	$c$ (Å)	$\alpha$	$\beta$	$\gamma$
Optimized with HSE06	17.21	4.911	5.627	90.00	91.84	90.00
Exp	17.11	4.922	5.594	90.00	90.81	90.00

### 3. Results and discussion

The range of chemical potential where  $\text{SnNb}_2\text{O}_6$  is stable is obtained in consideration of equilibrium conditions with the competing phases, *i. e.*,  $\text{SnO}$ ,  $\text{SnO}_2$ ,  $\text{Sn}$ ,  $\text{Nb}_2\text{O}_5$ ,  $\text{Nb}$ , and  $\text{O}_2$ . The total energies of them were calculated with the HSE06 functional. The obtained phase diagram of the Sn-Nb-O ternary system is presented in Fig. 3. The stable region of  $\text{SnNb}_2\text{O}_6$  is represented in red color. The possible ranges of chemical potentials are listed in table 2. The variable range of chemical potential for each element is limited within 0.1 eV. This corresponds to that a little freedom is permitted for controlling the defect concentration by varying the synthesis conditions at least under thermal equilibrium. For the calculation of formation energies shown later, the chemical potentials were used as the values at the center of the stable region of  $\text{SnNb}_2\text{O}_6$ .

Here, I treat the fundamental native defects, vacancies at Sn, Nb, and O sites ( $V_{\text{Sn}}$ ,  $V_{\text{Nb}}$ , and  $V_{\text{O}}$ ) and cation anti-sites of Sn at Nb sites ( $\text{Sn}_{\text{Nb}}$ ) and Nb at Sn sites ( $\text{Nb}_{\text{Sn}}$ ). For  $V_{\text{O}}$ , the three different Wyckoff positions of oxygen were separately calculated;  $V_{\text{O}1}$ ,  $V_{\text{O}2}$ , and  $V_{\text{O}3}$ . The considered charge states are as follow; -2 to 0 for  $V_{\text{Sn}}$ , -5 to 0 for  $V_{\text{Nb}}$ , 0 to +2 for  $V_{\text{O}}$ , -3 to 0 for  $\text{Sn}_{\text{Nb}}$ , and 0 to +3 for  $\text{Nb}_{\text{Sn}}$ .

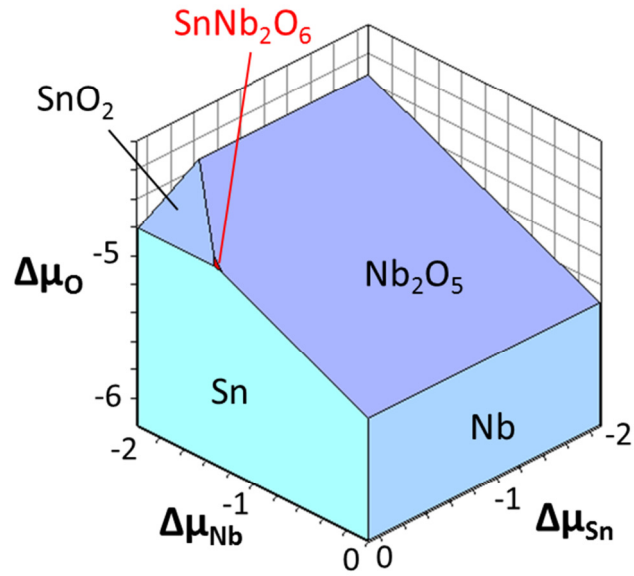


Figure 3 Sn-Nb-O ternary Phase diagram. The region where  $\text{SnNb}_2\text{O}_6$  is stable is filled with red color.

Table 2 Possible range of chemical potentials for Sn, Nb, and O in  $\text{SnNb}_2\text{O}_6$ .

	Small	Large
$\mu_{\text{Sn}}$	-4.57 eV	-4.52 eV
$\mu_{\text{Nb}}$	-14.4 eV	-14.3 eV
$\mu_{\text{O}}$	-9.64 eV	-9.59 eV

In Fig. 4-6, the calculated defect formation energies are plotted versus Fermi level. The energy origin for the Fermi level is set at the VBM and the maximum value of it is 2.41 eV which corresponds to the CBM. Figure 7 and 8 shows the local structures around the each defect with the representative charge state. Among the three kinds of  $V_O$ ,  $V_{O2}$  shows the lowest formation energy for any Fermi energy through the band gap. The O2-site is coordinated by two cations in contrast to the others coordinated by three as shown in Fig. 7(a-c). The relatively lower formation energy of  $V_{O2}$  may be attributed to the less covalent bonding between O and coordinated cations.  $V_O$  exhibits negative formation energy with the Fermi level from VBM to almost the center of the band gap, which insists that  $V_O$  acts as the pinning of Fermi level: the pinning level is at about 1.0 eV above the VBM. On the other hand,  $V_{Sn}$  and  $V_{Nb}$  are found to act as shallow and deep acceptor, respectively. Their formation energies also exhibit negative values for particular range within the band gap. For  $V_{Sn}$ , the sign is inverted at about 1.8 eV. The local structures around the vacancies are not significantly distorted after the geometrical optimization while the coordinating oxygen ions slightly moved outward.

For the anti-site cation of  $Sn_{Nb}$ , charged state of -1 is stable in wide range. It corresponds to Sn(IV) at Nb sites. In  $SnO_2$ , prototypical Sn(IV) oxide, Sn ions are located at the center of oxygen octahedrons and such coordination environment is common for Nb sites in  $SnNb_2O_6$ . The bond lengths of Nb-O of perfect structure are scattered from 1.84 to 2.21 Å. Contrarily,  $Sn_{Nb}^+$ -O bond lengths exhibit similar values.

$Nb_{Sn}$  exhibits three types of stable charge states, +1, +2, and +3, for certain range within the band gap. Both of the transition levels of +2/+1 and +3/+2 are deep from the CBM. The formation energy shows relatively low and negative value below

0.7 eV. It is found that the local structures around  $\text{Nb}_{\text{Sn}}$  are significantly distorted from the perfect structure for all of the considered charge states. The Nb ion moves toward the near oxygen ions, the upper side of Fig. 8 (d). The angle between the longer Nb-O bonds of 172 degrees is much larger than that of the O-Sn-O angle of the perfect structure, 145 degrees. The characteristic local structure around Sn(II) in  $\text{SnNb}_2\text{O}_6$ , Sn(II) at a pyramidal top, is attributed to the presence of lone-pair electrons of Sn-5s. Such a structure is considered to be not suitable for an Nb ion.

The defect formation energies with most stable charge states are summarized in Fig. 9. Considering the charge neutrality represented as formula (5), the equilibrium Fermi level and concentrations of defects and carriers were determined. The Fermi level at 773 K is 1.40 eV above the VBM, which is shown as a broken line in the Fig. 9. The temperature dependence of the Fermi level is small: almost the same value through 300 K to 1000 K. The Fermi level is close to the value obtained from the XPS experiment on the  $\text{SnNb}_2\text{O}_6$  epitaxial thin film, 1.3 eV as shown in chapter 3.

The temperature dependence of the equilibrium defect concentrations at Fermi level are shown in Fig. 10 and Table 3. The dominant defects are found to be  $\text{V}_{\text{O}_2}^{2+}$ ,  $\text{Sn}_{\text{Nb}}^-$ , and  $\text{V}_{\text{Sn}}^{2-}$ . Although there have been no experimental investigation on defects of  $\text{SnNb}_2\text{O}_6$ , this result is qualitatively similar to the non-stoichiometry of Sn-Nb-O pyrochlore. Sn-Nb-O pyrochlore which is described as  $\text{Sn}_2\text{Nb}_2\text{O}_7$  for the stoichiometric composition is known to show non-stoichiometry including a large amount of defects[13,14]. L. Cruz *et al.* reported that the sample of  $\text{Sn}_{1+x}\text{Nb}_2\text{O}_{6+x}$  with pyrochlore structure included Sn(IV) at Nb site and Sn site vacancy from the XRD and Mössbauer analyses[14]. The surplus charge was suggested to be compensated by oxygen vacancies, which is not evidenced in the experiments.

The formation of  $V_O^{2+}$  and  $V_{Sn}^{-2}$  limits the Fermi level, which prevent increase of the carrier concentration even if dopants are added. The lower limit of Fermi level is 1.0 eV above the VBM and the higher is 0.6 eV below the CBM. It shows the difficulty in obtaining conductivity, especially for *p*-type. The experimentally observed deep Fermi level of  $SnNb_2O_6$  is considered to have a root in the formation of kinds of point defects.

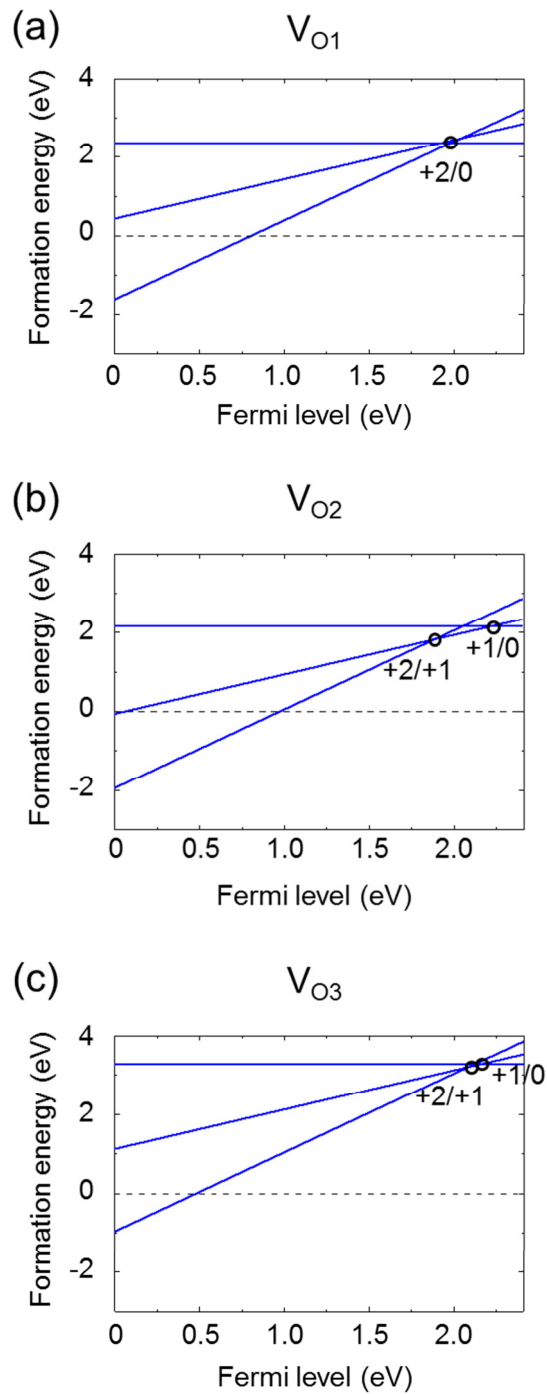


Figure 4 Formation energies of O vacancies in  $\text{SnNb}_2\text{O}_6$ , (a)  $V_{O1}$ , (b)  $V_{O2}$ , and (c)  $V_{O3}$ , as a function of Fermi energy relative to the VBM. The thermodynamical transition levels are denoted by open circles.

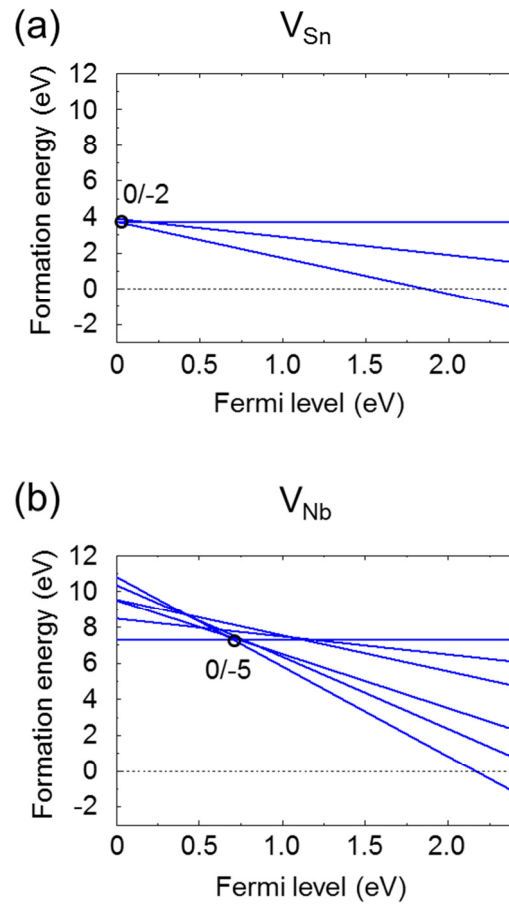


Figure 5 Formation energies of cation vacancies in  $\text{SnNb}_2\text{O}_6$ , (a)  $V_{\text{Sn}}$ , and (b)  $V_{\text{Nb}}$ , as a function of Fermi energy relative to the VBM. The thermodynamical transition levels are denoted by open circles.

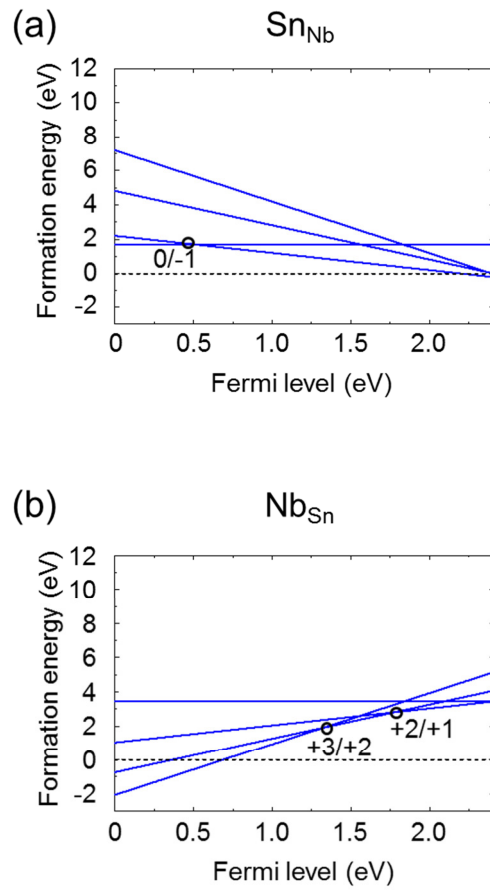


Figure 6 Formation energies of anti-site of cations in  $\text{SnNb}_2\text{O}_6$ , (a)  $\text{Sn}_{\text{Nb}}$ , and (b)  $\text{Nb}_{\text{Sn}}$ , as a function of Fermi energy relative to the VBM. The thermodynamical transition levels are denoted by open circles.

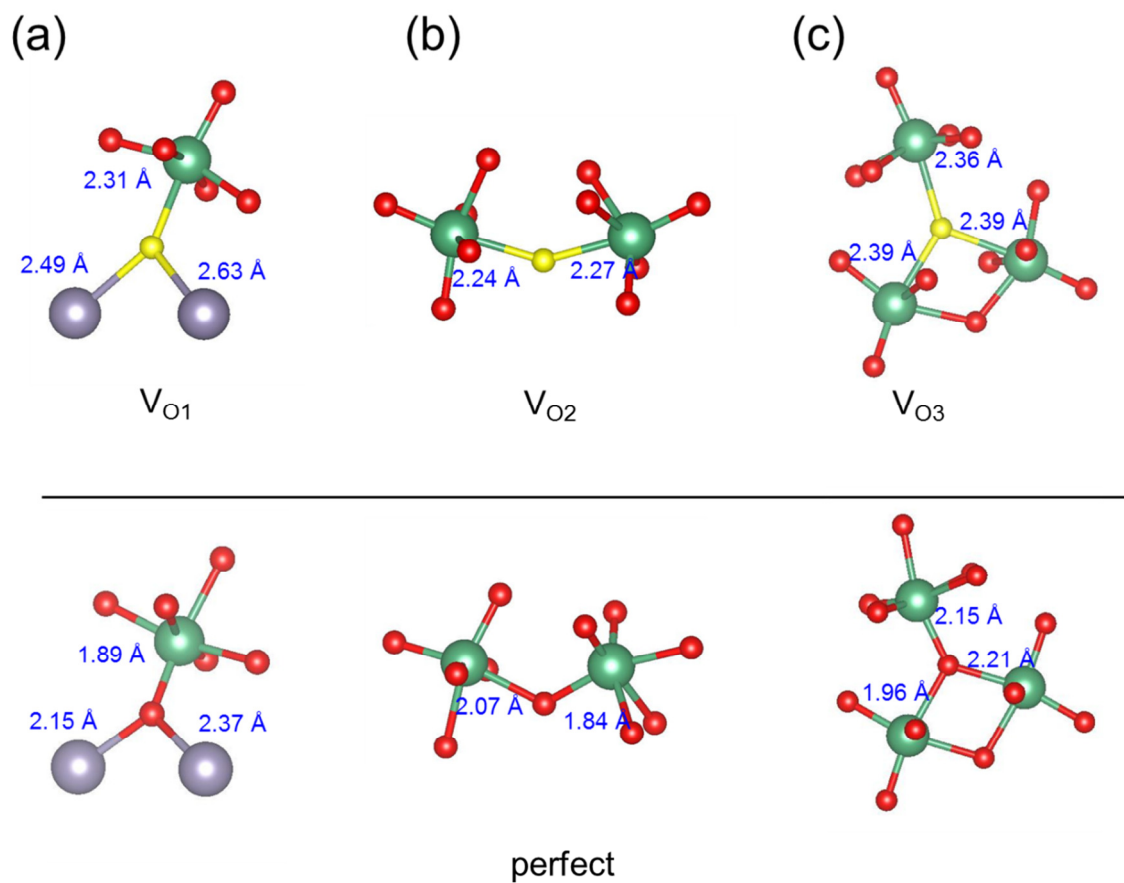


Figure 7 Comparison between local structures of O vacancies (upper) and those of the perfect structure (lower). (a)  $V_{O1}$ , (b)  $V_{O2}$ , and (c)  $V_{O3}$ . Yellow circles denote the vacancy sites before geometrical optimization.

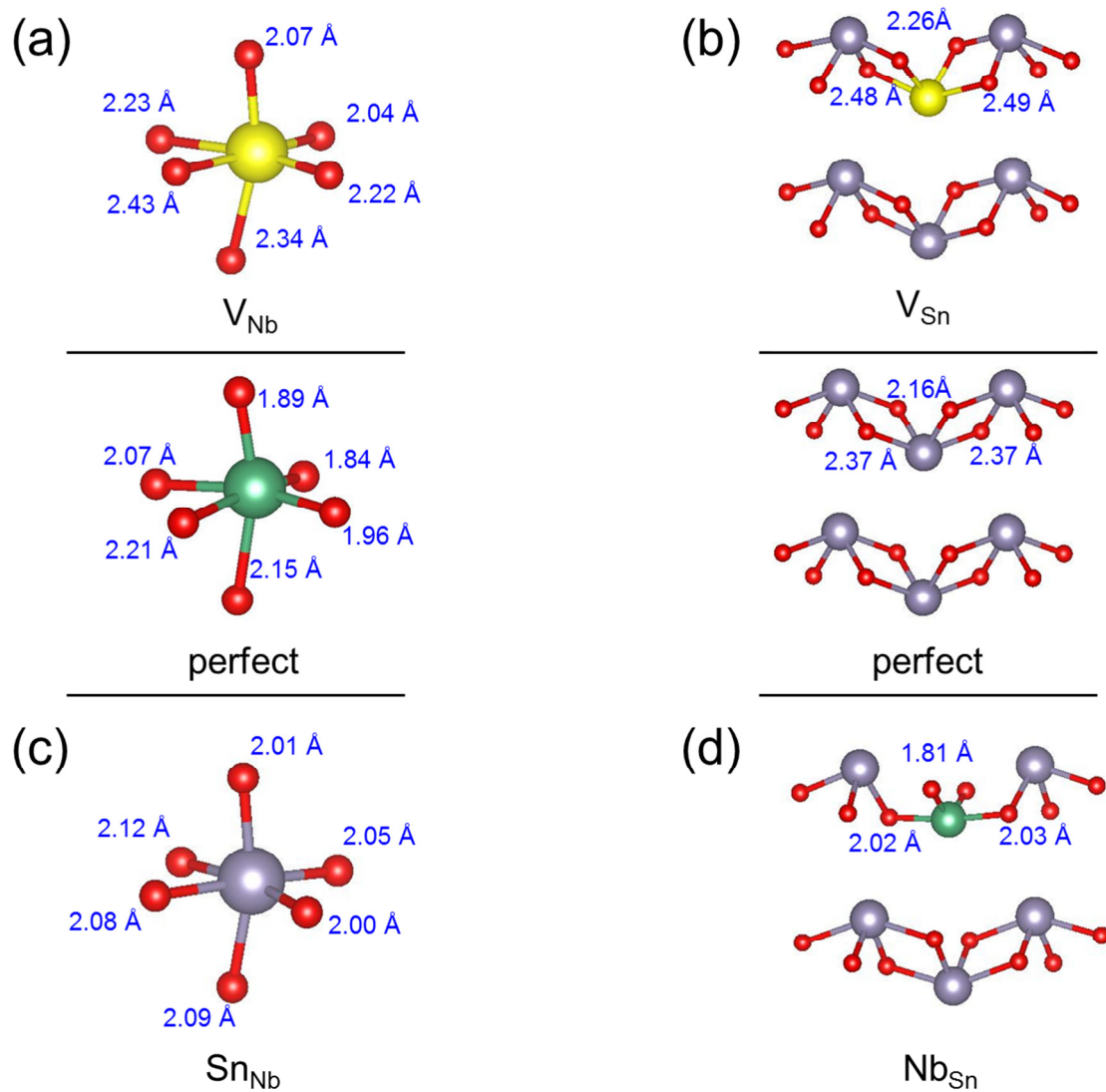


Figure 8 Comparison between local structures of cation vacancies (upper), those of the perfect structure (middle), and those of anti-site of cations (lower). (a)  $V_{Nb}$ , (b)  $V_{Sn}$ , (c)  $Sn_{Nb}$ , and (d)  $Nb_{Sn}$ . Yellow circles denote the vacancy sites before geometrical optimization.

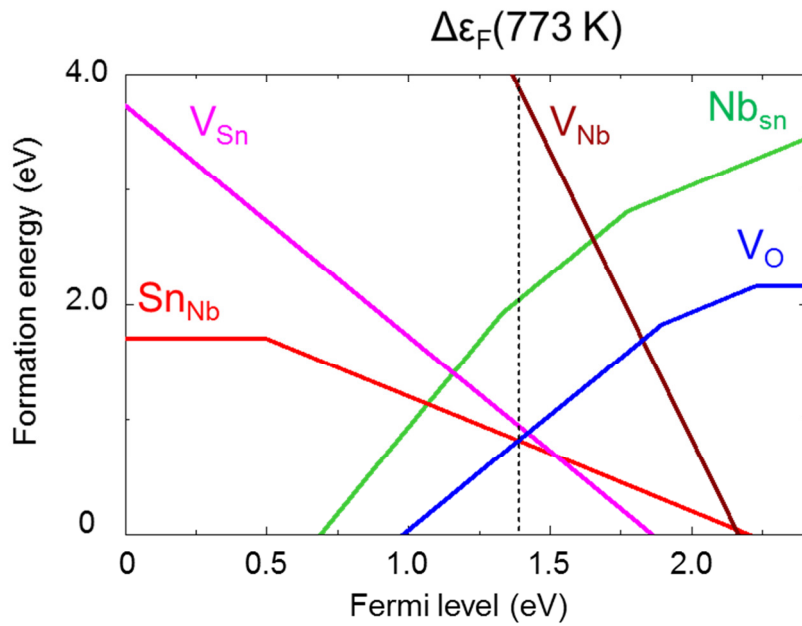


Figure 9 Summary of the formation energies for the considered defects. For each defect, only the charge state of the most stable is drawn. For O vacancy, only  $V_{\text{O}2}$  is described as the representative.

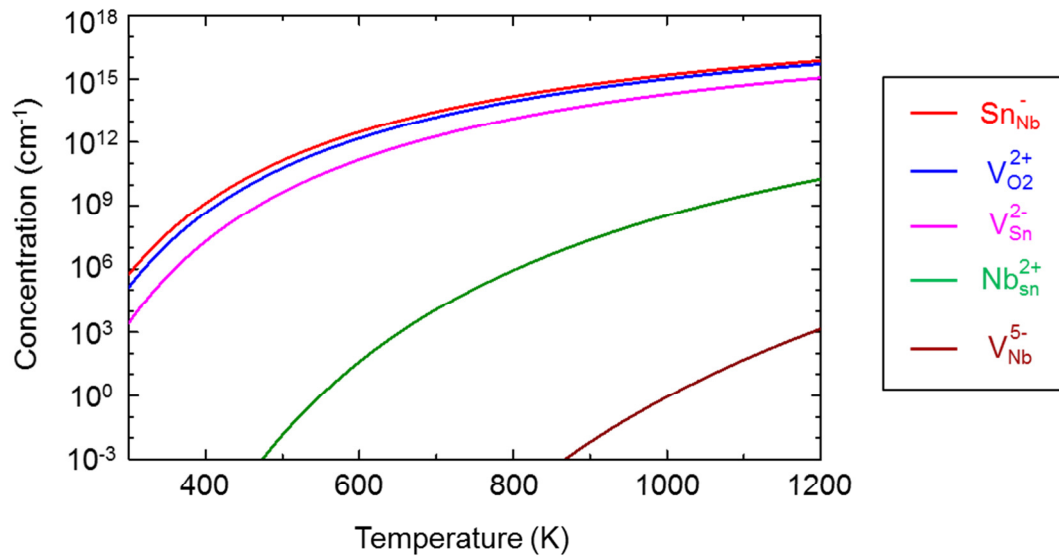


Figure 10 Temperature dependence of the defect concentration. For each defect, most stable charge state at the equilibrium Fermi level is described.

Table 3 Concentrations of dominant defects at room temperature (300 K), temperature for thin film growth (773 K), and for solid state reaction (1073 K).

	defect concentration		
	300 K	773 K	1073 K
$V_O^{2+}$	$1.4 \times 10^5 \text{ cm}^{-1}$	$5.8 \times 10^{13} \text{ cm}^{-1}$	$2.0 \times 10^{15} \text{ cm}^{-1}$
$Sn_{Nb}^-$	$5.6 \times 10^5 \text{ cm}^{-1}$	$9.9 \times 10^{13} \text{ cm}^{-1}$	$2.9 \times 10^{15} \text{ cm}^{-1}$
$V_{Sn}^{2-}$	$2.8 \times 10^3 \text{ cm}^{-1}$	$8.2 \times 10^{12} \text{ cm}^{-1}$	$3.9 \times 10^{14} \text{ cm}^{-1}$

#### 4. Conclusion

The formation energies and local structures of the native point defects in  $\text{SnNb}_2\text{O}_6$  are investigated by first-principles calculations. Some defects show negative formation energies in certain ranges of Fermi level within the band gap. The Fermi level at room temperature and synthesis temperature is located at deep position from both of the VBM and CBM. The dominant defects are  $V_{\text{O}}^{2+}$ ,  $\text{Sn}_{\text{Nb}}^-$ , and  $V_{\text{Sn}}^{2-}$ , which is consistent with the analogy of the non-stoichiometry of  $\text{Sn}_2\text{Nb}_2\text{O}_7$ . The Fermi level pinning caused by  $V_{\text{Sn}}^{2-}$  and  $V_{\text{O}}^{2+}$  is predicted to prevent carrier doping. This is different tendency from  $\text{SnO}$  and  $\text{K}_2\text{Sn}_2\text{O}_3$  which represent high formation energies of  $V_{\text{O}}$ .  $\text{Sn(II)}$  ternary oxides do not necessarily show the  $\text{SnO}$ -like  $p$ -type conductivity despite their VBM character similar to that of  $\text{SnO}$ , because of the different tendency in defect formation.

## References

- [1] Y. Ogo, H. Hiramatsu, K. Nomura, H. Yanagi, T. Kamiya, M. Kimura, M. Hirano and H. Hosono, *Phys. Status Solidi A* 206 (2009) 2187.
- [2] Y. Hosogi, Y. Shimodaira, H. Kato, H. Kobayashi and A. Kudo, *Chem. Mater.* 20 (2008) 1299.
- [3] M.W. Stoltzfus, P.M. Woodward, R. Seshadri, J.H. Klepeis and B. Bursten, *Inorg. Chem.* 46 (2007) 3839.
- [4] A. Togo, F. Oba, I. Tanaka and K. Tatsumi, *Phys. Rev. B* 74 (2006).
- [5] G. Hautier, A. Miglio, G. Ceder, G.M. Rignanese and X. Gonze, *Nat Commun* 4 (2013) 2292.
- [6] J.L. Solis and V. Lantto, *Phys. Scripta* T69 (1997) 281.
- [7] J.L. Solis, J. Frantti, V. Lantto, L. Haggstrom and M. Wikner, *Phys. Scripta* T79 (1999) 216.
- [8] P.E. Blochl, *Phys. Rev. B* 50 (1994) 17953.
- [9] G. Kresse and J. Furthmuller, *Phys. Rev. B* 54 (1996) 11169.
- [10] G. Kresse and D. Joubert, *Phys. Rev. B* 59 (1999) 1758.
- [11] J. Heyd, G.E. Scuseria and M. Ernzerhof, *J. Chem. Phys.* 118 (2003) 8207.
- [12] S.B. Zhang and J.E. Northrup, *Physical Review Letters* 67 (1991) 2339.
- [13] T. Birchall and A.W. Sleight, *J. Solid State Chem.* 13 (1975) 118.
- [14] L.P. Cruz, J.M. Savariault, J. Rocha, J.C. Jumas and J.D.P. de Jesus, *J. Solid State Chem.* 156 (2001) 349.

## Chapter 5

### Summary and Conclusion

In this thesis, electronic structures, optical properties, and electrical properties of Sn(II) ternary oxides were investigated by first-principles calculations and characterization using epitaxial thin films. In addition, calculations on the defect formation were performed. The main points of the results are summarized below.

In Chapter 2, the electronic structures of Sn(II) complex oxides with *d0* transition metals have been investigated by first-principles calculations based on the density functional theory with the HSE06 hybrid functional. The calculations confirm the common character of electronic structures for the Sn(II) complex oxides that their valence bands are dominantly composed of the hybridized states of O-2*p* and Sn-5*sp*. Relatively large band dispersion at the valence band maximum (VBM) is observed for the compounds which are considered to exhibit the correlation between Sn lone-pairs. They are assumed to show high hole mobilities if holes could be injected in the valence bands. In addition, most of them have the band gaps corresponding to the visible light region. Although they exhibit the indirect-type band structures, the difference between direct- and indirect-gap is 0.2 eV for the maximum, which indicates the possibility of good photo-absorption properties of them.

In Chapter 3, the optical and electrical properties of Sn(II) ternary oxides, Sn-*M*-O (*M*=Nb, Ta) pyrochlore, SnNb<sub>2</sub>O<sub>6</sub>, and  $\alpha$ -SnWO<sub>4</sub>, have been investigated using the thin films fabricated by the pulsed laser deposition method. The thin films are found to be epitaxially grown on single crystal substrates from the XRD analyses. Their

absorption coefficients were obtained by the spectroscopy. The absorption thresholds are consistent with the reported bulk values for all of them. Electrical conductivity is observed for only the  $\alpha$ -SnWO<sub>4</sub> film whose resistivity is  $9.2 \times 10^4 \Omega\text{cm}$ . The other films are insulator even if dopants are added to them. The XPS analyses showed that the Fermi levels of the Sn(II) ternary oxides are located at deep positions from both of the band edges in contrast to that of the *p*-type SnO film coincident with the VBM. This is in line with the high resistivity of the complex oxide films and indicates the Fermi level pinning caused by defects in the crystals.

In Chapter 4, the formation energies and local structures of the native point defects in SnNb<sub>2</sub>O<sub>6</sub> are investigated by first-principles calculations in order to explain its deep Fermi level and to examine the possibility of carrier doping on it. The calculations were performed with the HSE06 hybrid functional. Some of the defects show negative formation energies in certain ranges of Fermi level within the band gap. The equilibrium Fermi level is located at a deep position from both of the VBM and CBM regardless temperature. This is consistent the result of the XPS measurement on the SnNb<sub>2</sub>O<sub>6</sub> epitaxial thin film. The dominant defects at Fermi level are  $V_{\text{O}}^{2+}$ ,  $\text{Sn}_{\text{Nb}}^-$ , and  $V_{\text{Sn}}^{2-}$ , which is in line with the analogy of the non-stoichiometry of Sn<sub>2</sub>Nb<sub>2</sub>O<sub>7</sub>. The Fermi level pinning caused by  $V_{\text{Sn}}^{2-}$  and  $V_{\text{O}}^{2+}$  is predicted to prevent a carrier doping. This is different tendency from SnO and K<sub>2</sub>Sn<sub>2</sub>O<sub>3</sub> which represent relatively high formation energy of  $V_{\text{O}}$ .

In conclusion, the Sn(II) ternary oxides have the unique band structures associated with Sn-5s electrons. Meanwhile, it is found that they do not necessarily show *p*-type conductivity despite its similar character of the VBM to that of SnO. One of the reasons of this is found to be the different tendency in defect formation.

## Acknowledgements

The author would like to express the deepest gratitude to Professor Isao Tanaka at Kyoto University for continuous support and constant encouragement throughout this work. The author wishes to express his gratitude to Associate Professor Fumiyasu Oba for his continuous helpful discussions and advice. The author would also like to express his gratitude to Associate Professor Atsushi Togo and Assistant Professor Atsuto Seko for their productive advices. He would like to express his deepest appreciation to Professor Akira Sakai and Kuniaki Murase for their critical reading of this thesis.

The author sincerely thanks Assistant Professor Yu Kumagai at Tokyo Institute of Technology for generous discussions and advice on the first-principles calculations. The author acknowledges Dr. Yutaka Sonobayashi at Kyoto University for advices and managements on operating XPS. The author is deeply grateful to Dr. Kenji Kazumi and Dr. Nobuharu Sasaki for helpful managements on measurement of SEM-WDS and TEM observation.

The author would like to show his great appreciation to Dr. Hiroyuki Hayashi at Kyoto University for his helpful discussion and lecture on the experiment including PLD, XRD, and spectroscopy. The author has also greatly benefited from Mr. Yusuke Ogawa for supports on the experiments of the thin film growth.

The author would like to thank to Dr. Hidenobu Murata, Dr. Masahiro Mori, and Mr. Kazuki Shitara for giving continuous encouragement. The author wishes to make grateful acknowledgement to the members of Professor Tanaka's group for helpful discussions throughout this work.

Finally, the author would like to sincerely thank his family for their enduring support and encouragement.